

A CYLINDRICAL DIELECTRIC WHISPERING-
GALLERY MODE TERAHERTZ CAVITY
COUPLED WITH A DIELECTRIC
SLAB WAVEGUIDE

By

JIANGQUAN ZHANG

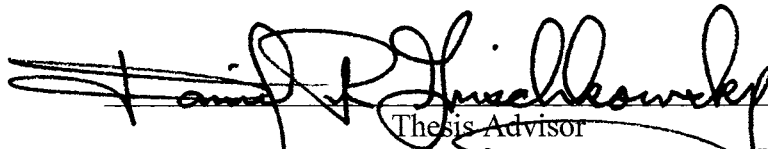
Bachelor of Science
University of Science and Technology of China
Hefei, Anhui, China
1992


Master of Science
Chinese Academy of Sciences
Beijing, China
1995


Submitted to the Faculty of the
Graduate College of the
Oklahoma State University
in partial fulfillment of
the requirements for
the Degree of
DOCTOR OF PHILOSOPHY
August, 2002

A CYLINDRICAL DIELECTRIC WHISPERING-
GALLERY MODE TERAHERTZ CAVITY
COUPLED WITH A DIELECTRIC
SLAB WAVEGUIDE

Thesis Approved:


Thesis Advisor




Albert T. Roeder


Dean of the Graduate College

Acknowledgments

I would like to express my sincere gratitude and deep appreciation to Dr. Daniel R. Grischkowsky, the principle advisor of my academic study and doctoral research, for his exceptional guidance and financial support throughout this study. I am especially grateful for his encouragement during the hard times of this study, which made possible the completion of this thesis.

Appreciation is also extended to other members of my advisory committee, Dr. R. Alan Cheville, Dr. James C. West, and Dr. Albert T. Rosenberger, for their time, valuable suggestions and advice. Dr. Rosenberger was especially helpful in the discussions of the coupling and in getting the literature on whispering-gallery mode. Thanks are also due to all the members of the Terahertz group, for their help and valuable discussions over the years.

This thesis is dedicated to my family in China – my parents, brothers, and sisters – for their never-ending love, encouragement and support throughout my entire life. Of course, my loving wife, Li, deserves to share all my achievements for her love and support ever since we met.

TABLE OF CONTENTS

Chapter	Page
I. INTRODUCTION	1
1.1 Whispering-Gallery Mode Resonators	1
1.2 Terahertz Time Domain Spectroscopy System	3
1.3 Terahertz Waveguides	5
1.4 Purpose of This Study	6
II. EXPERIMENTAL SETUP AND COUPLING STRUCTURES	8
III. EXPERIMENTAL RESULTS	18
3.1 The Input Pulse	18
3.2 Results from Structure A	20
3.3 Results from Structure B	27
IV. MODAL ANALYSIS	35
4.1 Mode Solutions for the Metal Plate Waveguide	35
4.2 Mode Solutions of TM Modes for Dielectric Slab Waveguide	39
4.3 Mode Solutions of Cylindrical WG Modes	44
V. COUPLED MODE THEORY	51

5.1	Reciprocity Relation in Cylindrical Coordinates	52
5.2	Coupled Mode Equations in Cylindrical Coordinates.....	54
5.3	Coupled Mode Equations for Slab and Cylinder System.....	59
VI. NUMERICAL RESULTS		64
6.1	Quasioptic Coupling.....	64
6.2	Dispersion and Phase Match	68
6.3	Coupling Coefficients	70
6.4	Coupling from Slab to Cylinder: Single Mode Coupling	73
6.5	Coupling from Cylinder to Slab and the Effect of TM_1 Mode	80
6.6	Transfer Functions for Cavity Pulses.....	87
6.7	Multimode Coupling from Slab to Cylinder	90
6.8	Comparison between Experiment and Theory.....	95
VII. CONCLUSIONS AND PERSPECTIVES		106
BIBLIOGRAPHY.....		111
APPENDIXES		118
Appendix A. Impedance, Orthogonality and Normalization of Guided Modes		118
Appendix B. Derivation of Reciprocity Relation (5-4)		123
Appendix C. Derivation of Longitudinal Components (5-9a) and (5-9b).....		125
Appendix D. Physical Explanation of Coupled Mode Equations		127
Appendix E. Quasioptic Coupling.....		131
Appendix F. Fourth-Order Runge-Kutta Method		134

LIST OF FIGURES

Figure	Page
2-1	Experimental setup 9
2-2	The output scan and the spectrum profile of the THz setup 11
2-3	Cross-sections of the coupling structures 12
2-4	Illustration of the coupling between the slab and the cylinder 15
2-5	Cylinder holders 17
3-1	Measured input pulse and its spectrum 19
3-2	Measured time domain pulses for structure A 21
3-3	Main transmitted pulses and spectra for structure A 23
3-4	The first and the second cavity pulses for structure A 25
3-5	The spectra of the first and the second cavity pulses for structure A 26
3-6	Measured time domain pulses for structure B 29
3-7	Main transmitted pulses and spectra for structure B 30
3-8	The first and the second cavity pulses for structure B 32
3-9	The spectra of the first and the second cavity pulses for structure B 33
4-1	Cross section and coordinate system of the metal plate waveguide 36
4-2	Mode profiles of the first three TM modes for the metal waveguide 38

4-3	Silicon slab waveguide	39
4-4	Normalized field patterns for slab waveguide	42,43
4-5	Dielectric cylinder and cylindrical coordinate system	44
4-6	E^r field profiles for WG modes for $l = 200$	47
4-7	Normalized field patterns for cylindrical WG modes	49,50
5-1	Concentric rings coupling configuration	55
5-2	Relative permittivities for the concentric rings	55
5-3	Cross section and coordinate system of the slab-cylinder coupling structure	60
6-1	Amplitude coupling coefficients for Gaussian and metal plate waveguide	65
6-2	Amplitude coupling coefficients for metal TEM and slab TM modes	67
6-3	Effective refractive indexes of TM and WG modes	69
6-4	Coupling coefficients C_{sc} and M_{sc} for TM_0 mode and WG modes	71
6-5	Coupling coefficients C_{sc} and M_{sc} for TM_1 mode and WG modes	72
6-6	Excitation and coupling diagram for slab-cylinder	75
6-7	Amplitude evolution for single mode coupling from TM_0 to WG modes	76
6-8	Single-mode coupling results for coupling from TM_0 to WG modes	78
6-9	Total power for single mode coupling from TM_0 to WG modes	79
6-10	Single-mode coupling results for coupling form WG to TM_0 mode	81
6-11	Total power for single mode coupling from WG to TM_0 mode	82
6-12	Amplitude and phase change for coupling from WG modes to TM_0 mode at 1.0 THz	83
6-13	Amplitude and phase change for coupling from WG modes to TM_0 mode at 1.5 THz	84
6-14	Amplitude and phase change for coupling from WG modes	

	to TM_0 and TM_1 modes at 1.0 THz	85
6-15	Amplitude and phase change for coupling from WG modes to TM_0 and TM_1 modes at 1.5 THz	86
6-16	Frequency transfer functions for cavity pulses from single mode coupling	89
6-17	Amplitude evolution for coupling from TM_0 mode to WG modes for the case of multimode coupling	91
6-18	Frequency transfer functions for cavity pulses from multimode coupling	93
6-19	Frequency transfer function for the main transmitted pulse	94
6-20	Spectrum comparison for cavity pulses of structure A	96
6-21	Time domain pulse comparison for cavity pulses of structure A	97
6-22	Comparison for main transmitted pulse for structure A	98
6-23	Spectrum comparison for cavity pulses of structure B	100
6-24	Time domain pulse comparison for cavity pulses of structure B	101
6-25	Comparison for main transmitted pulse for structure B	102
6-26	Comparison of the transfer functions for the main transmitted pulses	104
D-1	A prescribed distribution of currents in cylindrical coordinates	127
D-2	Induced current representation of perturbations	129
E-1	Quasioptic coupling configuration	131

NOMENCLATURE

a	Radius of cylinder, m
$a(\theta)$	θ -dependent modal amplitude of ring a
a_m	Modal amplitude of WG_m mode
a_s	Modal amplitude of slab TM_0 mode
a_{cm}^c	Final coupled modal amplitude of WG_m mode when WG_m is excited
a_{cm}^s	Final coupled modal amplitude of WG_m mode when slab TM_0 is excited
a_{sm}^c	Final coupled modal amplitude of slab TM_m mode when WG_m is excited
A	Vector for modal amplitudes
A_0	Complex spectrum amplitude of reference pulse
A_1, A_2	Complex spectrum amplitudes of the first and the second cavity pulses
b	Half thickness of dielectric slab, m
$b(\theta)$	θ -dependent modal amplitude of ring b
c	Speed of light in free space, m/sec
C	Matrix of coupling coefficients
C_{pq}	Coupling coefficient, 1/rad
CMT	Coupled mode theory
e	Normalized electrical field, V/m
e^t	Transverse component of normalized electrical field, V/m

e^z	z component of normalized electrical field, V/m
e_{cm}^r, e_{cm}^θ	r and θ components of normalized electrical field of cylindrical WG_m mode, V/m
e_{gm}^y, e_{gm}^z	y and z components of normalized electrical field of TM_m mode of metal plate waveguide, V/m
e_{sm}^y, e_{sm}^z	y and z components of normalized electrical field of slab TM_m mode, V/m
E	Electrical field, V/m
E^t	Transverse component of electrical field, V/m
E^x, E^y, E^z	x, y and z components of electrical field, V/m
f	Frequency, Hz
f_{gm}	Cutoff frequency of TM_m mode of metal plate waveguide, Hz
f_{sm}	Cutoff frequency of slab TM_m mode, Hz
FWHM	Full width at half maximum
h_{cm}^x	x component of normalized magnetic field of cylindrical WG_m mode, A/m
h_{gm}^x	x component of normalized magnetic field of TM_m mode of metal plate waveguide, A/m
H	Magnetic field, A/m
H_0	Complex frequency transfer function for main transmitted pulse
H_1, H_2	Complex frequency transfer functions for the first and the second cavity pulses
H^x, H^z	x and z components of magnetic field, A/m
H^θ	θ component of magnetic field, A/m

$H_l^{(1)}$	Hankel function of the first kind of order l
i	$\sqrt{-1}$
I	Complex spectrum of input pulse
\mathbf{J}	Current density, A/m ²
J_l	Bessel function of the first kind of order l
k	Free-space wavenumber, 1/m
KLM	Kerr-lens mode-locked
l	Order of Bessel functions; angular propagation constant of WG mode
l_m	Angular propagation constant of WG _{m} mode
m	Order of mode
M	Matrix of mode mapping coefficients
M_{pq}	Mode mapping coefficient
n_1, n_2	Refractive indexes of media 1 and 2
n_c	Refractive index of cylinder
n_{cm}	Effective refractive index of cylindrical WG _{m} mode
n_g	Refractive index of filling material of metal plate waveguide
n_s	Refractive index of slab
n_{sm}	Effective refractive index of slab TM _{m} mode
N_{cm}	Normalization constant for cylindrical WG _{m} mode, m ² /V ²
N_{gm}	Normalization constant for TM _{m} mode of metal plate waveguide, m ² /V ²
N_{sm}	Normalization constant for slab TM _{m} mode, m ² /V ²
t	Time, s
TEM	Transverse electric and magnetic

TM	Transverse magnetic
TM _{<i>m</i>}	<i>m</i> th order TM mode
U _{<i>m</i>}	Core modal parameter for slab TM _{<i>m</i>} mode
v _{<i>cn</i>}	Phase velocity for cylindrical WG _{<i>n</i>} mode
v _{<i>sm</i>}	Phase velocity for slab TM _{<i>m</i>} mode
W _{<i>m</i>}	Cladding modal parameter for slab TM _{<i>m</i>} mode
WG	Cylindrical whispering-gallery mode with $E^x = 0$ and $H^\theta = 0$
WG _{<i>m</i>}	<i>m</i> th order WG mode
WGM	Whispering-gallery mode
Y	Normalized position in <i>y</i> direction (= <i>y</i> / <i>b</i>)
\hat{z}	Unit vector in <i>z</i> direction
β	Propagation constant, rad/m
β_{gm}	Propagation constant for TM _{<i>m</i>} mode of metal plate waveguide, rad/m
β_{sm}	Propagation constant for slab TM _{<i>m</i>} mode, rad/m
ε	Variation in relative permittivities when both rings <i>a</i> and <i>b</i> are present
ε_0	Free-space permittivity, F/m
$\varepsilon_1, \varepsilon_2$	Relative permittivities for media 1 and 2
$\varepsilon_a, \varepsilon_b$	Variations in relative permittivities when only ring <i>a</i> or ring <i>b</i> is present
$\varepsilon_a, \varepsilon_b$	Relative permittivities for ring <i>a</i> and <i>b</i> (inside dielectric)
ε_r	Relative permittivity
η	Characteristic impedance, Ω
η_0	Intrinsic impedance of free-space, Ω

η_{TE}	Characteristic impedance for TE mode, Ω
η_{TM}	Characteristic impedance for TM mode, Ω
η_{p0}	Characteristic impedance for p th mode in free-space, Ω
η_{pd}	Characteristic impedance for p th mode in dielectric, Ω
μ_0	Free-space permeability, H/m
$\hat{\theta}$	Unit vector in θ direction
τ_1, τ_2	Time delays for the first and the second cavity pulses, s
ω	Angular frequency, rad/s

CHAPTER I

INTRODUCTION

1.1 Whispering-Gallery Mode Resonators

The whispering-gallery mode (WGM) represents the electromagnetic wave that circulates around the inner surface of a dielectric resonator owing to total internal reflection [1-3]. The resonator, which can be either a sphere or a cylinder, is usually made of a dielectric material with high dielectric permittivity and low loss. In the spherical case, the electromagnetic field of WGM modes is confined in annular “equatorial” area close to the resonator surface. In the cylindrical case, the wave runs in the plane of the circular cross-section, and most of the modal energy remains confined between the cylindrical boundary and a modal caustic.

In microwave region, conventional cylindrical dielectric resonators are used in many passive and active microwave components, where the resonators act on their TE or TM modes. At millimeter wavelengths, resonators of such kind result in exceedingly small

dimensions and their Q -factors are strongly reduced. WGM resonators, however, can overcome this serious defect, and are hence very suitable for millimeter wave integrated circuits. Such resonators have been used for frequency filters [4] and power combiners [5] in the millimeter-wavelength integrated circuits.

In optical range, the optical cavity has attracted considerable research interest with its important applications in laser design [6], cavity-ring-down spectroscopy [7], fiber optics [8], and basic research such as cavity quantum electrodynamics [9]. The WGM plays an important role in optical cavities. In this frequency range, the WGM resonator is usually a dielectric microsphere. The high Q value guarantees the building up of the electromagnetic field of a certain frequency, which is very important in the applications of frequency selection [3], spectroscopy [10], and parameter detection [11-13].

A WGM resonator is usually excited by the external evanescent fields of the coupler, which can be a dielectric prism [3], a tapered optical fiber [8], transmission lines [2], or a dielectric waveguide [14-16]. When the electromagnetic wave of the coupler passes the coupler-resonator contact region, part of the coupler field is coupled into the resonator and propagates around its inner surface. The coupling sources have been focused mainly on single frequency waves. In this case, the coherence condition must be met for constructive interference; in other words, the circumference of the resonator must be an integer number of wavelengths of the resonant WGM. Only a set of discrete frequency points can satisfy this condition and survive the continuous coupling. These frequency points, which can be called eigen-frequencies, are usually determined by the dimensions

and material properties of the resonator, coupling conditions, and the polarization of the coupling source. A WGM resonator with environment-sensitive dimensions can be used as parameter detectors of its surrounding environment, such as strain [11,12] and humidity [13]. Such detection is usually achieved by measuring the change of the eigen-frequencies of the WGM resonator caused by the change of its dimensions due to the change of the environmental parameters.

The applications of WGM resonators are not limited by those mentioned above. With high quality factor, size flexibility, wide working frequency range, mechanical stability, and adaptability to integrated circuits, WGM resonators are widely used for basic research and application purposes, including non-linear optics [17,18], measurement of dielectric parameters [16,19], and evanescent-wave sensing [20].

1.2 Terahertz Time Domain Spectroscopy System

Since the generation of the subpicosecond (subps) terahertz (THz) radiation by using fast photoconductive switches driven by short laser pulses was first demonstrated [21,22], THz technology has been a new research frontier, and has become a bridge to connect the microwave technology at the lower frequency end and the optical technology at the higher frequency end. Many research topics in the above two frequency regions have been expanded to THz region, and THz technology has found its important application in

such diverse fields as spectroscopy [23], imaging [24,25], ranging [26], and basic material characterization [27,28].

A typical THz time domain spectroscopy (THz-TDS) system consists of a THz transmitter (generator), beam collecting and steering system, and a THz receiver (detector). Both the THz transmitter and receiver are switched by pulsed laser beam. By changing the time delay between the excitation and detection laser beams, a THz time domain pulse scan is obtained with both the amplitude and phase information. The complex spectrum with amplitude and phase information can then be retrieved by applying digital Fourier transform to the time domain pulse. A sample scan can be compared with a reference scan to obtain the properties of the sample.

A simple, easy and broadly used method to generate and detect the THz pulse is the photoconductive antenna, which uses the coplanar transmission lines as the transmitter and receiver for the THz radiation [22,23,26-29]. In this system, silicon is broadly used in collecting and focusing the THz radiation due to its low-loss and low group velocity dispersion in THz range [23]. To increase the signal-to-noise ratio (SNR), the THz beam is chopped by an optical chopper and a lock-in amplifier is used to amplify the chopped signal.

1.3 Terahertz Waveguides

Guided-wave propagation of the THz radiation has attracted much interest as the applications of THz technology have greatly expanded. For freely propagating THz beams, subps THz pulses can propagate hundreds of centimeters without pulse distortion [23,30]. On the other hand, the propagation on coplanar transmission lines cannot exceed 1 cm, owing to the Cherenkov-like radiation [31]. This radiation loss is eliminated when the microstrip line is used with silicon-on-insulator materials, but the total observed loss owing to the dielectric and metal is still approximately the same as for the coplanar transmission line [32].

The first experimental demonstration of THz waveguides was achieved by coupling the freely propagating THz radiation into circular metal tubes using quasi-optical methods [33], where the THz radiation propagated for up to 24 mm in the waveguide with low loss. However, due to the dispersive nature of the waveguide modes and the multimode coupling, the transmitted THz pulses were greatly broadened in time domain, and spectral oscillations were observed in the frequency domain [34]. Single-mode transmission of THz pulses has been demonstrated in dielectric circular [35] and planar ribbon waveguides [36], with the outstanding problems of pulse broadening and frequency chirp. The first low-loss, non-dispersive propagation of THz pulses is achieved by using parallel metal plates as waveguides [37,38], where the THz pulses propagate for up to 250 mm in the metal waveguide with negligible pulse distortion.

The above progress in THz waveguide study has made possible the guided wave propagation and circuit interconnection of the THz radiation. It is expected that the rapidly advancing THz technology will find important applications in new areas only previously available to optical or microwave techniques.

1.4 Purpose of This Study

As the WGM resonators play an important role in the optical and microwave regions, it is of great interest and much importance to investigate the coupling and propagation properties of a WGM cavity for the THz radiation. With the progress in the THz waveguide study [33-38], a THz WGM cavity will soon be required in the THz integrated circuits. In other WGM-related studies, the coupling source is usually a single frequency cw laser [3,39]. However, the THz radiation usually has a time duration of several picoseconds, and covers a continuous frequency range from 0 to up to 5 THz. This unique feature will definitely show different coupling and propagation properties.

This dissertation presents an experimental demonstration of a cylindrical WGM cavity for the THz radiation [15]. The WGM cavity is a dielectric cylinder and the THz pulses are coupled into and out of the cavity via a dielectric slab waveguide. The coupled WGM pulses cover a continuous frequency range of 0.4—1.8 THz and consists of a superposition of several WGM modes. Two cavity pulses are observed from this slab-

cylinder coupling structure and thereby demonstrate the strong coupling of this coupling structure and the propagation properties of the WGM THz pulses [15].

The detailed coupling structures will be given in Chapter II as well as the coupling scheme. In the theoretical part, the modal analysis for both the slab waveguide and the cylindrical WGM cavity are both presented. A theory governing the coupling – coupled mode theory (CMT) – is derived and used to analyze the slab-cylinder coupling structure. The numerical calculations show reasonably good agreement with the experiment in both the frequency and time domains, and give a good explanation to the coupling behavior between the slab waveguide and the cylinder and propagation properties of the WGM THz pulses.

CHAPTER II

EXPERIMENTAL SETUP

AND

COUPLING STRUCTURES

The experimental setup is a standard THz time-domain spectroscopy (THz-TDS) system [30] presented in Fig. 2-1. A 40-femtosecond laser pulse train with a nominal wavelength of 820 nm and a repetition rate of 100 MHz, generated by a KLM Ti:Sapphire laser which is pumped by a Spectral Physics Millennia cw laser, is focused onto a coplanar stripline biased at 75 V on a semi-insulating GaAs wafer. The focus point is at the inner edge of the positive polarity line. This periodic optical pulse excitation causes pulsed, subps changes in the conductivity of the gap between the two lines, which results in pulses of electrical current, and consequently, bursts of electromagnetic radiation in the THz range. After passing through the GaAs substrate, a large fraction of this THz radiation is collected and collimated by a hyper hemisphere silicon lens attached to the back side of the GaAs wafer; then the THz beam propagates to a paraboloidal reflection mirror where it is recollimated to a highly directional beam. An

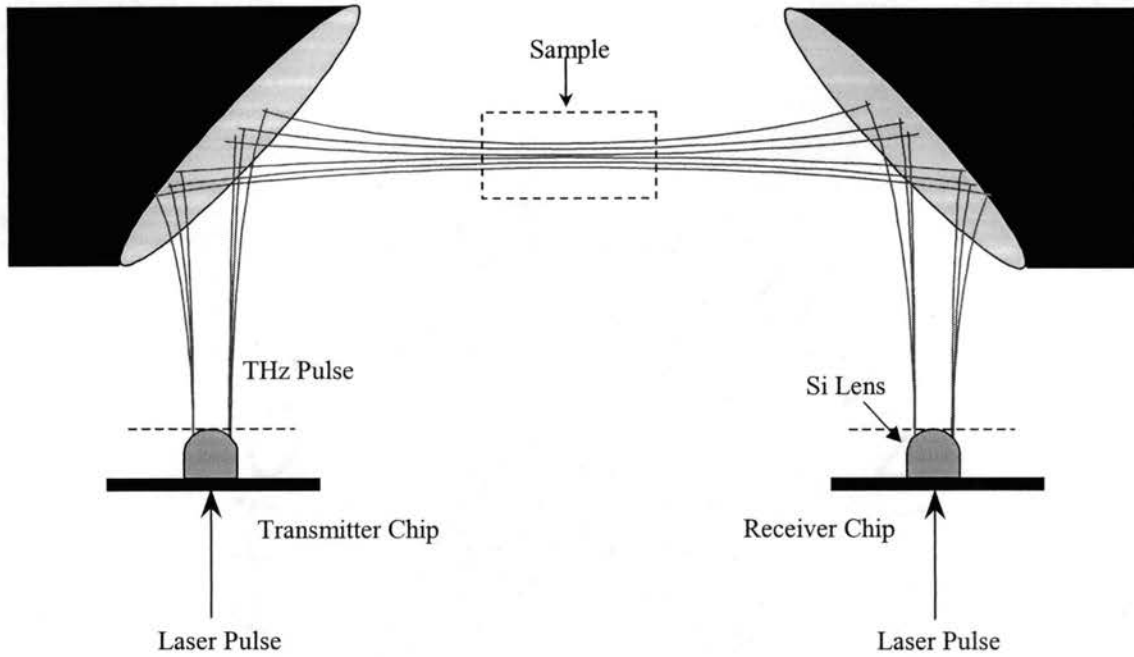


Fig. 2-1 Experimental setup.

identical combination of optics on the receiver side collects the THz beam. A paraboloidal mirror collects and steers the incoming THz beam to a silicon lens, which focuses it onto a $10\ \mu\text{m}$ dipole antenna on an ion-implanted silicon-on-sapphire (SOS) wafer. The electrical field of the focused THz radiation induces a transient bias voltage across the receiving antenna, which is photoconductively switched by a second optical pulse train from the same laser. A dc current proportional to the instantaneous electrical field is thus generated and pre-amplified by a low-noise current amplifier. In order to increase the signal-to-noise ratio (SNR), the THz beam is chopped by an optical chopper placed right after the silicon lens at the transmitter side. A lock-in amplifier then detects the pre-amplified current at the reference frequency provided by the chopper, and a computer data acquisition system records and analyzes the digital output data from the

lock-in amplifier. By scanning the relative delay between the two laser beams, the complete time dependence of the THz pulse including both the amplitude and phase information can be obtained.

In order to eliminate the effects of water vapor [40] on the THz beams, the entire setup is enclosed in a large airtight box that is purged and kept at positive pressure by dry air during the data collection.

Fig. 2-2a shows a scan taken with the above setup purged by dry air. The positive peak of this output pulse has a FWHM of approximately 0.32 ps. Taking discrete Fourier transform of this scan, we get its complex spectrum profile, with the amplitude part shown in Fig. 2-2b. This setup has a smooth frequency response ranging from 0 THz to above 3 THz. The small oscillations in the spectrum are absorption lines from the residual water vapor [40], which can be removed by longer time of purging with dry air.

For a standard THz-TDS measurement, the sample under investigation is usually placed at the waist of the THz beam in between the two paraboloidal mirrors [27,28]. In our case, the sample is the slab-cylinder coupling structure with plano-cylindrical lenses, which is placed in the central position between the two paraboloidal mirrors. As illustrated in Fig. 2-3, we use two similar coupling structures, both composed of a silicon cylinder and a silicon slab waveguide sandwiched between two metal plates with an open window in the middle. Here is the detailed information of the dimensions of the two coupling structures:

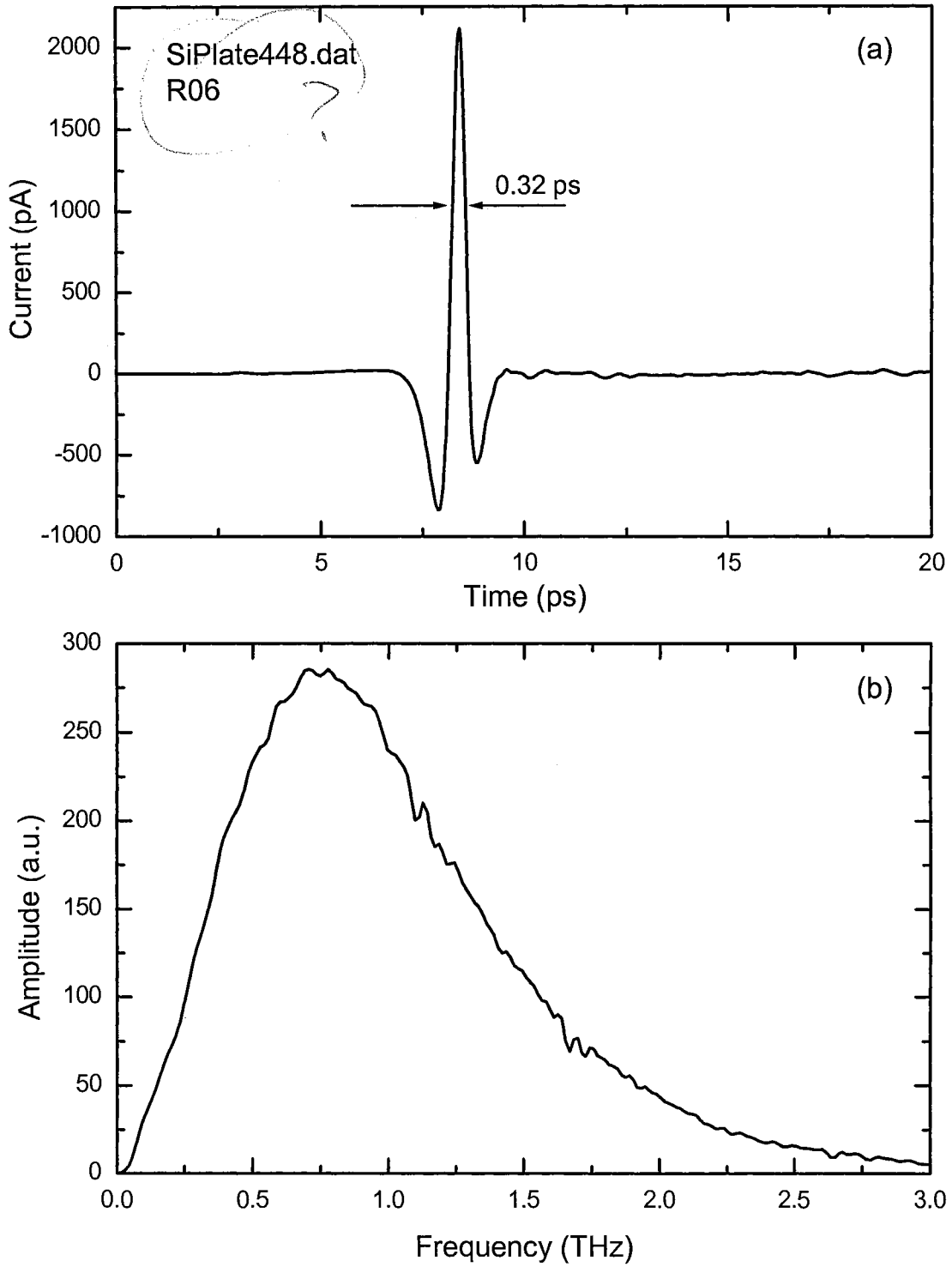


Fig. 2-2 (a) The output scan and (b) the spectrum profile of the THz setup.

A. Silicon cylinder: 5 mm (diameter) \times 10 mm (height- x);

Silicon slab waveguide: 20 mm (length- z) \times 100 μm (thickness- y) \times 20 mm (height- x);

Aluminum plates: identical, 24.5 mm (length- z) \times 5 mm (thickness- y) \times 40 mm (height- x), with open window of 7 mm (length- z) \times 17 mm (height- x) in the middle.

B. Silicon cylinder: 5 mm (diameter) \times 10 mm (height- x);

Silicon slab waveguide: 17.5 mm (length- z) \times 100 μm (thickness- y) \times 12.5 mm (height- x);

Aluminum plates: both are 18 mm (length- z) \times 40 mm (height- x) with open

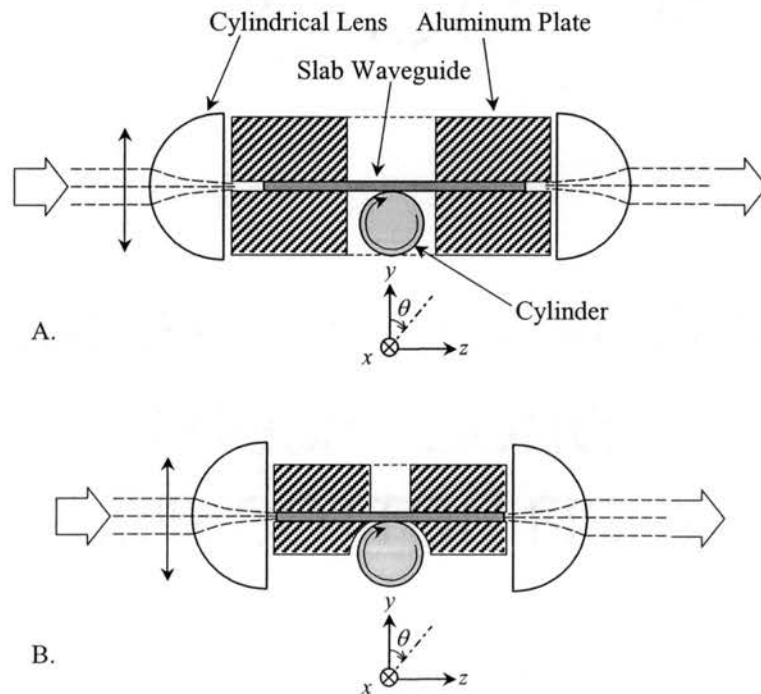


Fig. 2-3 Cross sections of the slab-cylinder coupling structures A and B.

window of $3.2 \text{ mm} \times 17 \text{ mm}$ (height- x) in the middle; the thicknesses are 4 mm (top) and 2.5 mm (bottom); the open window of the bottom plate is carefully milled out using a 6.2-mm-diameter ball-end bit to place the cylinder in contact with the slab waveguide.

The two plano-cylindrical lenses, the slab waveguide, and the cylinder are all made of high-resistivity silicon, which has very low energy absorption and almost no dispersion at THz frequency range [23]. The plano-cylindrical lenses are used to couple the incoming THz beam into and out of the slab waveguide [36,37]. The lens at the input of the guide is used to focus the beam along only the y -direction, producing an approximately Gaussian beam having an elliptical cross section at the waist, with a frequency-independent $1/e$ -amplitude minor axis of $200 \mu\text{m}$ [36,37]. An identical optical arrangement is used at the exit face. In order to confine the beam height of the incoming THz pulse, a 3-mm (height- x) and a 5-mm-diameter aperture is placed before the left lens for structures A and B, respectively.

The metal plates in the coupling structures serve as a firm holder for the thin slab waveguide, so the latter does not change its position when the cylinder is brought into contact with it. The incoming THz beam is focused by the cylindrical lens and is coupled into the metal waveguide formed by the metal plates filled with air or the silicon slab. In the air-filled metal plate waveguide, the THz pulse propagates in a single TEM mode with negligible dispersion and loss [37]. In the case of silicon-filled metal plate waveguide, if there is no air gap between the silicon slab and the metal plates, the THz

pulse will also couple dominantly into TEM mode. In experiment it is difficult to get an intimate contact between the silicon slab and the metal plates, so an air gap may exist between the silicon slab and the metal plates. In this case the THz pulse will not couple into a pure TEM mode. However, in the analysis, we will still assume that the THz pulse propagates in the TEM mode of the silicon-filled metal plate waveguide. This assumption will not affect our numerical analysis, as will be seen in Chapter VI.

In the open window region, the pulse propagates dominantly in the TM_0 mode of the slab waveguide with high group velocity dispersion [36], which causes pulse broadening and frequency chirp. This pulse broadening can be reduced by reducing the length of the open window, as will be seen in the experimental results.

When the cylinder is brought into contact with the slab waveguide in the open window area, part of the incoming THz pulse will be coupled into the cylinder as a linear combination of cylindrical WGM modes; the remaining pulse continues to propagate along the beam path of the system and is detected as the main transmitted pulse. The WGM-THz pulse travels continuously around the cylinder. When it returns to the slab-cylinder contact region after one round trip, part of this pulse will be coupled into the slab waveguide and will arrive at the THz receiver to be recorded as the first cavity pulse. As this coupling occurs every time the circulating WGM-THz pulse returns to the contact region, a cavity pulse train is generated. This process is illustrated in Fig. 2-4.

Originally we made only structure A for our experiment. After experiment with structure

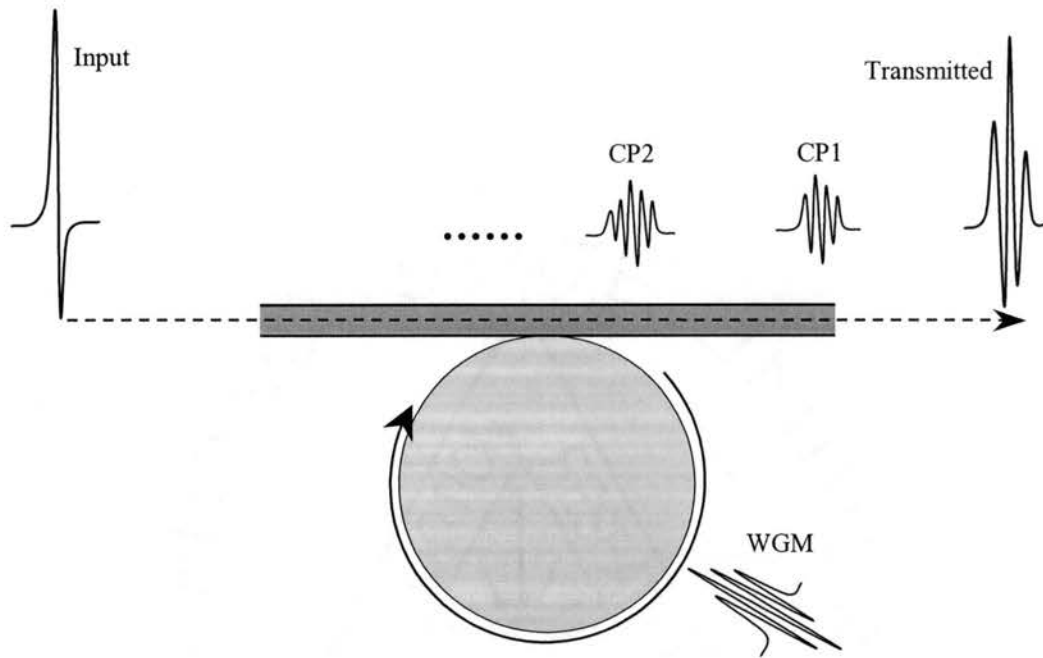


Fig. 2-4 Illustration of the coupling between the slab and the cylinder. CP stands for cavity pulse.

A, we made structure B to improve the experimental results. The main difference between the two structures lies in the lengths of the open windows. If the cylinder is not present, in the reference scan we will obtain a main transmitted pulse and some reflection pulses. The dominant reflection pulses will be those from the cylindrical lenses. As the transmitted pulse is broadened by the propagation in the open window area, the reflection pulses are also expected to have the similar broadening. As will be seen in the scans, the delay of one reflection pulse is very close to the first cavity pulse. By reducing the length of the open window, the pulse broadening effect will be reduced for the transmitted pulses, and hence for the reflection pulses. This reduction gives a longer time window for the cavity pulse where there is no background pulse in the reference scan, so that a clearer cavity pulse can be obtained. Structure B has an open window of 3.2 mm,

compared with 7 mm for structure A, so the transmitted pulse width for structure B will be much shorter than that for structure A. We expect that we can obtain a better scan of cavity pulses for structure B.

In the scan we will also get a reflection pulse from between the planar surface of the cylindrical lens and the entrance (exit) surface of the silicon slab. The distance between the two surfaces is approximately 3 mm for structure A and 0.7 mm for structure B, corresponding to a time delay of about 20 ps and 4.7 ps, respectively. This delay is small compared to the pulse width of the main transmitted pulse, so the reflection pulse will be added to the main transmitted pulse and contributes to its broadening. For this reason, structure B will get less pulse broadening from this reflection pulse, due to its shorter time delay compared with that for structure A.

For structure B, we also improve the cylinder holder. Fig. 2-5 illustrates the cylinder holders we used for the two structures. For structure A, the holder head is attached to a plastic bar with a piece of sponge. The plastic bar is able to move in three translational directions x , y , and z , and can rotate in x - z plane. The purpose of using the sponge is to avoid any damage to the silicon slab waveguide when the cylinder is brought in contact with it. However, since the sponge is very flexible, when rotated in x - z plane, the cylinder may not rotate accordingly, making it very difficult to vertically align the cylinder. To solve this problem, we place two parallel plastic plates on both sides of the holder in the sponge area, so the cylinder will rotate along with the plastic bar. This allows us to vertically align the cylinder so that the axial direction of the cylinder is

parallel to x direction.

In experiment, we observed the first two cavity pulses for both the coupling structures. The following chapters will present the experimental results and the theory used to analyze this coupling structure.

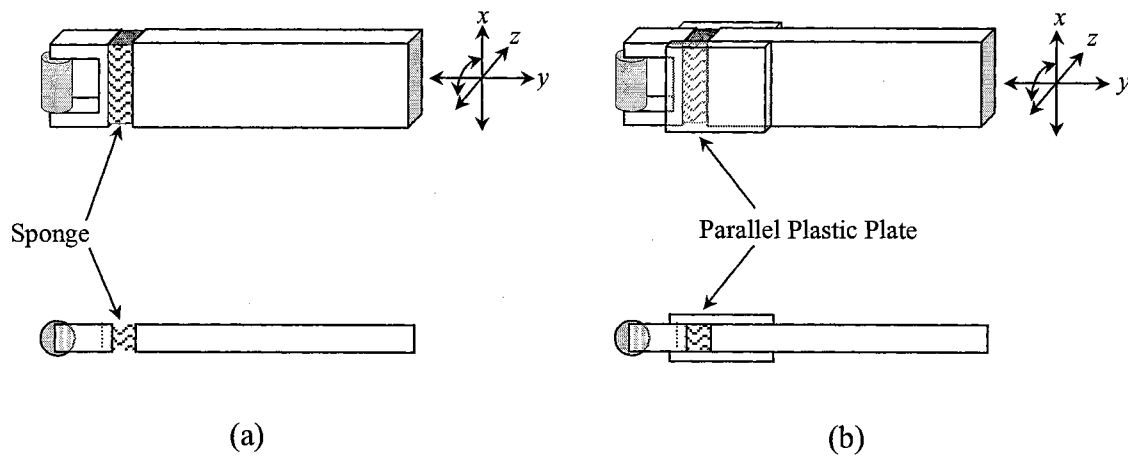


Fig. 2-5 Cylinder holders for (a) structure A and (b) structure B. The bottoms are the top views.

CHAPTER III

EXPERIMENTAL RESULTS

3.1 The Input Pulse

In experiment, the coupling structure including the two plano-cylindrical lenses as shown in Fig. 2-2, is placed in between the two paraboloidal mirrors of the THz-TDS system [36,37], as indicated by the dotted rectangular in Fig. 2-1. The input pulse is measured by removing the coupling structure and moving the cylindrical lenses to their confocal position [36,37]. This pulse is presented in Fig. 3-1 along with its spectrum. As shown in the figure, this pulse has a smooth spectrum and a narrow pulse width, with a FWHM of 0.27 ps for the big positive peak. Compared with the spectrum shown in Fig. 2-2, this spectrum has a very smooth profile without any spectral oscillations, indicating that the system contains no water vapor as a result of the long purging time by dry air.

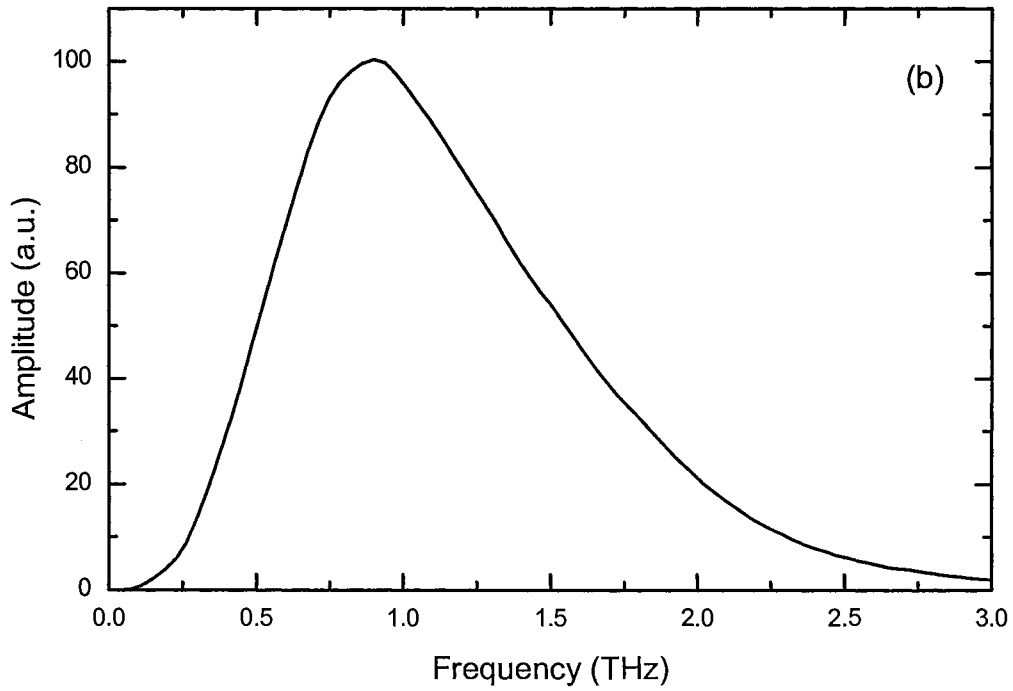
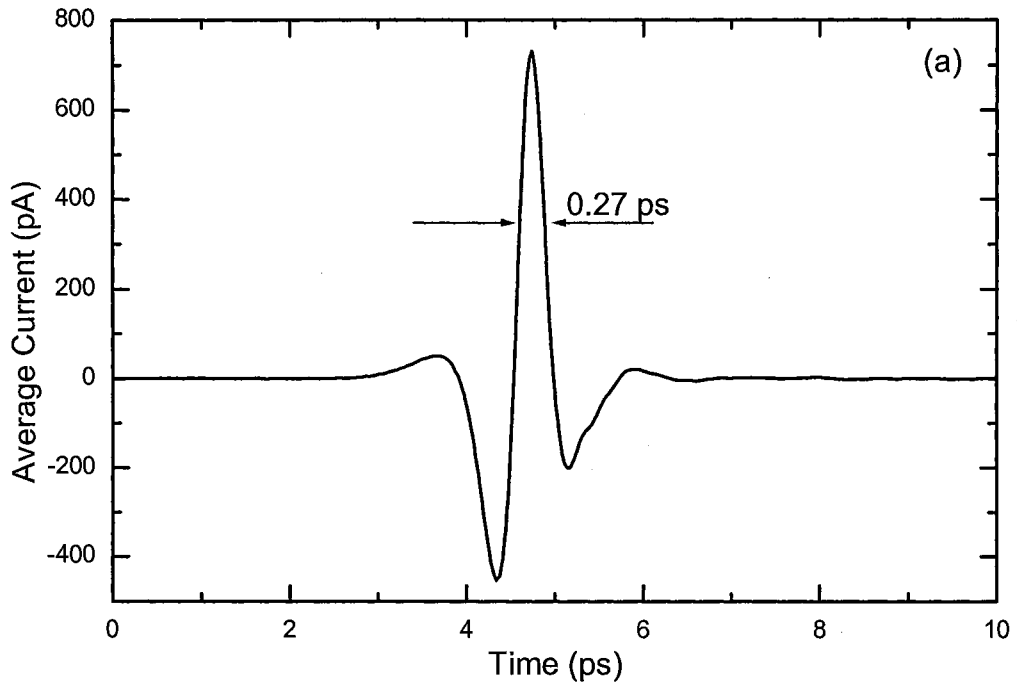


Fig. 3-1 (a) Measured input pulse and (b) its spectrum.

3.2 Results from Structure A

For the coupling structures A and B, the reference scan is taken without the cylinder, and the sample scan is taken when the cylinder is brought into contact with the slab waveguide in the open window region. By comparing the reference scan and the sample scan, the coupling properties and the propagation properties of the WGM THz pulses can be retrieved.

For the coupling structure A, the reference scan is presented in Fig. 3-2a, which shows that the main transmitted pulse is followed by two smaller pulses R1 and R2, the first and the second reflection pulses from the cylindrical lenses. Compared with the input pulse in Fig. 3-1, the three pulses are extremely broadened due to the 7 mm propagation in the open window area, with a FWHM of about 10 ps for the main transmitted pulse. The sample scan is shown in Fig. 3-2b. In addition to the three pulses in the reference scan, three new pulses CP1, CP2 and RCP1 appear in the sample scan.

As described in Chapter II, when the cylinder is brought into contact with the slab waveguide, a WGM-THz pulse will be formed inside the cylindrical cavity and a cavity pulse train will be generated. If we assume the WGM-THz pulse travels around the cylinder at a velocity equal to that in the bulk silicon, the time delay between the first cavity pulse and the main transmitted pulse can be calculated as

$$\tau_1 = 2\pi n_c a / c, \quad (3-1)$$

where $n_c = 3.417$ is the refractive index of the cylinder (silicon) [23], $a = 2.5$ mm is the

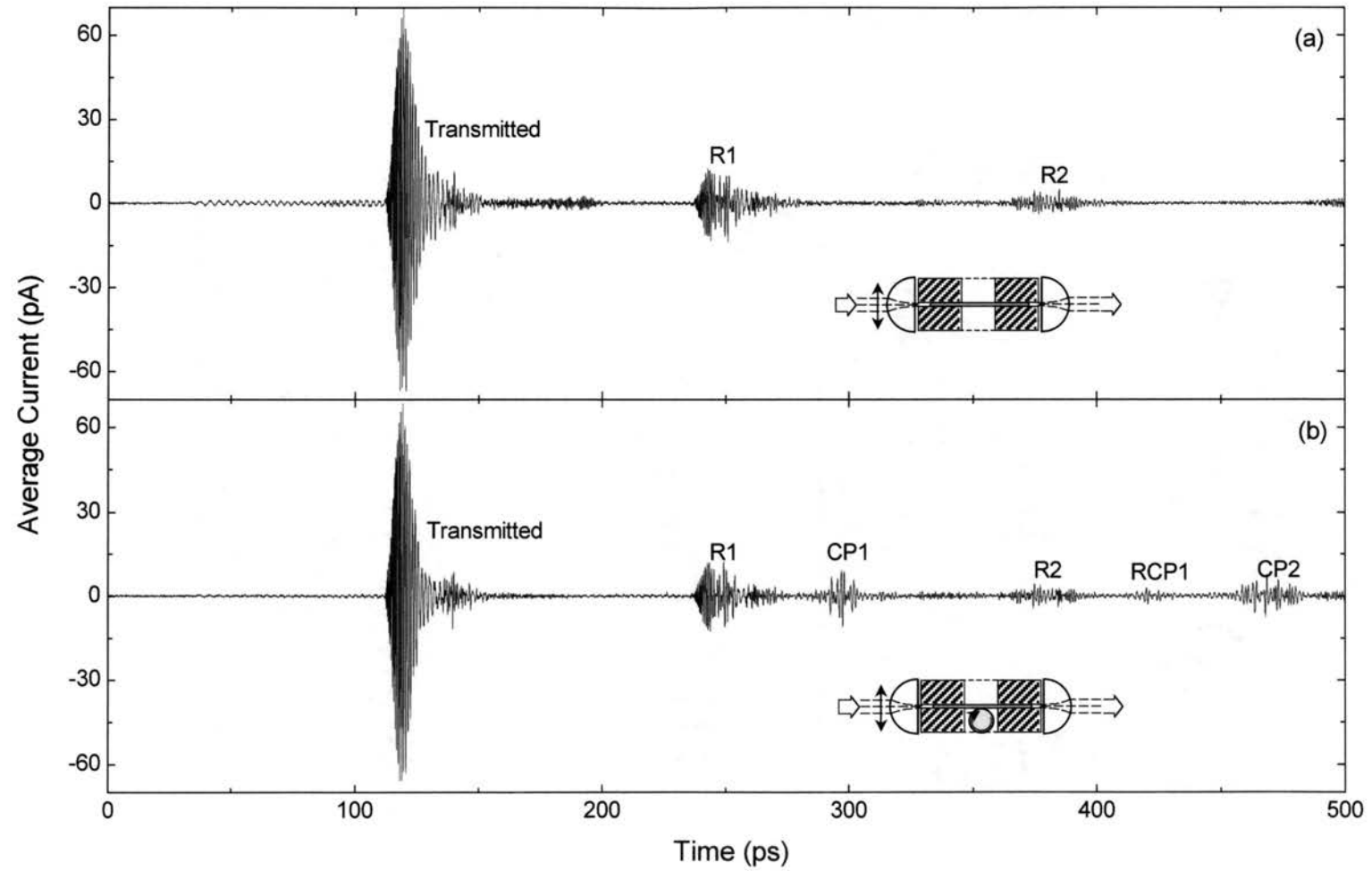


Fig. 3-2 Measured time domain pulses for coupling structure A. (a) Reference scan without cylinder. (b) Sample scan with the cylinder in contact with the slab waveguide.

radius of the cylinder, and c is the speed of light in free space. Substituting the corresponding values into the above equation, we get $\tau_1 = 179$ ps, which is in excellent agreement with the experimental delay of 172~187 ps between CP1 and the main pulse; thus pulse CP1 is identified as the first cavity pulse. Accordingly, the second cavity pulse has a time delay of $\tau_2 = 2\tau_1$ relative to the main pulse. The experimental delay of pulse CP2 relative to the main pulse is in the range of 337~367 ps, which is again in good agreement of the calculated value $\tau_2 = 358$ ps; thus pulse CP2 is identified as the second cavity pulse. In addition, with an experimental delay of 170~190 ps relative to pulse R1, pulse RCP1 is identified as the first cavity pulse from pulse R1.

Fig. 3-3 shows the magnifications of Fig. 3-2 for the main transmitted pulses of the reference and sample scans and their corresponding spectra. In the time domain, the intensity of the main pulse remains almost the same when the cylinder is brought into contact with the slab waveguide, except in the leading part, where the small oscillations are greatly suppressed by the slab-cylinder coupling. These oscillations contain the low frequency components with the highest group velocities [36]. The suppression of the oscillations indicates a strong coupling between the slab waveguide mode and the cylindrical WGM modes. In the frequency domain, though accompanied by spectral oscillations, the spectra show the single-mode propagation of the main transmitted pulses, as described in Chapter II. The spectral oscillations, with a frequency period of approximately 0.05 THz, are due to the reflections between the planar surfaces of the cylindrical lenses and the entrance and exit surfaces of the silicon slab, separated by approximately 3 mm.

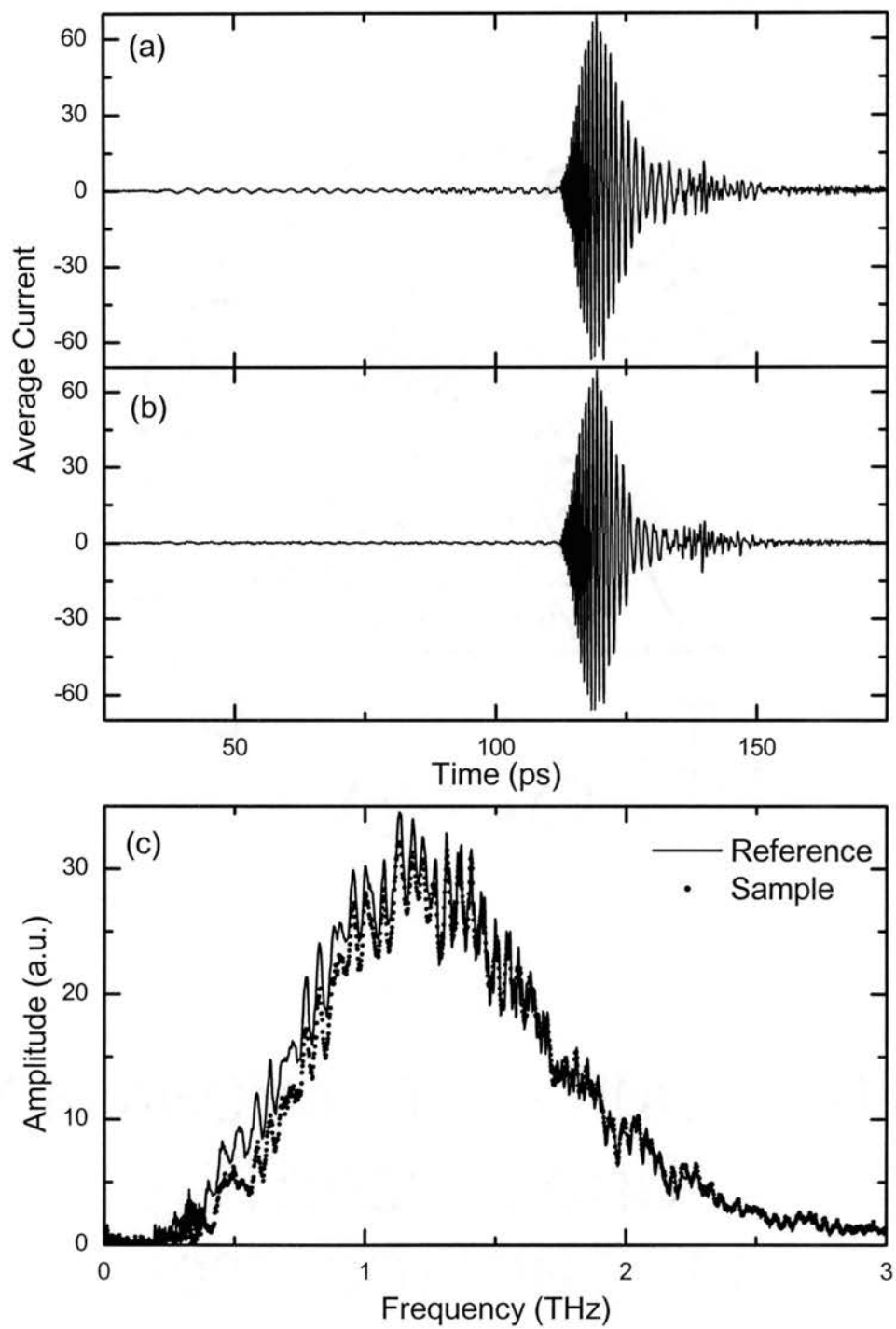


Fig. 3-3 Main transmitted pulses and their spectra for structure A. (a) Reference scan (pulse 1a). (b) Sample scan (pulse 1b). (c) Spectra of pulses (a) and (b).

Figs. 3-4a and 3-4b are magnifications of Fig. 3-2 for the first and the second cavity pulses CP1 and CP2, respectively. Their respective spectra are presented in Figs. 3-5a and 3-5b. Compared with the spectrum of the main pulse (Fig. 3-3c), the spectra of the cavity pulses have complicated structures and oscillations. Since the incoming THz pulse in the slab waveguide is propagating in a single mode, the spectral oscillations in the cavity pulse indicate that the WGM-THz pulse inside the cylindrical cavity is composed of several WGM modes [34]; the oscillations occur because the phase velocities are different for the individual WGM modes and interference occurs when they are coherently combined at the coupling point. The second cavity pulse travels a longer path inside the cylinder, which causes its more complicated spectral pattern compared with the first cavity pulse.

As shown in Fig. 3-5, the spectra of the cavity pulses cover a relatively lower frequency range (0.4 to 1.8 THz) compared with that of the input pulse (Fig. 3-1b), which indicates that the lower frequency components have stronger coupling. This can also be seen in Fig. 3-3. As a result of the strong coupling from the slab waveguide to the cylindrical cavity, for the main transmitted pulse, the intensities of the frequency components in the above range decrease significantly when the cylinder is brought into contact with the slab waveguide (Fig. 3-3c). In the time domain, the small oscillations in the leading part of the main transmitted pulse contain the lower frequency components with the highest group velocities. These oscillations are strongly suppressed in the sample scan as a result of this strong coupling in lower frequency range.

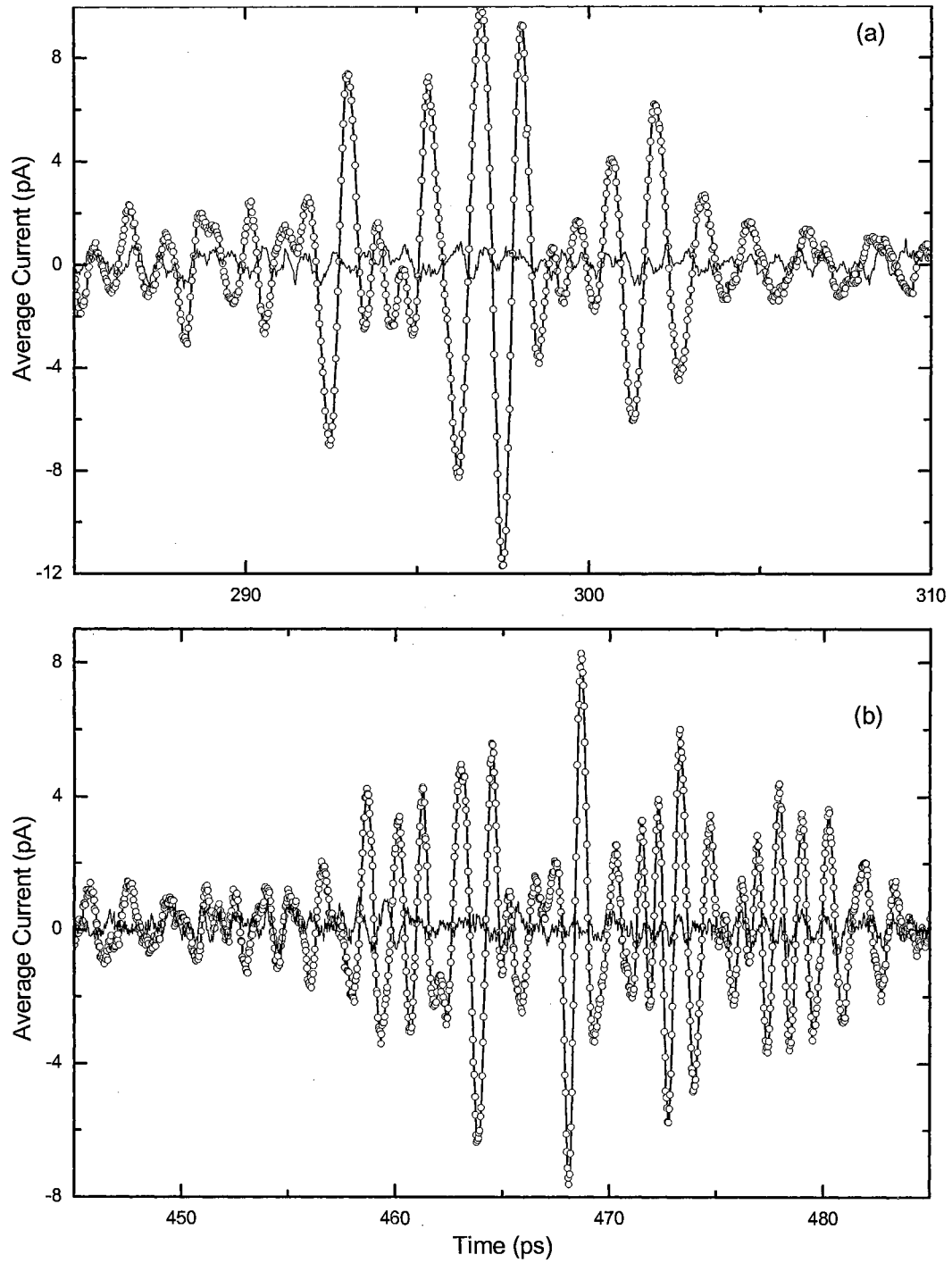


Fig. 3-4 (a) The first and (b) the second cavity pulses (lines with open circles) and their reference pulses (solid lines) for coupling structure A.

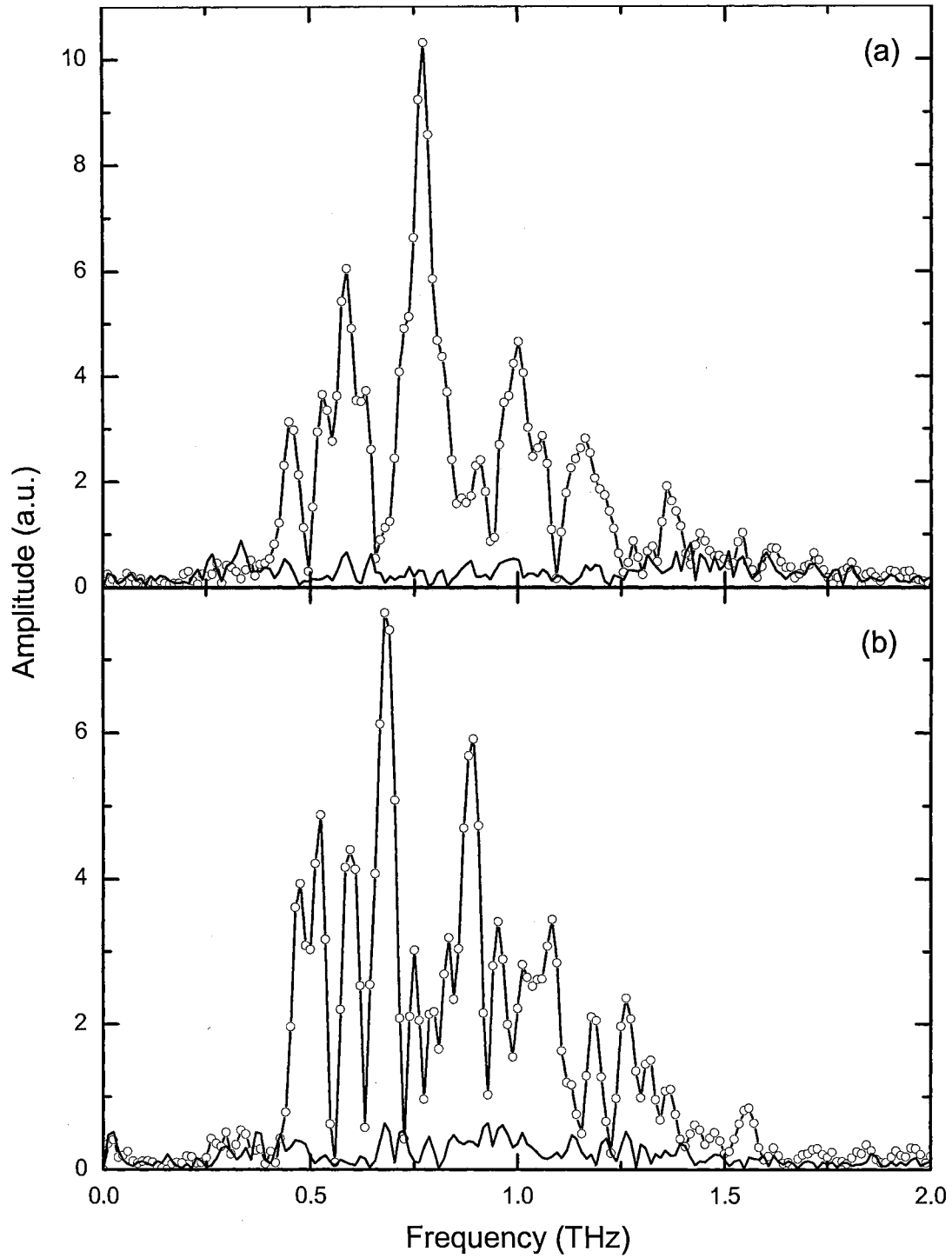


Fig 3-5 The spectra of (a) the first and (b) the second cavity pulses for coupling structure A. The solid lines on the bottom are the spectra of the reference pulses.

From Fig. 3-5, the energy contained in the two cavity pulses can also be compared. If we take the square of the spectrum and then integrate over the frequency range from 0.0 THz to 2.0 THz, we obtain $E_1 = 8.91$ for the first cavity pulse and $E_2 = 4.36$ for the second cavity pulse. Note that these numbers are not the absolute value of the energy, but only give relative amount of energy in the two pulses. It is seen that the second cavity pulse decays dramatically compared with the first one. It should be pointed out that this calculation only gives the comparison of total energy over a certain frequency range, and it cannot be used to calculate the Q value of the cavity.

Compared with the results from other WGM-related studies [3,39], since our coupling source is a subps THz pulse instead of a cw wave, the coherence condition is not required for the coupled WGM modes in the cylindrical cavity; hence the cavity pulses cover a continuous frequency range, instead of the discrete frequency points.

3.3 Results from Structure B

The main difference between structure B and structure A is that the former has a shorter open window. As mentioned in Chapter II, the pulse broadening of the main transmitted pulse is due to the pulse propagation in the dispersive slab TM_0 mode in the open window area. As the length of this open window is reduced, the broadening of the main transmitted pulse is also expected to be reduced. Another difference between the two

structures is that, for structure B, the length of the metal plates is almost the same with that of the silicon slab, so the separation between the planar surfaces of the cylindrical lenses and the entrance and exit surfaces of the silicon slab is much closer, approximately 0.7 mm compared with 3 mm for structure A. This will reduce the reflection-induced spectral oscillations for the main pulses.

The reference and sample scans for structure B are shown in Figs. 3-6a and 3-6b, respectively. Compared with Fig. 3-2 for structure A, similar pulses appear in the two scans and are numbered the same way. As expected, the broadening of the main transmitted pulses is significantly reduced due to the shorter propagation length in the dispersive slab TM_0 mode in the open window area. The main transmitted pulses now have a FWHM of approximately 4 ps, compared with 10 ps for structure A. This reduction in pulse broadening makes it much easier for us to separate the cavity pulses from the reflection pulses, so that we are able to analyze the coupling properties of the slab-cylinder coupling structure more easily.

Fig. 3-7 shows the magnifications of Fig. 3-6 for the main transmitted pulses of the reference and sample scans and their corresponding spectra. In the time domain, the intensity of the main pulse again remains almost the same when the cylinder is brought into contact with the slab waveguide. The reflection-induced spectral oscillations now have a frequency period of approximately 0.23 THz, corresponding to a spatial separation of 0.65 mm between the reflection surfaces, in excellent agreement with our experimental estimation of 0.7 mm for the separation between the planar surfaces of the cylindrical

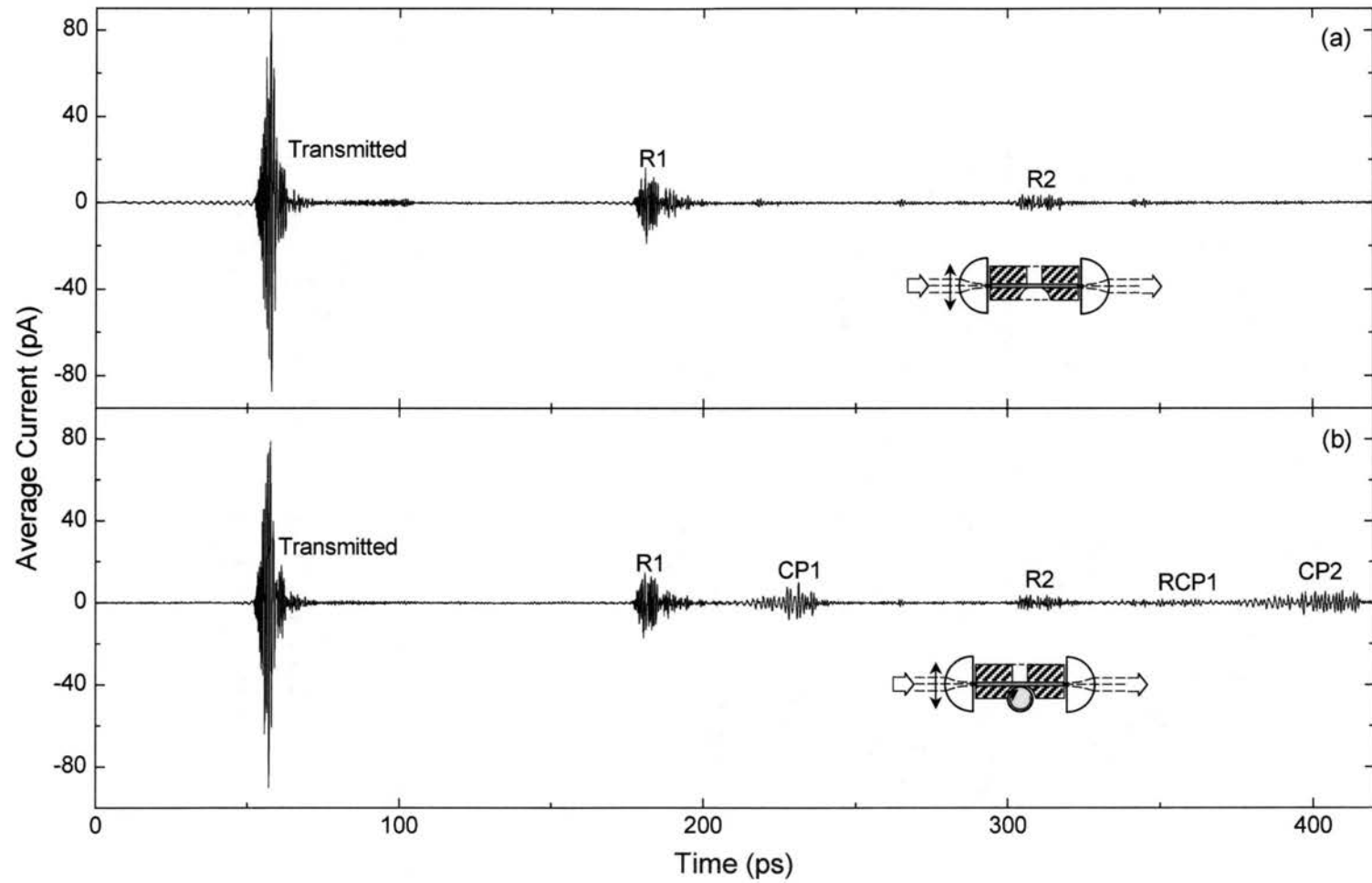


Fig. 3-6 Measured time domain pulses for coupling structure B. (a) Reference scan without cylinder. (b) Sample scan with the cylinder in contact with the slab waveguide.

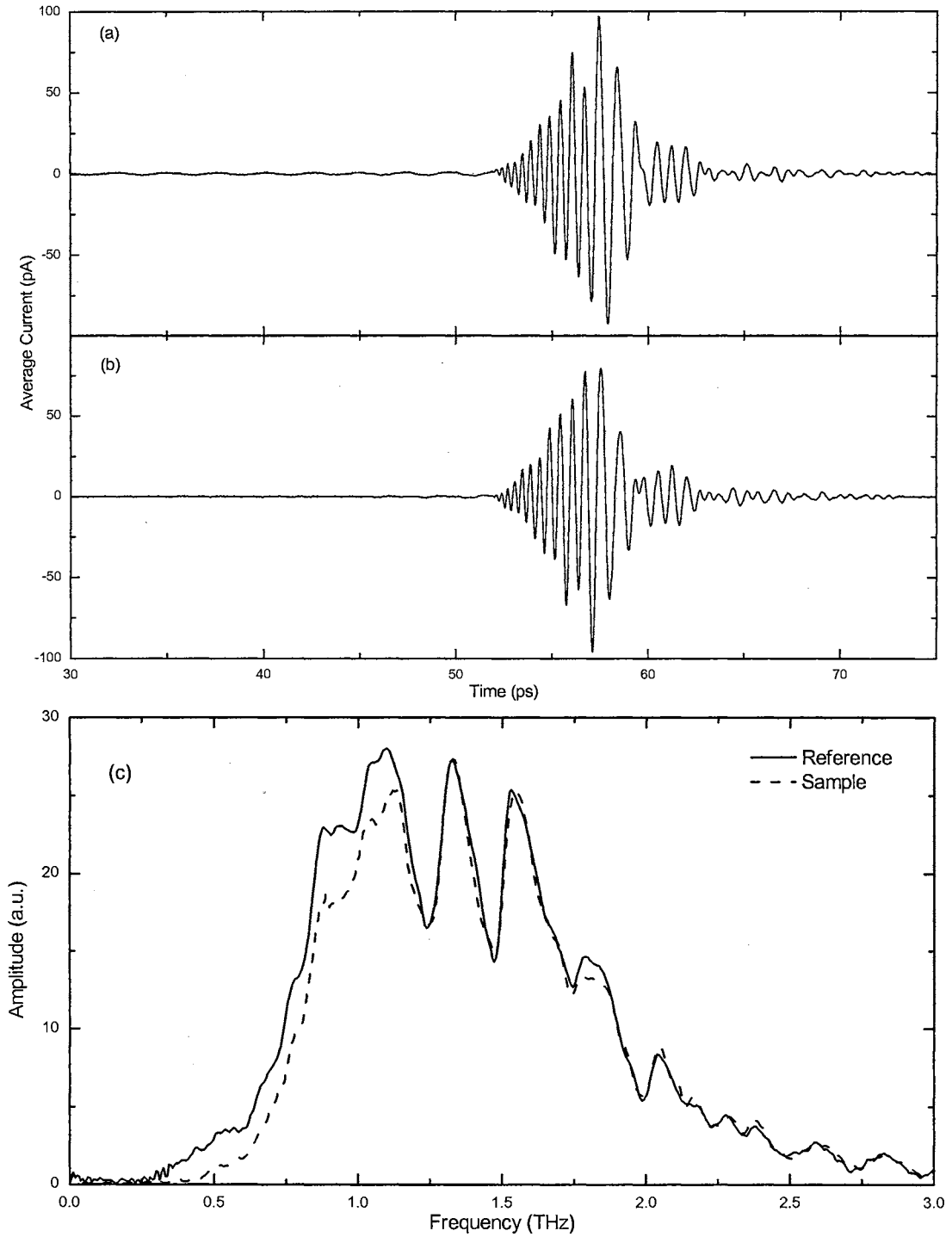


Fig. 3-7 Main transmitted pulses and their spectra for structure B. (a) Reference scan (pulse 1a). (b) Sample scan (pulse 1b). (c) Spectra of pulses (a) and (b).

lenses and the entrance and exit surfaces of the silicon slab. Again the spectra show good single-mode propagation property for the main transmitted pulses. The intensity drop for the low frequency components is clearly seen in the figure when the cylinder is brought into contact with the slab waveguide.

Figs. 3-8a and 3-8b are magnifications of Fig. 3-6 for the first and the second cavity pulses CP1 and CP2, respectively. Their respective spectra are presented in Figs. 3-9a and 3-9b. The cavity pulses show similar properties as those for structure A. However, since the broadening of the main transmitted pulse and therefore of the reflection pulses R1 is significantly reduced, we are now able to obtain a clearer scan for the cavity pulses. Note that the time ranges in Figs. 3-8a and 3-8b are 40 ps and 55 ps, respectively, compared with 25 ps and 40 ps, respectively, for the cavity pulses of structure A shown in Fig. 3-4. The larger time ranges are a result of a higher signal-to-noise ratio as the noise from the reflection pulse is greatly suppressed.

The spectral oscillations still appear in Figs. 3-9a and 3-9b due to the multimode composition of the WGM-THz pulse [34]. The frequency ranges for the two cavity pulses remain the same with those for structure A. As expected, the small oscillations in the leading part of the main transmitted pulse disappear due to the strong coupling of the low frequency components from the slab waveguide to the cylindrical cavity, as shown in Figs. 3-7a and 3-7b.

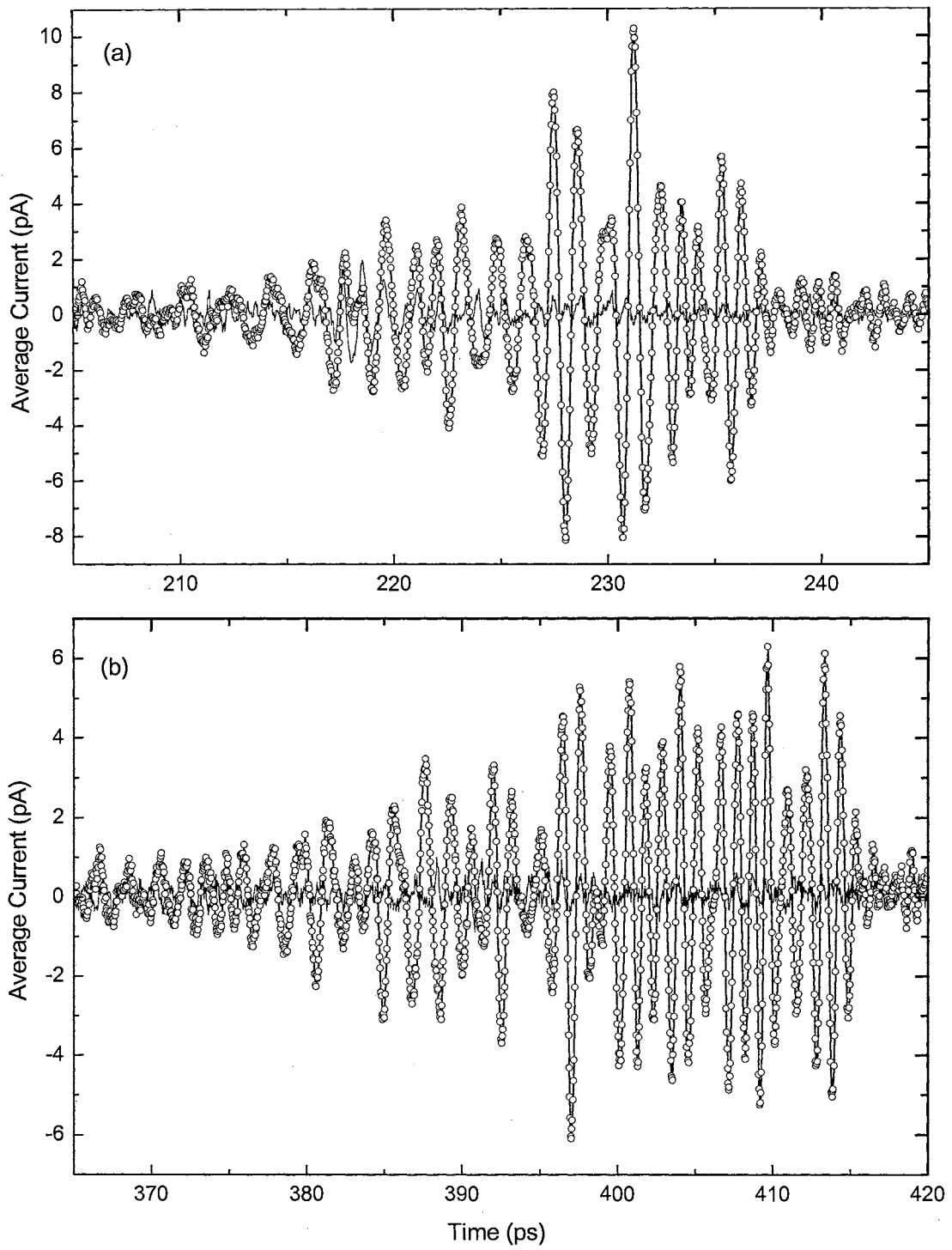


Fig. 3-8 (a) The first and (b) the second cavity pulses (lines with open circles) and their reference pulses (solid lines) for coupling structure B.

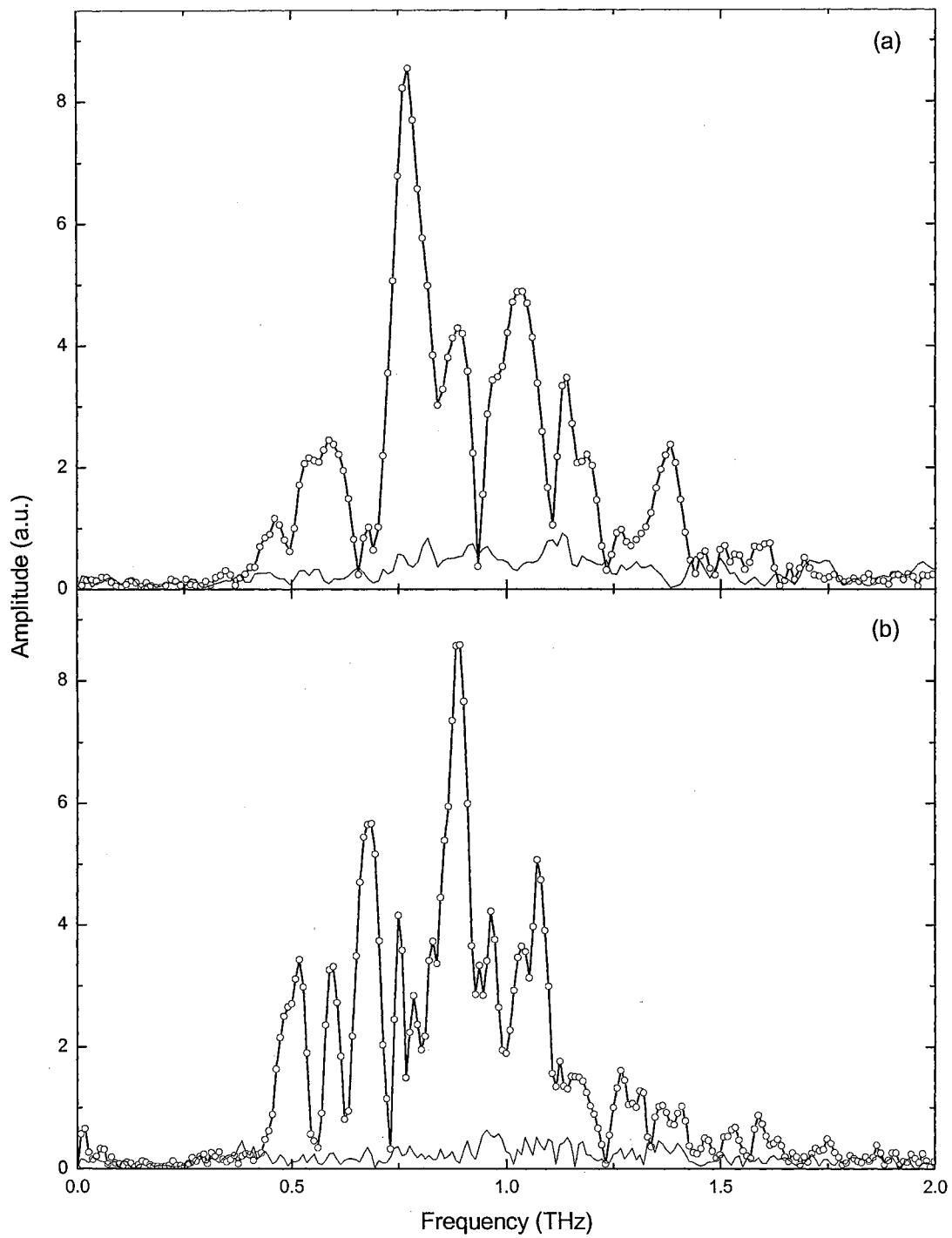


Fig 3-9 The spectra of (a) the first and (b) the second cavity pulses for coupling structure B. The solid lines on the bottom are the spectra of the reference

Again, the energy contained in the two cavity pulses can be compared From Fig. 3-9. If we take the square of the spectrum and then integrate over the frequency range from 0.0 THz to 2.0 THz, we obtain $E_1=10.00$ for the first cavity pulse and $E_2=9.53$ for the second cavity pulse. So for structure B, the two cavity pulses contain almost the same amount of energy, with the second pulse decaying about 4.7% compared with the first pulse. Remember for structure A, this decay is about 50%. In principle the two structures should give similar energy decay rate, this big difference is considered due to the alignment of the cylindrical cavity. As mentioned in Chapter II, due to the holder problem, the cylinder for structure A may not be well aligned, resulting in this huge decay of the cavity pulses. It should be emphasized that, this comparison does not give an accurate description of the cavity decay, as the coupling involves constructive and destructive interference among the WGM modes. In fact, at some frequencies, the second cavity pulse even has a larger intensity than the first one, due to the interference. An exact evaluation of the energy decay is therefore very difficult in this case.

The experimental results from the two coupling structures demonstrate the feasibility of the slab-cylinder structure as an effective coupling scheme for the THz WGM cavity. In the theoretical part, we will give the mode solutions for the slab waveguide and the cylindrical WGM modes, and the coupling between the two devices will be analyzed numerically. The mode solutions of the metal waveguide, the quasi-optical coupling between cylindrical lenses and the metal waveguide, and that between the metal waveguide and the slab waveguide will also be given as part of the theoretical analysis for this system.

CHAPTER IV

MODAL ANALYSIS

The propagation devices in our system include the metal plate waveguide, the dielectric slab waveguide, and the dielectric cylindrical cavity. Here we give the mode solutions for these devices, and their field profiles for selected frequencies.

4.1 Mode Solutions for the Metal Plate Waveguide

Fig. 4-1 shows the cross section and the coordinate system of a metal plate waveguide, with plate separation $2b$ and filling media of refractive index n_g . Since the incoming THz pulse is y -polarized, only the TM modes are coupled into the waveguide [37]. Assuming that the waveguide is infinite in x direction, and the conductivity of the metal plates is infinite, the normalized non-vanishing components of the TM modes are [41,42]

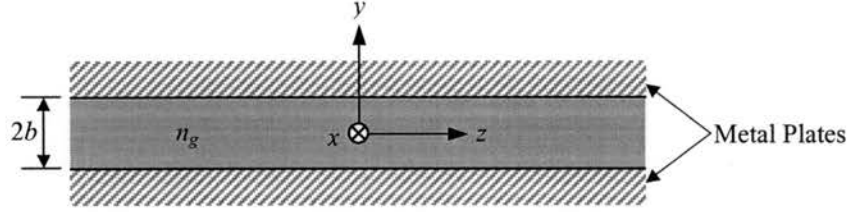


Fig. 4-1 Cross section and coordinate system of the metal plate waveguide.

$$\begin{aligned}
 h_{gm}^x(y) &= -\frac{1}{\sqrt{N_{gm}}} \frac{kn_g^2}{\beta_{gm}} \sqrt{\frac{\epsilon_0}{\mu_0}} \cos\left(\frac{m\pi y}{2b} + \frac{m\pi}{2}\right), \\
 e_{gm}^y(y) &= \frac{1}{\sqrt{N_{gm}}} \cos\left(\frac{m\pi y}{2b} + \frac{m\pi}{2}\right), \\
 e_{gm}^z(y) &= -\frac{1}{\sqrt{N_{gm}}} \frac{im\pi}{2b\beta_{gm}} \sin\left(\frac{m\pi y}{2b} + \frac{m\pi}{2}\right),
 \end{aligned} \tag{4-1}$$

where $m=0, 1, 2, \dots$ is the mode number and $|y| \leq b$. For simplicity, the phase factor $\exp(i\beta_{gm}z - i\omega t)$ has been omitted in the above solutions. Here the subscript g indicates metal waveguide; the superscripts x , y , and z indicate the corresponding components; $k=2\pi c/f$ is the free-space wavenumber, where c is the speed of light in free-space, and f is frequency; ϵ_0 and μ_0 are free-space permittivity and permeability, respectively.

Applying the boundary conditions, the mode propagation constant β_{gm} is found to be

$$\beta_{gm} = \sqrt{(n_g k)^2 - \left(\frac{m\pi}{2b}\right)^2}. \tag{4-2}$$

The mode is normalized in a way such that, the modal field carries unit power flow, when averaged by time, in the propagation direction. The normalization factor N_{gm} is then determined by [42]

$$\frac{1}{2} \int_{-b}^b \mathbf{e}_{gm} \times \mathbf{h}_{gm}^* \cdot \hat{z} = 1, \quad (4-3)$$

and is written explicitly as

$$N_{gm} = \begin{cases} \frac{bkn_g^2}{\beta_{gm}} \sqrt{\frac{\epsilon_0}{\mu_0}}, & m = 0; \\ \frac{bkn_g^2}{2\beta_{gm}} \sqrt{\frac{\epsilon_0}{\mu_0}}, & m > 0. \end{cases} \quad (4-4)$$

In Eq. (4-3), the factor 1/2 comes from the time averaging; the caret ^ indicates a unit vector; the asterisk * denotes complex conjugate. For later convenience we also give the orthogonality relation combined with the normalization relation (4-3) as (See Appendix A)

$$\frac{1}{2} \int_{-b}^b \mathbf{e}_{gm} \times \mathbf{h}_{gn}^* \cdot \hat{z} = \begin{cases} 0 & m \neq n; \\ 1 & m = n. \end{cases} \quad (4-5)$$

The cutoff frequency is given by [41]

$$f_{gm} = \frac{mc}{4bn_g}. \quad (4-6)$$

The fundamental mode, TM₀ mode, is in fact a TEM mode. It has no cutoff frequency and no group velocity dispersion, with both the phase velocity and the group velocity equal to the light speed in the filling material.

The normalized field profiles for the e_g^y field of the first three TM modes at 1.0 THz are presented in Fig. 4-2. Here the separation of the metal plates is 100 μm ($b = 50 \mu\text{m}$). It is worthy to point out that the field profile does not change with the filling media. Note that the even modes (TEM and TM₂) are symmetric but the odd mode (TM₁) is anti-

symmetric. When the incoming THz beam with symmetric Gaussian profile [36,37] is incident onto the metal waveguide, only the symmetric (even) modes are excited. Even though the higher order even mode is possible to be excited, it is still subject to the selection of the cutoff frequency, and the profile mapping (coupling coefficient) with the incoming beam.

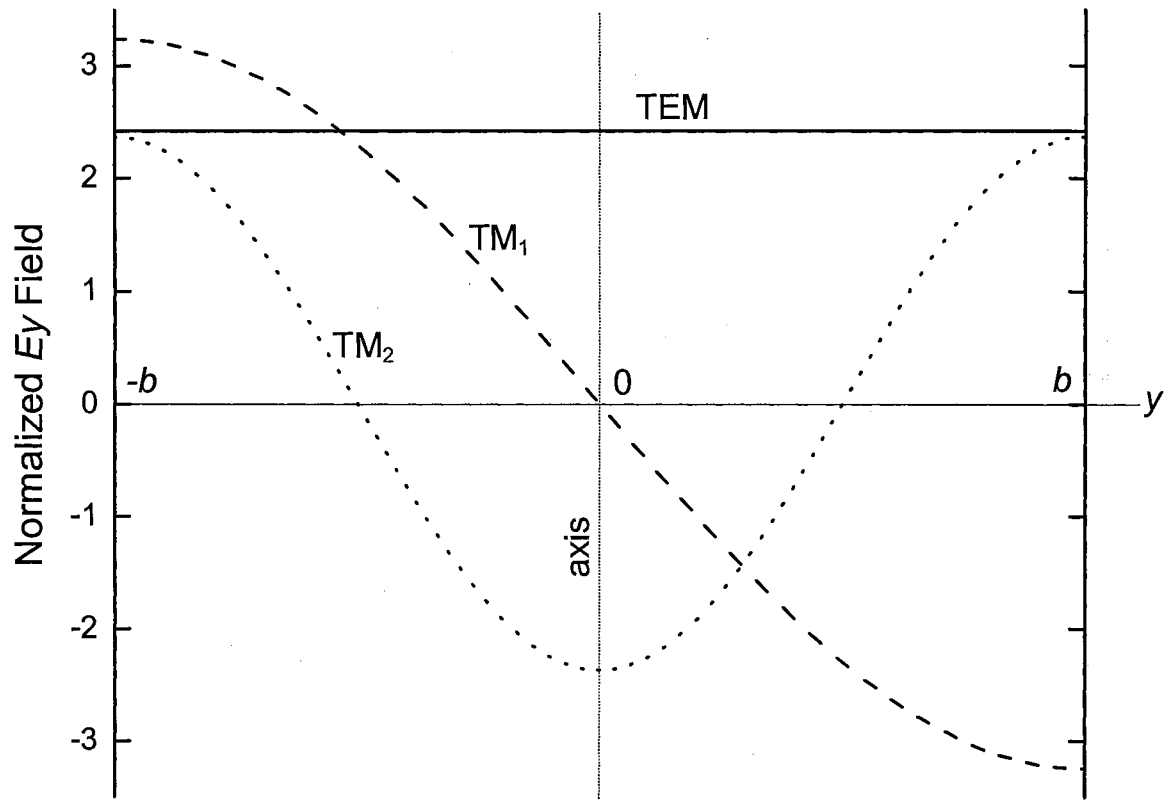


Fig. 4-2 Mode profiles of the first three TM modes for the metal waveguide.

4.2 Mode Solutions of TM Modes for Dielectric Slab Waveguide

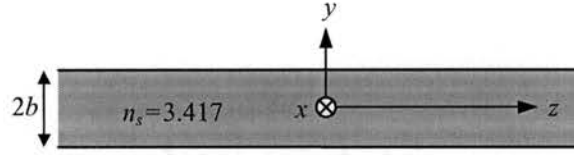


Fig. 4-3 Silicon slab waveguide.

Fig. 4-3 shows a slab waveguide with thickness $2b$ and refractive index n_s surrounded by air. Since the incoming THz beam (from the metal waveguide) is y -polarized, only TM modes ($E^x = 0, H^y = 0$) are coupled into the slab waveguide. Although the symmetric modes of the metal waveguide only couple into even TM modes of the slab waveguide, the odd TM modes are also possible to be excited when coupled with the cylinder. Here we give the field solutions for both the even and odd TM modes for the slab waveguide. Following Snyder and Love (Tables 12-1 and 12-2 of Ref. 42), for even TM modes, the non-vanishing field components are

Inside the waveguide, $|y| < b$,

$$\begin{aligned}
 h_{sm}^x(y) &= -\frac{1}{\sqrt{N_{sm}}} \frac{kn_s^2}{\beta_{sm}} \sqrt{\frac{\epsilon_0}{\mu_0}} \frac{\cos(U_m Y)}{\cos U_m}, \\
 e_{sm}^y(y) &= \frac{1}{\sqrt{N_{sm}}} \frac{\cos(U_m Y)}{\cos U_m}, \\
 e_{sm}^z(y) &= -\frac{1}{\sqrt{N_{sm}}} \frac{in_s^2}{b} \frac{W_m}{\beta_{sm}} \frac{\sin(U_m Y)}{\sin U_m}, \tag{4-7a}
 \end{aligned}$$

outside the waveguide, $|y| > b$,

$$\begin{aligned}
h_{sm}^x(y) &= -\frac{1}{\sqrt{N_{sm}}} \frac{kn_s^2}{\beta_{sm}} \sqrt{\frac{\epsilon_0}{\mu_0}} \frac{\exp(-W_m|Y|)}{\exp(-W_m)}, \\
e_{sm}^y(y) &= \frac{n_s^2}{\sqrt{N_{sm}}} \frac{\exp(-W_m|Y|)}{\exp(-W_m)}, \\
e_{sm}^z(y) &= -\frac{1}{\sqrt{N_{sm}}} \frac{in_s^2}{b} \frac{W_m}{\beta_{sm}} \frac{Y}{|Y|} \frac{\exp(-W_m|Y|)}{\exp(-W_m)}, \tag{4-7b}
\end{aligned}$$

where $m = 0, 2, \dots$ is the mode number, and the subscript s stands for slab. Again the phase factor $\exp(i\beta_{sm}z - i\omega t)$ has been omitted. Other parameters in the above equations are defined as

$$U_m = b\sqrt{k^2 n_s^2 - \beta_{sm}^2}, \quad W_m = b\sqrt{\beta_{sm}^2 - k^2}, \quad Y = y/b. \tag{4-8}$$

Similarly as in Eq. (4-5), the normalization and orthogonality relation is

$$\frac{1}{2} \int_{-\infty}^{\infty} \mathbf{e}_{sm} \times \mathbf{h}_{sn}^* \cdot \hat{z} dx = \begin{cases} 0 & m \neq n; \\ 1 & m = n. \end{cases} \tag{4-9}$$

The normalization factor is given explicitly as

$$N_{sm} = \frac{bkn_s^2}{2\beta_{sm}} \sqrt{\frac{\epsilon_0}{\mu_0}} \left\{ 1 + \frac{n_s^4 W_m^2}{U_m^2} + n_s^2 \frac{U_m^2 + W_m^2}{U_m^2 W_m} \right\}. \tag{4-10}$$

Applying the boundary conditions, with the help of Eq. (4-8), the propagation constant β_{sm} can be solved from the following eigenvalue equation

$$n_s^2 W_m = U_m \tan U_m. \tag{4-11}$$

On the other hand, for odd TM modes, the non-vanishing components of the fields are

Inside the waveguide, $|y| < b$,

$$h_{sm}^x(y) = -\frac{1}{\sqrt{N_{sm}}} \frac{kn_s^2}{\beta_m} \sqrt{\frac{\epsilon_0}{\mu_0}} \frac{\sin(U_m Y)}{\sin U_m},$$

$$e_{sm}^y(y) = \frac{1}{\sqrt{N_{sm}}} \frac{\sin(U_m Y)}{\sin U_m},$$

$$e_{sm}^z(y) = -\frac{1}{\sqrt{N_{sm}}} \frac{in_s^2 W_m \cos(U_m Y)}{b \beta_m \cos U_m}; \quad (4-12a)$$

outside the waveguide, $|y| > b$,

$$h_{sm}^x(y) = -\frac{1}{\sqrt{N_{sm}}} \frac{kn_s^2}{\beta_m} \sqrt{\frac{\epsilon_0}{\mu_0}} \frac{Y \exp(-W_m |Y|)}{|Y| \exp(-W_m)},$$

$$e_{sm}^y(y) = \frac{n_s^2}{\sqrt{N_{sm}}} \frac{Y \exp(-W_m |Y|)}{|Y| \exp(-W_m)},$$

$$e_{sm}^z(y) = -\frac{1}{\sqrt{N_{sm}}} \frac{in_s^2 W_m \exp(-W_m |Y|)}{b \beta_m \exp(-W_m)}; \quad (4-12b)$$

where $m = 1, 3, \dots$. The mode parameters and the normalization factor are defined the same as in Eqs. (4-8) and (4-10). Applying the boundary conditions, the eigenvalue equation for solving β_{sm} is given as

$$n_s^2 W_m = -U_m \cot U_m. \quad (4-13)$$

The cutoff frequency for the individual TM mode is given by [41,42]

$$f_{sm} = \frac{mc}{4b\sqrt{n_s^2 - 1}}, \quad (4-14)$$

where $m = 0, 1, 2, \dots$. Note that the fundamental TM_0 mode has a zero cutoff frequency.

There are infinite solutions (modes) to Eq. (4-11) and (4-13). The mode is numbered by m , which is the number of zeros inside the slab in the field pattern of its transverse components along y -direction, with TM_0 having no zero point and TM_1 having one. The

normalized field patterns of TM_0 , TM_1 and TM_2 modes at $f=0.75$ THz and $f=1.5$ THz for $2b=100 \mu\text{m}$ silicon slab waveguide are shown in Fig. 4-4, where the edges of the slab are indicated by dotted straight lines. According to Eq. (4-14), the cutoff frequencies for these modes are $f_{s0}=0$ THz, $f_{s1}=0.46$ THz, and $f_{s2}=0.92$ THz, respectively, so TM_2 mode

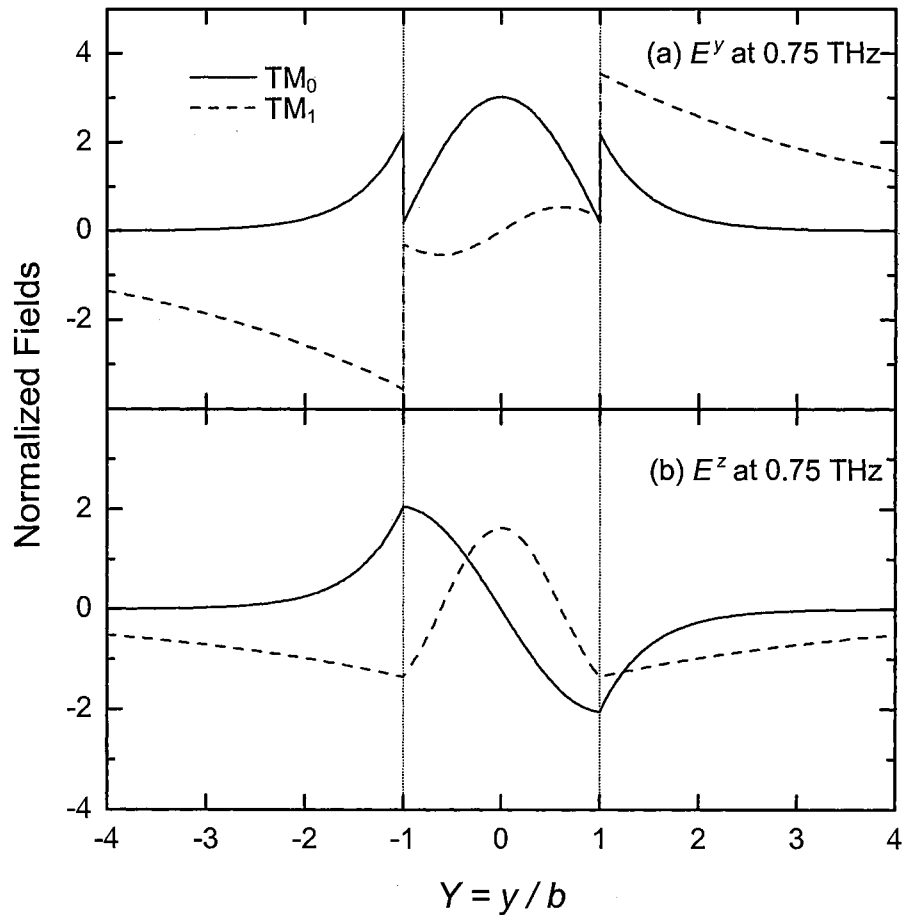


Fig. 4-4 Normalized field patterns of TM_0 , TM_1 and TM_2 modes for 0.1 mm silicon slab waveguide. (a) E^y at 0.75 THz; (b) E^z at 0.75 THz; (c) next page: E^y at 1.5 THz; (d) next page: E^z at 1.5 THz. Solid: TM_0 mode; Dashed: TM_1 mode; Dotted: TM_2 mode. The edges of the waveguide are indicated by the dotted lines. The cutoff frequency for TM_2 mode is above 0.75 TH, so TM_2 mode is not shown in (a) and (b).

is forbidden at 0.75 THz. Note that according to Eqs. (4-7a) and (4-7b), e_s^y and e_s^z have a phase difference of $\pi/2$. Fig. 4-4 only shows the real part of e_s^y and the imaginary part of e_s^z .

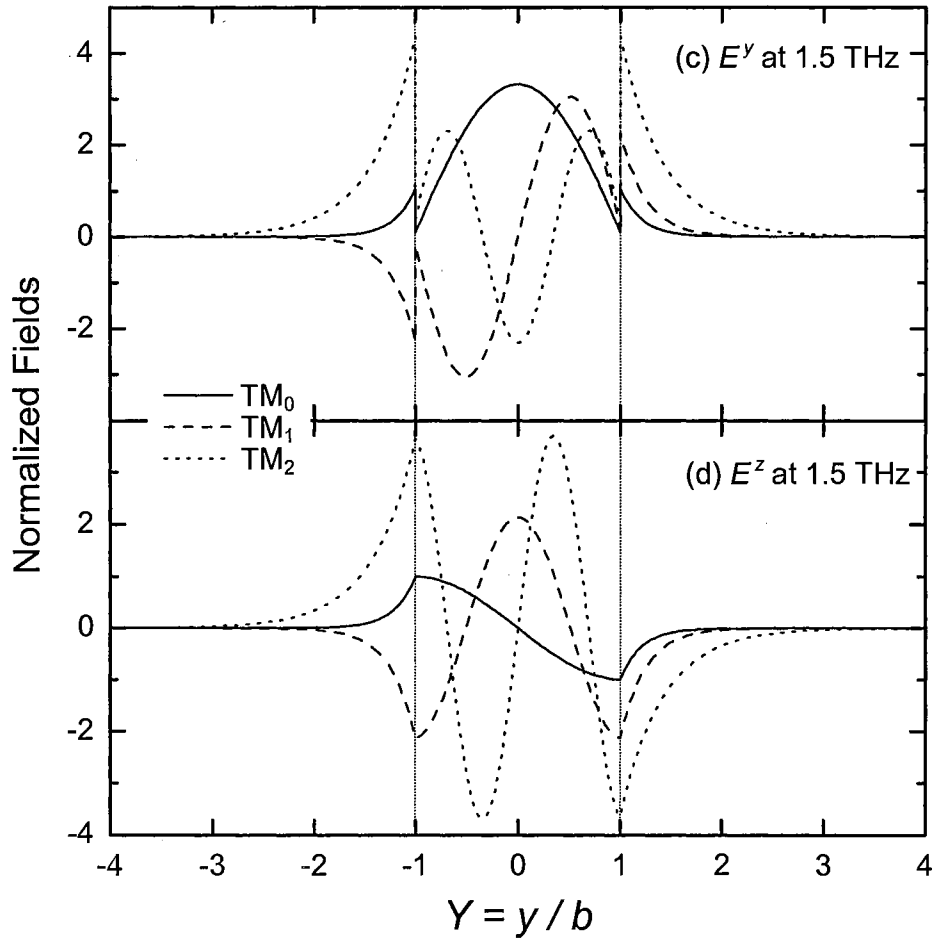


Fig. 4-4 Normalized field patterns of TM_0 , TM_1 and TM_2 modes for 0.1 mm silicon slab waveguide. (c) E^y at 1.5 THz; (d) E^z at 1.5 THz. Solid: TM_0 mode; Dashed: TM_1 mode; Dotted: TM_2 mode. The edges of the waveguide are indicated by the dotted lines.

4.3 Mode Solutions of Cylindrical WGM Modes

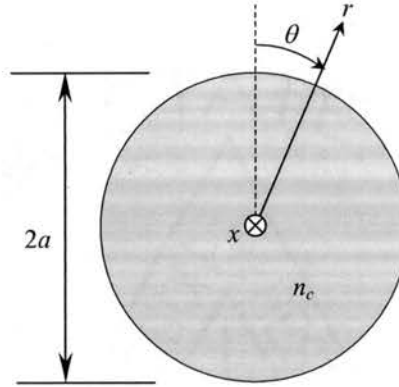


Fig. 4-5 Cross section of the dielectric cylinder and its coordinate system.

Fig. 4-5 shows the cross section of the cylinder of radius a with refractive index n_c surrounded by air. Again, only the modes with $E^x = 0$ and $H^\theta = 0$ are excited during the coupling process due to the polarization of the incoming THz pulse. In the literature, WGM modes with such a polarization are denoted as WGE modes [43,44], which means transverse electric (from the longitudinal direction) WGM modes. In our system, the propagation is along the θ direction, and the mode is transverse magnetic (from θ direction) since $H^\theta = 0$. However, to avoid this ambiguity, we will just use WG to denote the WGM modes in our coupling system.

In the coordinate system shown in Fig. 4-5, the non-vanishing components of the field solutions of the WG modes can be written as [45]

Inside the cylinder, ($r < a$)

$$\begin{aligned}
h_{cm}^x(r) &= \frac{1}{\sqrt{N_{cm}}} \sqrt{\frac{\epsilon_0}{\mu_0}} \frac{J_l(kn_c r)}{J_l(kn_c a)}, \\
e_{cm}^r(r) &= \frac{1}{\sqrt{N_{cm}}} \frac{l}{kn_c^2 r} \frac{J_l(kn_c r)}{J_l(kn_c a)}, \\
e_{cm}^\theta(r) &= \frac{1}{\sqrt{N_{cm}}} \frac{i}{n_c} \frac{[J_l(kn_c r)]'}{J_l(kn_c a)};
\end{aligned} \tag{4-15a}$$

Outside the cylinder, ($r > a$)

$$\begin{aligned}
h_{cm}^x &= \frac{1}{\sqrt{N_{cm}}} \sqrt{\frac{\epsilon_0}{\mu_0}} \frac{H_l^{(1)}(kr)}{H_l^{(1)}(ka)}, \\
e_{cm}^r &= \frac{1}{\sqrt{N_{cm}}} \frac{l}{kr} \frac{H_l^{(1)}(kr)}{H_l^{(1)}(ka)}, \\
e_{cm}^\theta &= \frac{i}{\sqrt{N_{cm}}} \frac{[H_l^{(1)}(kr)]'}{H_l^{(1)}(ka)};
\end{aligned} \tag{4-15b}$$

where the superscripts x , r , and θ indicate the corresponding components, J_l is the Bessel function of the first kind of order l , $H_l^{(1)}$ is the Hankel function of the first kind of order l , and the prime (') denotes the differentiation with respect to the argument inside the parentheses. Here l is essentially the angular propagation constant for the specific WG mode. Again, the phase factor $\exp(il\theta - i\omega t)$ has been omitted. The normalization factor N_{cm} is determined by

$$\frac{1}{2} \int_0^\infty \mathbf{e}_{cm} \times \mathbf{h}_{cm}^* \cdot \hat{\theta} dr = 1. \tag{4-16}$$

No analytical form is available for N_{cm} and it can only be evaluated numerically.

Applying the boundary conditions, we get the following eigenvalue equation,

$$\frac{[J_l(U_c)]'}{n_c J_l(U_c)} = \frac{[H_l^{(1)}(Q_c)]'}{H_l^{(1)}(Q_c)}, \quad (4-17a)$$

or equivalently,

$$\frac{J_{l+1}(U_c)}{kn_c a J_l(U_c)} - \frac{l}{U_c^2} = \frac{H_{l+1}^{(1)}(Q_c)}{ka H_l^{(1)}(Q_c)} - \frac{l}{Q_c^2}, \quad (4-17b)$$

where $U_c = kn_c a$ and $Q_c = ka$. The WGM modes are leaky modes in nature [42], so the eigenvalues U_c are complex. In our case, the imaginary part of U_c is very small and can be neglected, so the WGM modes are essentially bound modes.

Solving the eigenvalue equation (4-17), we obtain a set of solutions, with each solution corresponding to a WGM mode. A cylindrical WGM mode is usually indexed by three numbers: angular index l (the angular propagation constant), radial index m (the number of zeros of the transverse field component in radial direction, should always be an integer), and axial index h (the propagation constant in axial direction). In our case, we assume that the cylinder is longitudinally infinite, and there is no wave propagation along the axial direction, so we can set $h = 0$. In the case of cw coupling source, l should be an integer as required by the coherence condition, corresponding to a discrete set of resonant frequencies. In our case, since the coupling source is a subps THz pulse, the coherence condition is not required so l can be continuous, corresponding to a continuous frequency range which can be coupled into the cylinder. There are two ways to solve Eq. (4-17): (a) given l solve for the eigen-frequencies; (b) given frequency solve for l . Method (a) is usually used in the case of cw coupling source to calculate the resonant frequencies of a specific cavity resonator, where l is given as an integer as required by the coherence condition. In this case, one l corresponds to a discrete set of resonant frequencies, with

each numbered by the number of zeros in the field pattern in the radial direction. As an example, Fig. 4-6 shows the field patterns of the first five WG modes for a silicon cylinder with radius $a = 2.5$ mm. Here $l = 200$, and the radial number m and its corresponding resonant frequency for each mode are also indicated in the figure.

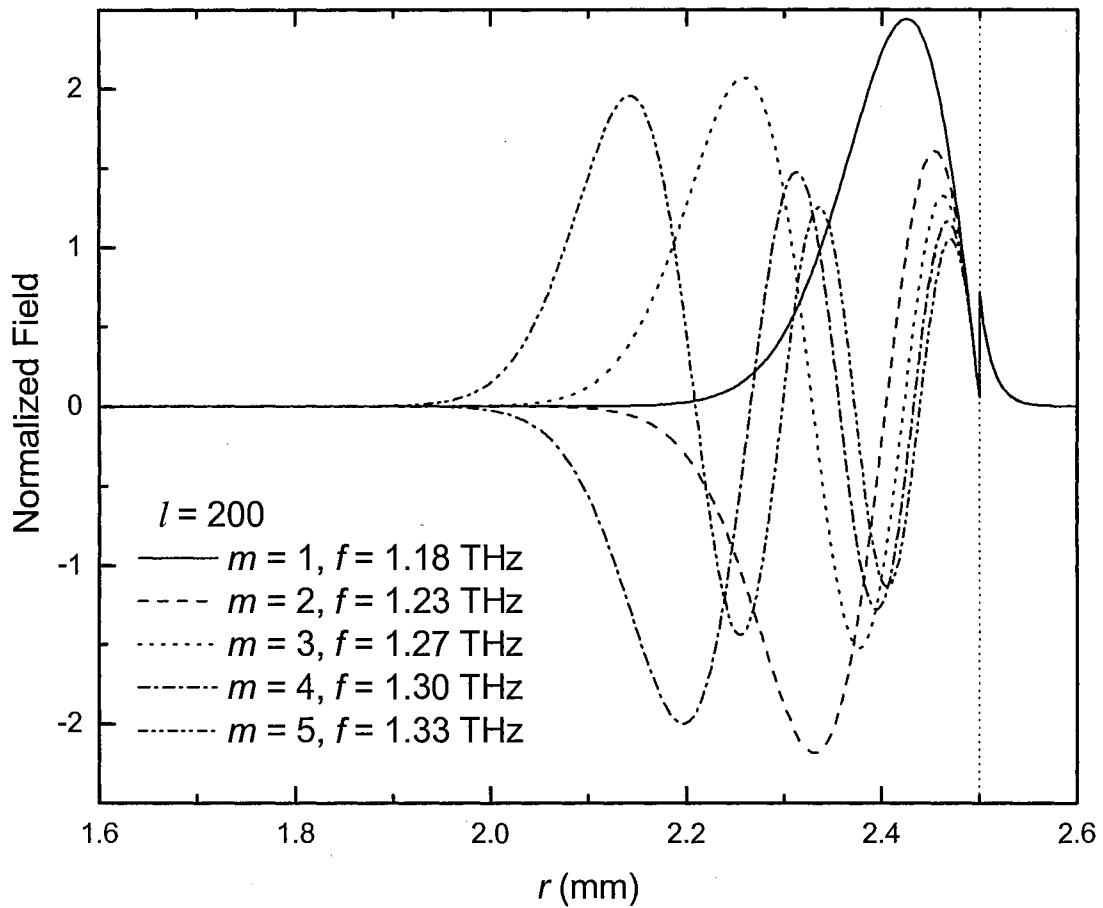


Fig. 4-6 E_z field profiles for WG modes of a silicon cylinder with radius $a = 2.5$ mm. Here $l = 200$ and the radial indexes $m = 1, 2, \dots, 5$. The corresponding frequencies are also given. The straight dotted line represents the rim of the cylinder.

For our case with subps THz pulses as coupling source, method (b) is used to solve Eq. (4-17). For each given frequency, a set of solutions for l is obtained and numbered the same way as in method (a). This method is in fact analogous to that in Sec. 4.2, where the frequency was given to solve for the propagation constant. Here the solutions of l are generally non-integers. Fig. 4-7 shows the normalized field profiles of e_c^r and e_c^θ components at 0.5 THz and 1.0 THz for a silicon cylinder with radius $a = 2.5$ mm. The figure shows the first five WG modes ($m = 1 \dots 5$) with their corresponding l values.

As discussed earlier, the cylindrical WGM modes are specified by three numbers l , m and h . For our case, the angular number l is a solution to the eigenvalue equation determined by the frequency and radial number m , and h is assumed to be 0, leaving m the only number to specify a mode. From now on, we will use WG_m to indicate the WG mode with radial number m , and its corresponding angular number will be written as l_m .

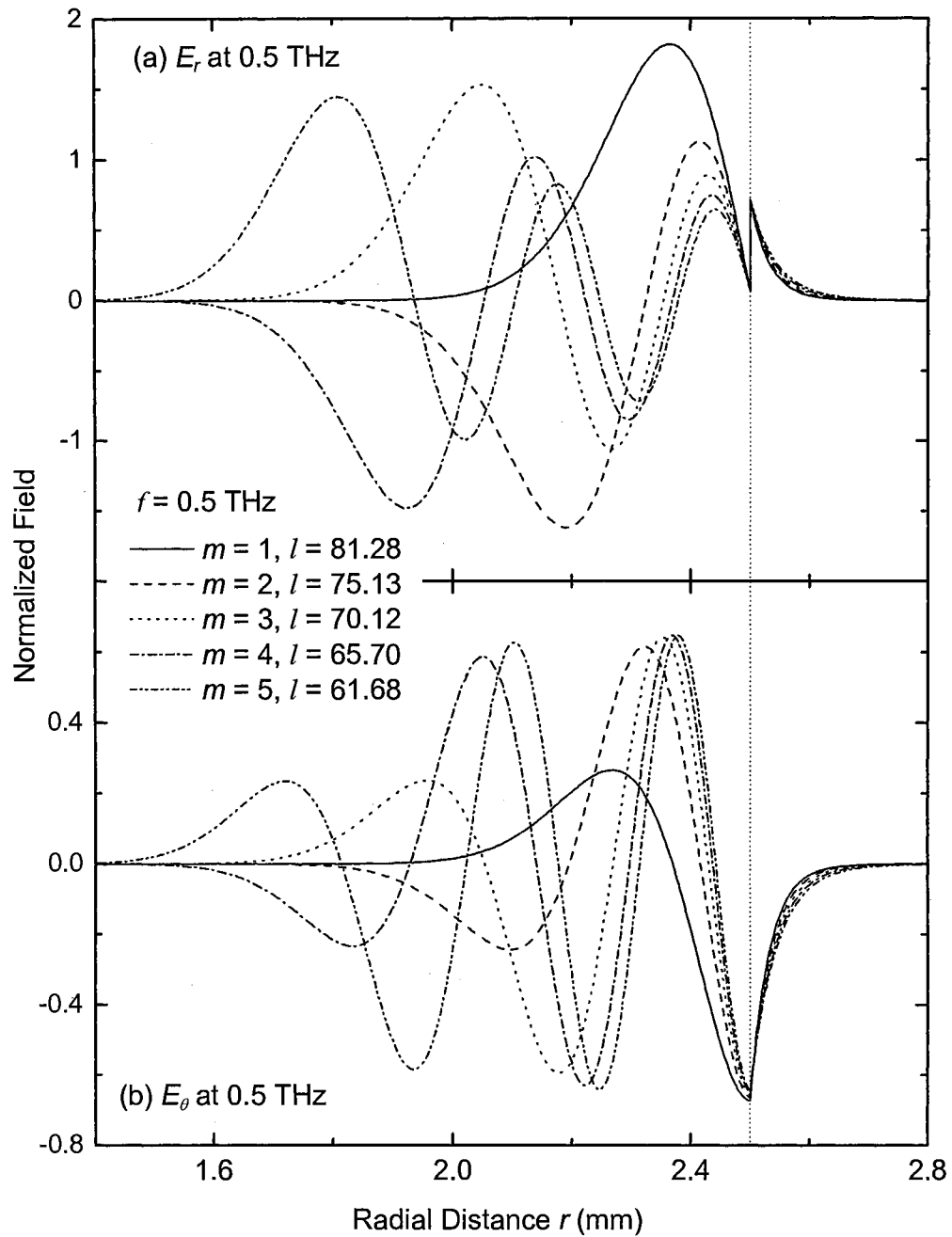


Fig. 4-7 Normalized field patterns for the first 5 WG modes for the 5-mm silicon cylinder. (a) E_r at 0.5 THz; (b) E_θ at 0.5 THz; (c) next page: E_r at 1.0 THz; (d) next page: E_θ at 1.0 THz. The straight dotted lines indicate the surface of the cylinder.

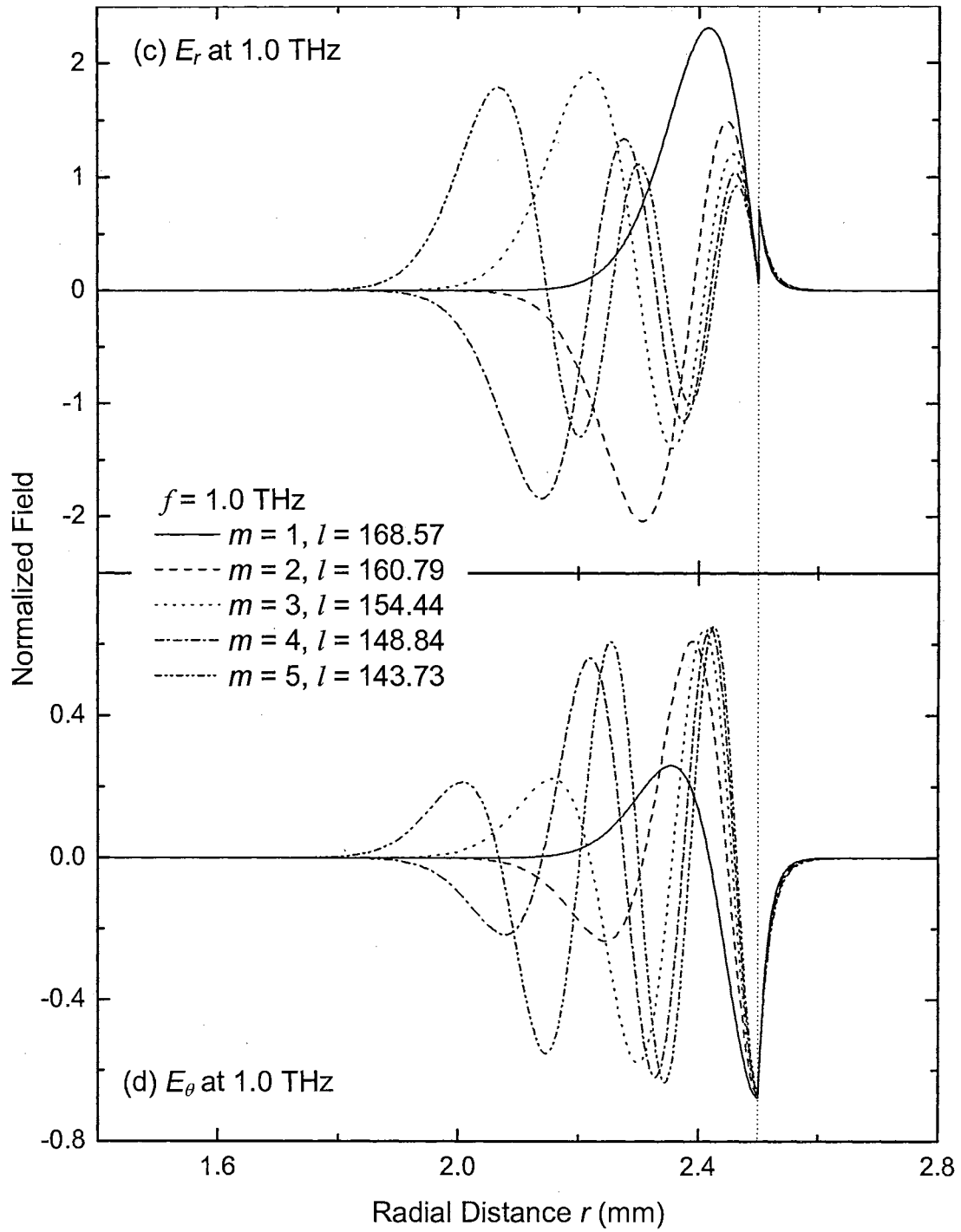


Fig. 4-7 Normalized field patterns for the first 5 WG modes for the 5-mm silicon cylinder. (c) E^r at 1.0 THz; (d) E^θ at 1.0 THz. The straight dotted lines indicate the surface of the cylinder.

CHAPTER V

COUPLED MODE THEORY

The coupled mode theory (CMT) is widely used in analyzing the coupling between coupled waveguide systems. In this theory, the variations of the modal amplitudes of the coupled waveguides with propagation distance are described by several differential equations, called coupled mode equations, which should be solved simultaneously in order to obtain the amplitude and phase change information of the coupled waveguide modes. The CMT dealing with the coupling between two parallel straight waveguides has been addressed in the literature [46-50]. It is worthy to point out that early derivations of CMT, such as those in [47,48], do not conserve energy during the coupling process. An exact formulation of CMT for parallel straight waveguides can be found in Ref. 49, where the author also gives the proof of power conservation during the coupling process.

For non-parallel waveguides, several modified forms of CMT are also available to analyze the coupling [51-53]. An exact formulation of CMT in these systems is difficult to obtain, and approximations have to be used in these derivations. For the coupling of

WGM resonators, the modified CMT is often used to analyze the coupling from the couplers to the WGM resonators [53,54]. In these analyses, the CMT for straight waveguide system were modified to calculate the coupling between a straight waveguide and the curved WGM resonator. We could also use the modified CMT to analyze the slab-cylinder coupling structure, however, we think that it is of theoretical interest to derive the CMT for the cylindrical coordinate system, and then modify this theory for the slab-cylinder structure.

Up to now, a complete derivation of CMT for the cylindrical coordinate is not available in the literature. In Ref. 53, the authors gave the derivation for the coupling between a dielectric ring and a dielectric disk, which can also be used for the coupling between concentric cylindrical systems. However, they used unnecessary approximation in the derivation, which made the final results questionable (See Appendix B). In this chapter, we will give the complete derivation of the CMT in the concentric cylindrical coordinate, and then modify this theory for the slab-cylinder structure.

5.1 Reciprocity Relation in Cylindrical Coordinates

Consider two sets of field solutions $(\mathbf{E}_1, \mathbf{H}_1, \mathbf{J}_1)$ and $(\mathbf{E}_2, \mathbf{H}_2, \mathbf{J}_2)$ in two different media with relative permittivities $\varepsilon_1(r, \theta)$ and $\varepsilon_2(r, \theta)$ which satisfy the Maxwell's equations and boundary conditions. Here \mathbf{E} , \mathbf{H} , and \mathbf{J} denote electrical field, magnetic field, and current

density, respectively. We assume an implicit time dependence $\exp(-i\omega t)$ in the field vectors and the current density. The relative permittivities are related with the refractive indexes by

$$\varepsilon_{1,2}(r, \theta) = n_{1,2}^2(r, \theta). \quad (5-1)$$

For simplicity we assume that the media are non-absorbing so ε_1 and ε_2 are all real, and the permeability is taken to have the free-space value μ_0 . The Maxwell's equations can be expressed in the form

$$\nabla \times \mathbf{E}_{1,2} = ik \sqrt{\frac{\mu_0}{\varepsilon_0}} \mathbf{H}_{1,2}, \quad (5-2a)$$

$$\nabla \times \mathbf{H}_{1,2} = \mathbf{J}_{1,2} - ik\varepsilon_{1,2} \sqrt{\frac{\varepsilon_0}{\mu_0}} \mathbf{E}_{1,2}. \quad (5-2b)$$

Here k , ε_0 , and μ_0 are wavenumber, permittivity, and permeability, respectively, all in free-space. From the vector equalities and Maxwell's equations, it is easy to obtain the following relation [42]

$$\nabla \cdot (\mathbf{E}_1 \times \mathbf{H}_2^* + \mathbf{E}_2^* \times \mathbf{H}_1) = ik \sqrt{\frac{\varepsilon_0}{\mu_0}} (\varepsilon_1 - \varepsilon_2) \mathbf{E}_1 \cdot \mathbf{E}_2^* - (\mathbf{E}_2^* \cdot \mathbf{J}_1 + \mathbf{E}_1 \cdot \mathbf{J}_2^*). \quad (5-3)$$

Here the asterisk * denotes complex conjugate. If we apply the above relation to an infinitesimal section $\Delta\theta$ of a cylindrical geometry which is invariant in the θ and y directions, we obtain the conjugate form of the reciprocity relation [42] in cylindrical coordinates (See Appendix B)

$$\begin{aligned} & \frac{\partial}{\partial \theta} \int_0^\infty (\mathbf{E}_1 \times \mathbf{H}_2^* + \mathbf{E}_2^* \times \mathbf{H}_1) \cdot \hat{\theta} dr \\ & = ik \sqrt{\frac{\varepsilon_0}{\mu_0}} \int_0^\infty (\varepsilon_1 - \varepsilon_2) r \mathbf{E}_1 \cdot \mathbf{E}_2^* dr - \int_0^\infty (\mathbf{E}_2^* \cdot \mathbf{J}_1 + \mathbf{E}_1 \cdot \mathbf{J}_2^*) r dr, \end{aligned} \quad (5-4)$$

where the caret $\hat{\cdot}$ indicates a unit vector. For completeness the unconjugated form of the reciprocity relation is also given here [42]

$$\begin{aligned} & \frac{\partial}{\partial \theta} \int_0^\infty (\mathbf{E}_1 \times \mathbf{H}_2 - \mathbf{E}_2 \times \mathbf{H}_1) \cdot \hat{\theta} \, dr \\ & = ik \sqrt{\frac{\varepsilon_0}{\mu_0}} \int_0^\infty (\varepsilon_2 - \varepsilon_1) r \mathbf{E}_1 \cdot \mathbf{E}_2 \, dr + \int_0^\infty (\mathbf{E}_2 \cdot \mathbf{J}_1 - \mathbf{E}_1 \cdot \mathbf{J}_2) r \, dr . \end{aligned} \quad (5-5)$$

The unconjugated form of the reciprocity relation for source-free system ($\mathbf{J}_1 = \mathbf{J}_2 = 0$) has been derived in Ref. 53. However, the authors used unnecessary approximation so the final form is different from (5-5). See Appendix B for details.

In general the current densities \mathbf{J}_1 and \mathbf{J}_2 do not appear in the coupling system. However, these quantities are useful in the physical understanding of the coupling, as will be seen in Appendix D.

5.2 Coupled Mode Equations in Cylindrical Coordinates

Now we apply the reciprocity relation (5-4) to the coupling between two hollow cylinders (hereafter called ring a and ring b) with their cross section shown in Fig. 5-1. The current densities \mathbf{J}_1 and \mathbf{J}_2 will be set to zero, as we will be dealing with a source-free coupling system. As shown in Fig. 5-2, we suppose the functions $\varepsilon_a(r, \theta)$ and $\varepsilon_b(r, \theta)$ represent the variation in the relative permittivities when only ring a and ring b are present, respectively, i.e.,

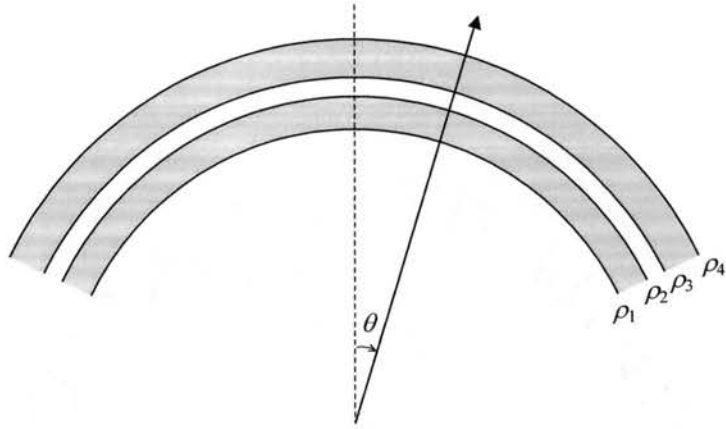


Fig. 5-1 Concentric rings coupling configuration.

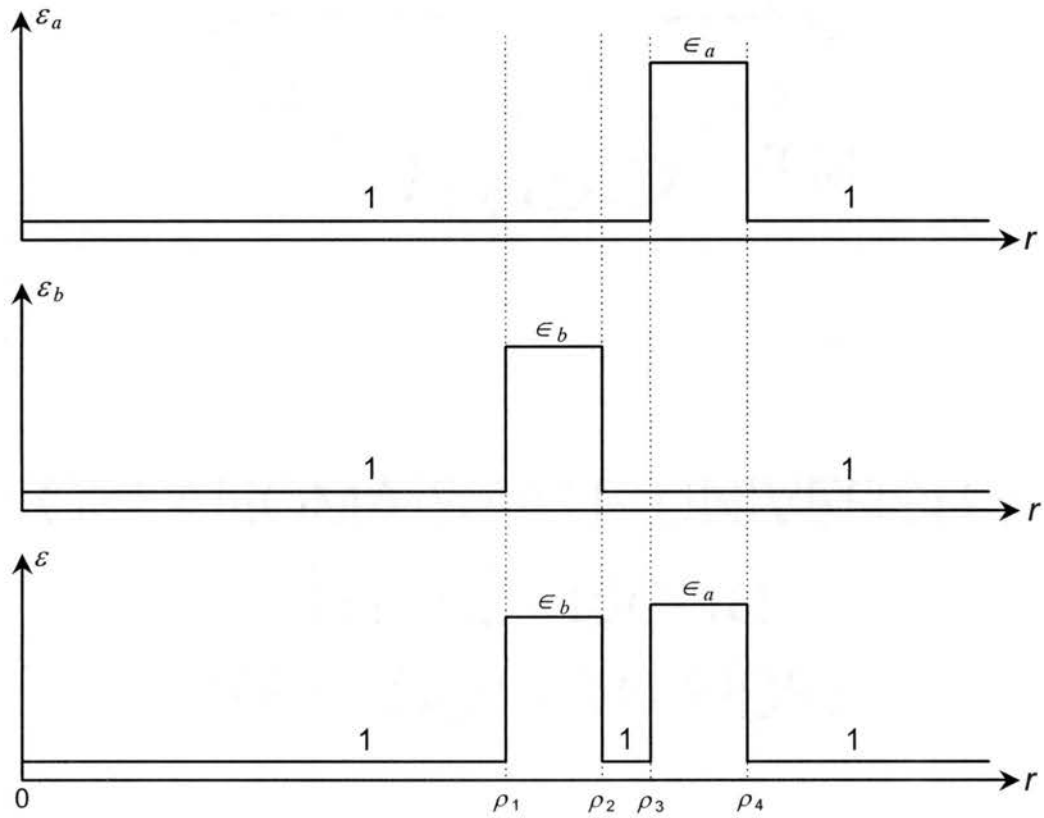


Fig. 5-2 Relative permittivities for the coupling configuration shown in Fig. 5-1.

$$\varepsilon_{a,b}(r,\theta) = \begin{cases} \varepsilon_{a,b}; & \text{within the rings} \\ \varepsilon_0; & \text{in the cladding} \end{cases} \quad (5-6)$$

where $\varepsilon_a(r,\theta) = \varepsilon_0$ (not ε_a) in the region ring b occupies and *vice versa*. The function $\varepsilon_T(r,\theta)$ represents the relative permittivity when both rings exist simultaneously. Following the general procedures of deriving coupled mode equations [42,49,53], we first give the modal fields for the isolated rings, and then form the total fields of the coupling system by modal expansion of the modal fields. The guided modes are

$$\begin{aligned} \mathbf{E}_{a,b}(r,\theta) &= \mathbf{E}'_{a,b}(r,\theta) + \hat{\theta}E_{a,b}^\theta(r,\theta) = \mathbf{e}_{a,b}(r,\theta)\exp(i\beta_{a,b}\theta) \\ &= [\mathbf{e}'_{a,b}(r,\theta) + \hat{\theta}e_{a,b}^\theta(r,\theta)]\exp(i\beta_{a,b}\theta), \end{aligned} \quad (5-7a)$$

$$\begin{aligned} \mathbf{H}_{a,b}(r,\theta) &= \mathbf{H}'_{a,b}(r,\theta) + \hat{\theta}H_{a,b}^\theta(r,\theta) = \mathbf{h}_{a,b}(r,\theta)\exp(i\beta_{a,b}\theta) \\ &= [\mathbf{h}'_{a,b}(r,\theta) + \hat{\theta}h_{a,b}^\theta(r,\theta)]\exp(i\beta_{a,b}\theta), \end{aligned} \quad (5-7b)$$

where the superscripts t and θ indicate the transverse and θ components, respectively, and the lower case \mathbf{e} (e) and \mathbf{h} (h) represent the normalized fields.

The total coupled fields ($\mathbf{E}_T, \mathbf{H}_T$) can be formed by modal expansions in terms of the two guided modes in rings a and b as follows [42,49,53]. For the transverse components,

$$\begin{aligned} \mathbf{E}'_T(r,\theta) &= a(\theta)\mathbf{E}'_a(r,\theta) + b(\theta)\mathbf{E}'_b(r,\theta) \\ &= a(\theta)\mathbf{e}'_a(r,\theta)\exp(i\beta_a\theta) + b(\theta)\mathbf{e}'_b(r,\theta)\exp(i\beta_b\theta), \end{aligned} \quad (5-8a)$$

$$\begin{aligned} \mathbf{H}'_T(r,\theta) &= a(\theta)\mathbf{H}'_a(r,\theta) + b(\theta)\mathbf{H}'_b(r,\theta) \\ &= a(\theta)\mathbf{h}'_a(r,\theta)\exp(i\beta_a\theta) + b(\theta)\mathbf{h}'_b(r,\theta)\exp(i\beta_b\theta), \end{aligned} \quad (5-8b)$$

where $a(\theta)$ and $b(\theta)$ are the modal amplitudes for the two modal fields. The longitudinal

components of the fields follow from Maxwell's equations in the cylindrical coordinates
(see Appendix C)

$$\begin{aligned}
E_T^\theta(r, \theta) &= a(\theta) \frac{\varepsilon_a}{\varepsilon_T} E_a^\theta(r) + b(\theta) \frac{\varepsilon_b}{\varepsilon_T} E_b^\theta(r) \\
&= a(\theta) \frac{\varepsilon_a}{\varepsilon_T} e_a^\theta(r, \theta) \exp(i\beta_a \theta) + b(\theta) \frac{\varepsilon_b}{\varepsilon_T} e_b^\theta(r, \theta) \exp(i\beta_b \theta), \quad (5-9a)
\end{aligned}$$

$$\begin{aligned}
H_T^\theta(r, \theta) &= a(\theta) H_a^\theta(r) + b(\theta) H_b^\theta(r) \\
&= a(\theta) h_a^\theta(r, \theta) \exp(i\beta_a \theta) + b(\theta) h_b^\theta(r, \theta) \exp(i\beta_b \theta). \quad (5-9b)
\end{aligned}$$

For the purpose of deriving coupled-mode equations, two sets of electromagnetic fields are necessary to use the reciprocity relation (5-4). We choose the total coupled fields shown in (5-8)-(5-9) as the first set of solutions. For the second set, we choose individual modal fields as shown in (5-7a) and (5-7b).

Case I: We choose

$$\varepsilon_1(r, \theta) = \varepsilon_T(r, \theta), \quad \varepsilon_2(r, \theta) = \varepsilon_a(r, \theta), \quad (5-10)$$

and

$$\begin{aligned}
\mathbf{E}_1(r, \theta) &= \mathbf{E}_T(r, \theta) = \mathbf{E}_T^t(r, \theta) + \hat{\theta} E_T^\theta(r, \theta), \\
\mathbf{H}_1(r, \theta) &= \mathbf{H}_T(r, \theta) = \mathbf{H}_T^t(r, \theta) + \hat{\theta} H_T^\theta(r, \theta), \\
\mathbf{E}_2(r, \theta) &= \mathbf{E}_a(r, \theta) = \mathbf{E}_a^t(r, \theta) + \hat{\theta} E_a^\theta(r, \theta), \\
\mathbf{H}_2(r, \theta) &= \mathbf{H}_a(r, \theta) = \mathbf{H}_a^t(r, \theta) + \hat{\theta} H_a^\theta(r, \theta). \quad (5-11)
\end{aligned}$$

We obtain from (5-4)

$$\frac{d}{d\theta}[M_{aa}a(\theta) + M_{ab}b(\theta)] = iC_{aa}a(\theta) + iC_{ab}b(\theta), \quad (5-12)$$

where M and C are coupling coefficients and will be defined later in (5-16a) and (5-16b).

Case II: We choose

$$\varepsilon_1(r, \theta) = \varepsilon_T(r, \theta), \quad \varepsilon_2(r, \theta) = \varepsilon_b(r, \theta), \quad (5-13)$$

and

$$\begin{aligned} \mathbf{E}_1(r, \theta) &= \mathbf{E}_T(r, \theta) = \mathbf{E}_T^t(r, \theta) + \hat{\theta}E_T^\theta(r, \theta), \\ \mathbf{H}_1(r, \theta) &= \mathbf{H}_T(r, \theta) = \mathbf{H}_T^t(r, \theta) + \hat{\theta}H_T^\theta(r, \theta), \\ \mathbf{E}_2(r, \theta) &= \mathbf{E}_b(r, \theta) = \mathbf{E}_b^t(r, \theta) + \hat{\theta}E_b^\theta(r, \theta), \\ \mathbf{H}_2(r, \theta) &= \mathbf{H}_b(r, \theta) = \mathbf{H}_b^t(r, \theta) + \hat{\theta}H_b^\theta(r, \theta). \end{aligned} \quad (5-14)$$

Again we obtain from (5-4)

$$\frac{d}{d\theta}[M_{ba}a(\theta) + M_{bb}b(\theta)] = iC_{ba}a(\theta) + iC_{bb}b(\theta). \quad (5-15)$$

The coupling coefficients in Eqs. (5-12) and (5-15) are defined as

$$M_{pq}(\theta) = \frac{1}{4} \int_0^\infty \exp(i\Delta\Phi_{pq}) [(\mathbf{e}_p^t)^* \times \mathbf{h}_q^t + \mathbf{e}_q^t \times (\mathbf{h}_p^t)^*] \cdot \hat{\theta} dr, \quad (5-16a)$$

$$C_{pq}(\theta) = \frac{k}{4} \sqrt{\frac{\varepsilon_0}{\mu_0}} \int_0^\infty \Delta\varepsilon_p \exp(i\Delta\Phi_{pq}) \left[\mathbf{e}_q^t \cdot (\mathbf{e}_p^t)^* + \frac{\varepsilon_q}{\varepsilon_T} e_q^\theta (e_p^\theta)^* \right] r dr, \quad (5-16b)$$

where

$$\Delta\varepsilon_p(r, \theta) = \varepsilon_T(r, \theta) - \varepsilon_p(r, \theta),$$

$$\Delta\Phi_{pq}(r, \theta) = \Phi_q(r, \theta) - \Phi_p(r, \theta) = \beta_q\theta - \beta_p\theta. \quad (5-17)$$

Note that by definition of the normalization factor (4-16)

$$M_{aa} = M_{bb} = 1. \quad (5-18)$$

Eqs. (5-12) and (5-15) are the coupled mode equations for the coupling between the rings a and b . A physical derivation of the coupled mode equations is shown in Appendix D.

In the derivation, we did not use any approximation, so the coupled mode equations (5-12) and (5-15) are exact for the concentric cylindrical waveguides. Here we deal with the coupling between two concentric rings, however, the same set of equations can also be used for the coupling between a ring and a cylinder, or other similar structures, as long as the coupled devices are concentric with circular symmetry.

5.3 Coupled Mode Equations for Slab-Cylinder System

Now we modify the coupled mode equations for our slab-cylinder coupling structure. As shown in Fig. 5-3, there exist relations between the cylindrical coordinate system of the cylinder and the Cartesian coordinate system of the slab

$$y = r \cos \theta - (a+b), \quad z = r \sin \theta. \quad (5-19)$$

We use the subscripts s and c to indicate slab and cylinder, respectively. The modal fields of the slab and cylinder are

$$\begin{aligned} \mathbf{E}_s(r, \theta) &= [\mathbf{e}_s^t(r, \theta) + \hat{\theta} e_s^\theta(r, \theta)] \exp(i\beta z), \\ \mathbf{H}_s(r, \theta) &= [\mathbf{h}_s^t(r, \theta) + \hat{\theta} h_s^\theta(r, \theta)] \exp(i\beta z), \\ \mathbf{E}_c(r, \theta) &= [\mathbf{e}_c^t(r, \theta) + \hat{\theta} e_c^\theta(r, \theta)] \exp(il\theta), \end{aligned} \quad (5-20a)$$

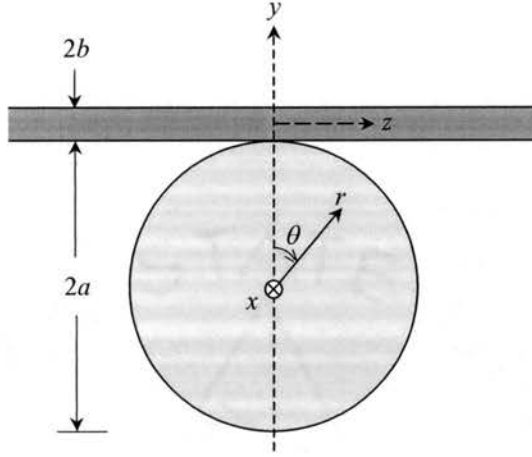


Fig. 5-3 Cross section and coordinate systems of the slab-cylinder coupling structure.

$$\mathbf{H}_c(r, \theta) = [\mathbf{h}'_c(r, \theta) + \hat{\theta} h_c^\theta(r, \theta)] \exp(il\theta), \quad (5-20b)$$

where β is the propagation constant of the slab mode, and l is the angular propagation constant for the WGM mode. In our case, the normalized fields of the slab TM mode and cylindrical WG mode can be expressed in the cylindrical coordinates as

$$\mathbf{e}'_s(r, \theta) = \hat{r} [e_s^y(y) \cos \theta + e_s^z(y) \sin \theta],$$

$$\mathbf{h}'_s(r, \theta) = \hat{x} h_s^x(y),$$

$$e_s^\theta(r, \theta) = e_s^z(y) \cos \theta - e_s^x(y) \sin \theta,$$

$$h_s^\theta(r, \theta) = 0; \quad (5-21a)$$

$$\mathbf{e}'_c(r, \theta) = \hat{r} e_c^r(r),$$

$$e_c^\theta(r, \theta) = e_c^\theta(r),$$

$$\mathbf{h}'_c(r, \theta) = \hat{x} h_c^x(r),$$

$$h_c^\theta(r, \theta) = 0. \quad (5-21b)$$

Similarly as in (5-8)-(5-9), we form the total fields as

$$\begin{aligned} \mathbf{E}_T(r, \theta) = a_s(z) \exp(i\beta z) & \left[\mathbf{E}'_s(r, \theta) + \frac{\varepsilon_s}{\varepsilon_T} E'_s(r, \theta) \hat{\theta} \right] \\ & + a_c(\theta) \exp(il\theta) \left[\mathbf{E}'_c(r) + \frac{\varepsilon_c}{\varepsilon_T} E'_c(r) \hat{\theta} \right], \end{aligned} \quad (5-22a)$$

$$\begin{aligned} \mathbf{H}_T(r, \theta) = a_s(z) \exp(i\beta z) & \left[\mathbf{H}'_s(r, \theta) + H'_s(r, \theta) \hat{\theta} \right] \\ & + a_c(\theta) \exp(il\theta) \left[\mathbf{H}'_c(r) + H'_c(r) \hat{\theta} \right]. \end{aligned} \quad (5-22b)$$

Note that the modal amplitude of slab $a_s(z)$ is a function of z instead of θ . For simplicity, we use $a_s(\theta)$ to approximate $a_s(z)$ where

$$z = (a + b) \sin \theta. \quad (5-23)$$

If we use this field for the first set of solution, and the individual modal fields shown in Eqs. (5-20a) and (5-20b) as the second set of solution, we obtain the same coupled mode equations as Eqs. (5-12) and (5-15). The coupling coefficients are still defined by Eqs. (5-16a) and (5-16b), except now $(p, q) = (s, c)$, $\Delta\Phi_{pq}(r, \theta) = \Phi_q(r, \theta) - \Phi_p(r, \theta)$, where $\Phi_s(r, \theta) = \beta_s(r, \theta)$, and $\Phi_c(r, \theta) = l\theta$. Similarly as in Eq. (5-18), we have

$$M_{ss} \approx M_{cc} = 1. \quad (5-24)$$

Eqs. (5-12) and (5-15) are the coupled mode equations for the coupling between a single slab mode and a single cylindrical WGM mode. Now if we have N modes (each mode may be either a slab mode or a cylinder mode) coupling together in the system, it is easy to derive the multimode coupling equations, with the m th one ($m = 1 \dots N$) written as

$$\frac{d}{d\theta} \sum_{n=1}^N M_{mn}(\theta) a_n(\theta) = i \sum_{n=1}^N C_{mn}(\theta) a_n(\theta), \quad (5-25)$$

where a_n is the modal amplitude of the n th mode, and M_{mn} and C_{mn} are coupling coefficients defined in Eqs. (5-16a) and (5-16b).

For our slab-cylinder system, the modes involved are: single slab TM_0 mode (with modal amplitude denoted by a_s), and the WG modes (with modal amplitudes denoted by a_1, a_2, \dots , for simplicity, hereafter we use numbers to indicate individual WG modes). Since the WG modes are orthogonal to each other, the coefficients $M_{mn} \approx 0$ and $C_{mn} \approx 0$ if m and n refer to different WG modes. This leaves the following coupled mode equation:

$$\frac{d}{d\theta}[M(\theta)A(\theta)] = iC(\theta)A(\theta), \quad (5-26)$$

where,

$$M(\theta) = \begin{pmatrix} M_{ss} & M_{s1} & M_{s2} & \cdots & M_{sN} \\ M_{1s} & M_{11} & M_{12} & \cdots & M_{1N} \\ M_{2s} & M_{21} & M_{22} & \cdots & M_{2N} \\ \vdots & \vdots & \vdots & \ddots & \vdots \\ M_{Ns} & M_{N1} & M_{N2} & \cdots & M_{NN} \end{pmatrix} = \begin{pmatrix} 1 & M_{s1} & M_{s2} & \cdots & M_{sN} \\ M_{1s} & 1 & 0 & \cdots & 0 \\ M_{2s} & 0 & 1 & \cdots & 0 \\ \vdots & \vdots & \vdots & \ddots & \vdots \\ M_{Ns} & 0 & 0 & \cdots & 1 \end{pmatrix},$$

$$C(\theta) = \begin{pmatrix} C_{ss} & C_{s1} & C_{s2} & \cdots & C_{sN} \\ C_{1s} & C_{11} & C_{12} & \cdots & C_{1N} \\ C_{2s} & C_{21} & C_{22} & \cdots & C_{2N} \\ \vdots & \vdots & \vdots & \ddots & \vdots \\ C_{Ns} & C_{N1} & C_{N2} & \cdots & C_{NN} \end{pmatrix} = \begin{pmatrix} C_{ss} & C_{s1} & C_{s2} & \cdots & C_{sN} \\ C_{1s} & C_{11} & 0 & \cdots & 0 \\ C_{2s} & 0 & C_{22} & \cdots & 0 \\ \vdots & \vdots & \vdots & \ddots & \vdots \\ C_{Ns} & 0 & 0 & \cdots & C_{NN} \end{pmatrix},$$

$$A(\theta) = \begin{pmatrix} a_s(\theta) \\ a_1(\theta) \\ a_2(\theta) \\ \vdots \\ a_N(\theta) \end{pmatrix}, \quad (5-27)$$

and N is the number of the coupled WG modes in the system.

If we consider the coupling between a single WG mode and the slab TM_0 and TM_1 modes, the coupling coefficient matrices will be

$$M(\theta) = \begin{pmatrix} 1 & 0 & M_{s_0c} \\ 0 & 1 & M_{s_1c} \\ M_{cs_0} & M_{cs_1} & 1 \end{pmatrix}, \quad C(\theta) = \begin{pmatrix} C_{s_0s_0} & 0 & C_{s_0c} \\ 0 & C_{s_1s_1} & C_{s_1c} \\ C_{cs_0} & C_{cs_1} & C_{cc} \end{pmatrix},$$

$$A(\theta) = \begin{pmatrix} a_{s_0}(\theta) \\ a_{s_1}(\theta) \\ a_c(\theta) \end{pmatrix}, \quad (5-28)$$

where the subscripts c , s_0 , and s_1 denote the WG mode, and the slab TM_0 and TM_1 modes, respectively.

CHAPTER VI

NUMERICAL RESULTS

6.1 Quasioptic Coupling

As stated in Chapter II, the THz beam is coupled into the metal plate waveguide by a plano-cylindrical lens. For the quasi-optic calculation of this coupling, we assume that the incoming THz beam propagates in the fundamental Gaussian mode, and the entrance side of the metal waveguide is located at the beam waist of the incident beam [36,37]. A quasioptic calculation of the coupling coefficient is shown in Appendix E. We now use Eqs. (E-13) and (E-14) to calculate the coupling between the modes in our system.

The y -polarized incoming Gaussian THz beam, with a waist of $200 \mu\text{m}$ [36], is incident onto the parallel metal plate waveguide with plate separation $2b = 100 \mu\text{m}$, and couples into its even TM modes [37]. For structure A, the THz pulse is first coupled into the air-filled metal guide. With a cutoff frequency of 3.0 THz for TM_2 mode, which is at the upper side of the spectral range of the system, the THz pulse couples into the single TEM mode of the air-filled metal plate waveguide. This pulse in turn couples into the same

TEM mode of the silicon-filled metal plate waveguide, so for structure A, the THz pulse propagates in the single TEM mode in the metal plate waveguide.

For structure B, the length of the air-filled part of the metal plate waveguide is very small (~ 0.25 mm), so we assume that the THz pulse directly couples into the silicon-filled metal plate waveguide. The amplitude coupling coefficient, a_p , is calculated for the TEM, TM_2 , and TM_4 modes of the silicon-filled metal waveguide, and the results are plotted in Fig. 6-1. The incoming Gaussian beam couples dominantly into the TEM

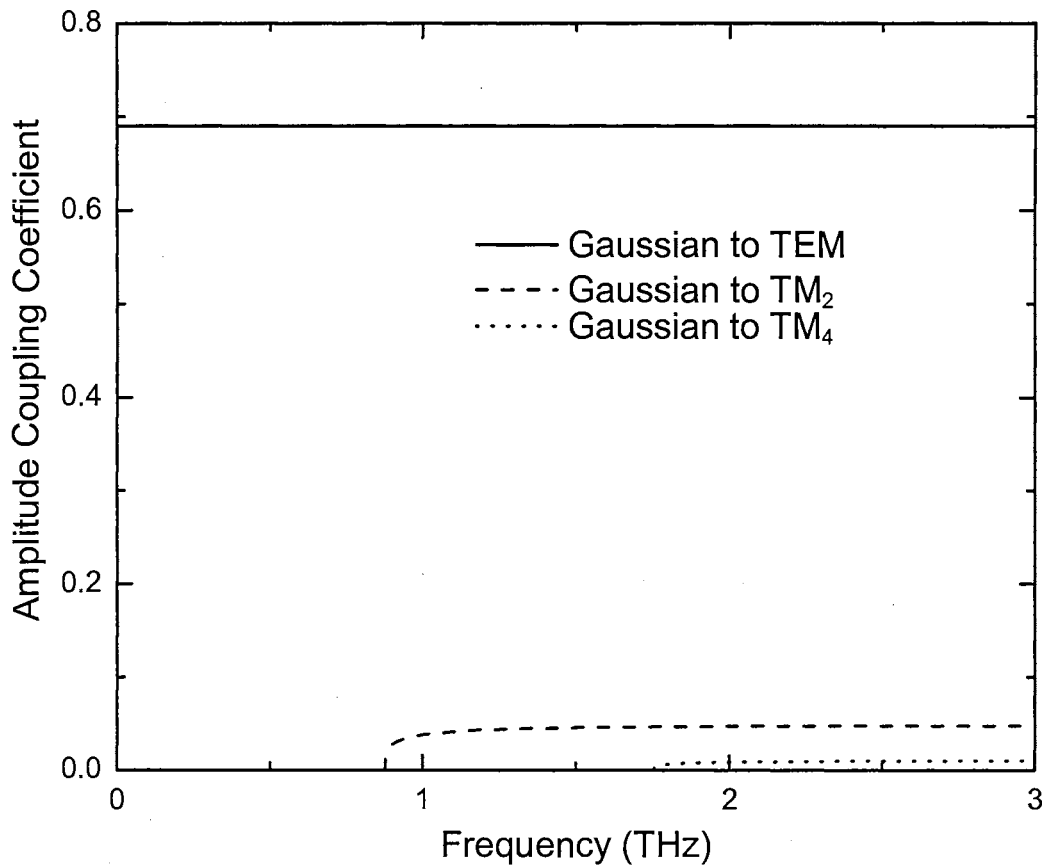


Fig. 6-1 Amplitude coupling coefficients for the coupling from Gaussian beam into the even TM modes of the silicon-filled metal plate waveguide.

mode of the metal guide; the other coupled modes, TM_2 and TM_4 , have amplitude coupling coefficients of approximately 7% and 1.5% of that for the TEM mode, respectively, showing the very good single-mode propagation property for the coupled THz pulse inside the metal plate waveguide.

The next coupling occurs at the interface of the metal plate guide and the dielectric slab guide. Again only the even TM modes of the slab guide are excited. Following the same procedure, we calculate the overall amplitude coupling coefficient for the coupling from the metal TEM mode into the slab TM_0 and TM_2 modes. The results are plotted in Fig. 6-2. To our surprise, it is in fact not a single-mode propagation for the THz pulse in the slab waveguide, as the TM_2 mode has an amplitude of approximately 30% of that for the dominant TM_0 mode above 1.5 THz. Nevertheless, the detected THz pulse shows good single-mode propagation property, as seen in Figs. 3-3 and 3-7. This is actually the combination results of the input and output couplings. The overall coupling coefficient, $|a_p|^2$, is also plotted in Fig. 6-2. Now the modal amplitude of TM_2 mode is less than 10% of that of the TM_0 mode, or less than 1% if comparing the energy carried by the two modes. In fact, the WGM THz pulses in our system cover a frequency range less than 1.5 THz, so the multimode feature of the THz pulse in the slab waveguide will not affect our analysis based on a single-mode propagation assumption in the slab waveguide.

As a conclusion to this section, here is the overall picture of the coupling and modes in our coupling structures without the cylinder in presence: the input Gaussian THz beam couples dominantly into the TEM mode of the metal plate waveguide; the TEM mode of

the metal guide couples into the TM_0 and TM_2 modes of the silicon slab waveguide. Even though the coupled TEM mode contains the contribution from the slab TM_2 mode, since this contribution is mainly above 1.5 THz, which is beyond the frequency range of our WGM THz pulses, we still view the detected main pulse as a single-mode pulse. This conclusion will be used to continue the analysis on the coupling system.

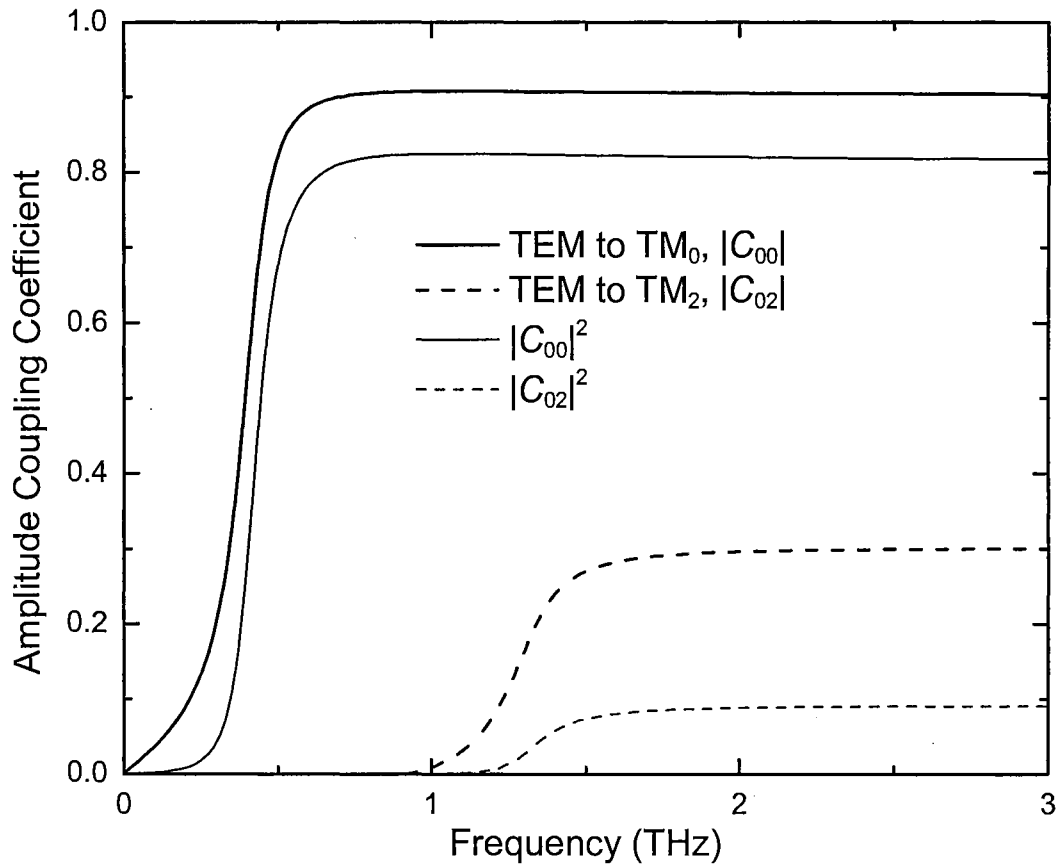


Fig. 6-2 Amplitude coupling coefficients for the coupling between the TEM mode of the silicon-filled metal guide and the TM_0 and TM_2 modes of the silicon slab waveguide.

6.2 Dispersion and Phase Match

In order to get a strong coupling, the phase velocity of the slab mode should be very close to that of the WGM mode in the coupling region [4-9], as required by the definition of coupling coefficients in Eqs. (5-16a) and (5-16b). For convenience, we define the effective refractive indexes

$$n_{sm}(f) = \frac{c}{v_{sm}(f)} = \frac{c\beta_m(f)}{2\pi f}, \quad (6-1)$$

for the slab modes, and

$$n_{cn}(f) = \frac{c}{v_{cn}(f)} = \frac{cl_n(f)}{2\pi af}, \quad (6-2)$$

for the WG modes [55], where the subscripts m and n indicate individual modes, and v_{sm} and v_{cn} are the phase velocities for an individual slab mode and cylindrical WG mode, respectively, and other parameters have the same meanings as in Chapter IV. In Eq. (6-2), we used the phase velocity at the rim of the cylinder to define the relative refractive index for the individual WG mode. Fig. 6-3 shows the effective refractive indexes for the slab TM_0 , TM_1 , and TM_2 modes, and the first 8 WG modes. It is seen from Fig. 6-3 that the TM_0 and TM_1 modes have a large frequency range of phase matching with the WG modes, while the TM_2 mode only matches the WG modes at the end of our experimental frequency range. We expect that at the vicinity of the intersection points the coupling will be strong between the corresponding modes, which means that we shall get a strong coupling between the WG modes and the TM_0 and TM_1 modes.

The slab TM_1 mode excited by the cylindrical WG modes will couple into the odd modes of the metal plate waveguide, but due to its anti-symmetric feature, it will not be detected by the THz receiver [34]. However, we will still need to evaluate its effect on the coupling between the WG modes and the TM_0 mode.

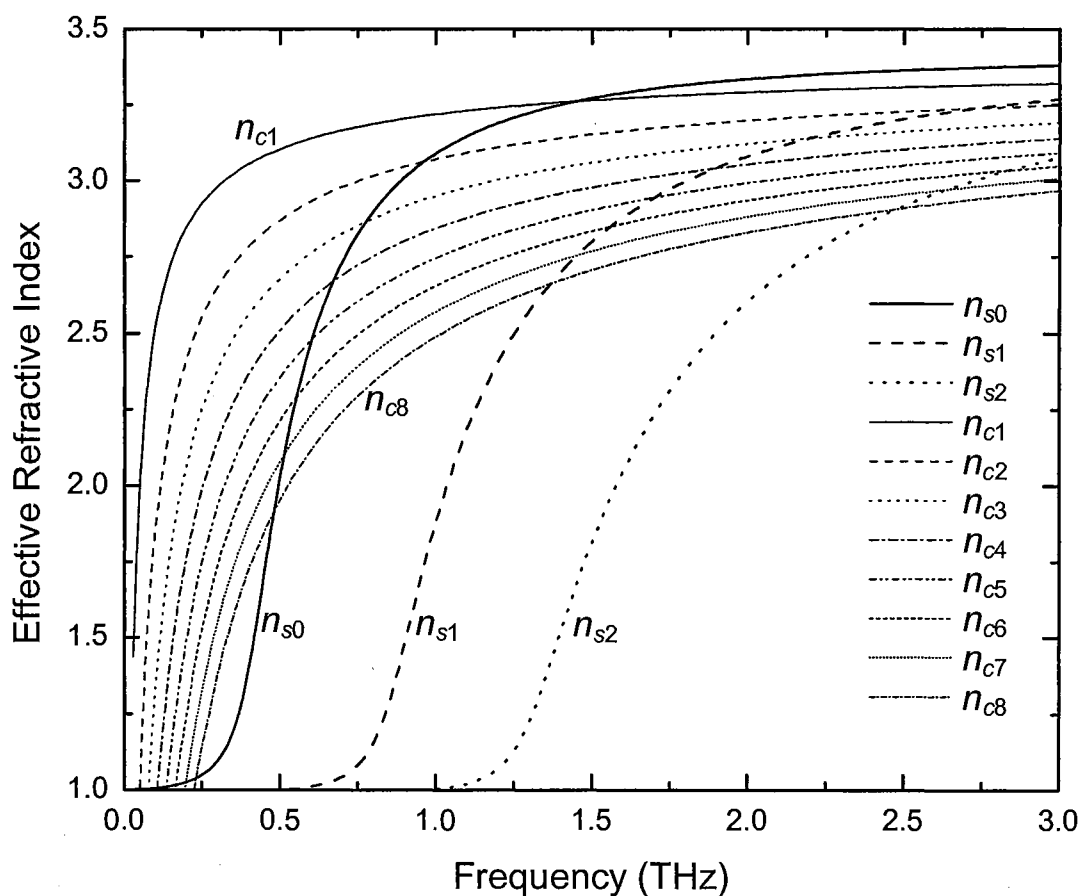


Fig. 6-3 Effective refractive indexes of the slab TM modes and the cylindrical WG modes.

6.3 Coupling Coefficients

Putting the integrals in Eqs. (5-16a) and (5-16b) into practice, we show in Figs. (6-4) and (6-5) the coupling coefficients C_{sc} and M_{sc} for WG_1 , WG_3 , WG_5 , and WG_7 modes when coupled with slab TM_0 and TM_1 modes, and at various frequencies. To keep the figures simple and easy to read, the results for the even modes WG_2 , WG_4 , WG_6 , WG_8 are not included in the plots. For convenience, the contents of the figures are listed here:

Fig. No.	Slab Mode	Coefficient	Frequency
Figs. 6-4a,b	TM_0	C_{sc}	0.6 THz
Figs. 6-4c,d	TM_0	M_{sc}	0.6 THz
Figs. 6-4e,f	TM_0	C_{sc}	1.0 THz
Figs. 6-4g,h	TM_0	M_{sc}	1.0 THz
Figs. 6-5a,b	TM_1	C_{sc}	1.0 THz
Figs. 6-5c,d	TM_1	M_{sc}	1.0 THz
Figs. 6-5e,f	TM_1	C_{sc}	1.5 THz
Figs. 6-5g,h	TM_1	M_{sc}	1.5 THz

Note that by definition, M_{sc} has a dimension of 1/angle. Unlike the concentric rings case, the slab-cylinder coupling structure gives the complex coupling coefficients varying with propagation length (here angle θ) except at the contact point ($\theta=0$) where all the parameters are real. All the coupling coefficients have their largest value at the contact point and decay with increasing angle. At lower frequencies, the evanescent portion of the guided field is larger, which results in the slower decay of the coupling coefficients with increasing angle, indicating a larger coupling range.

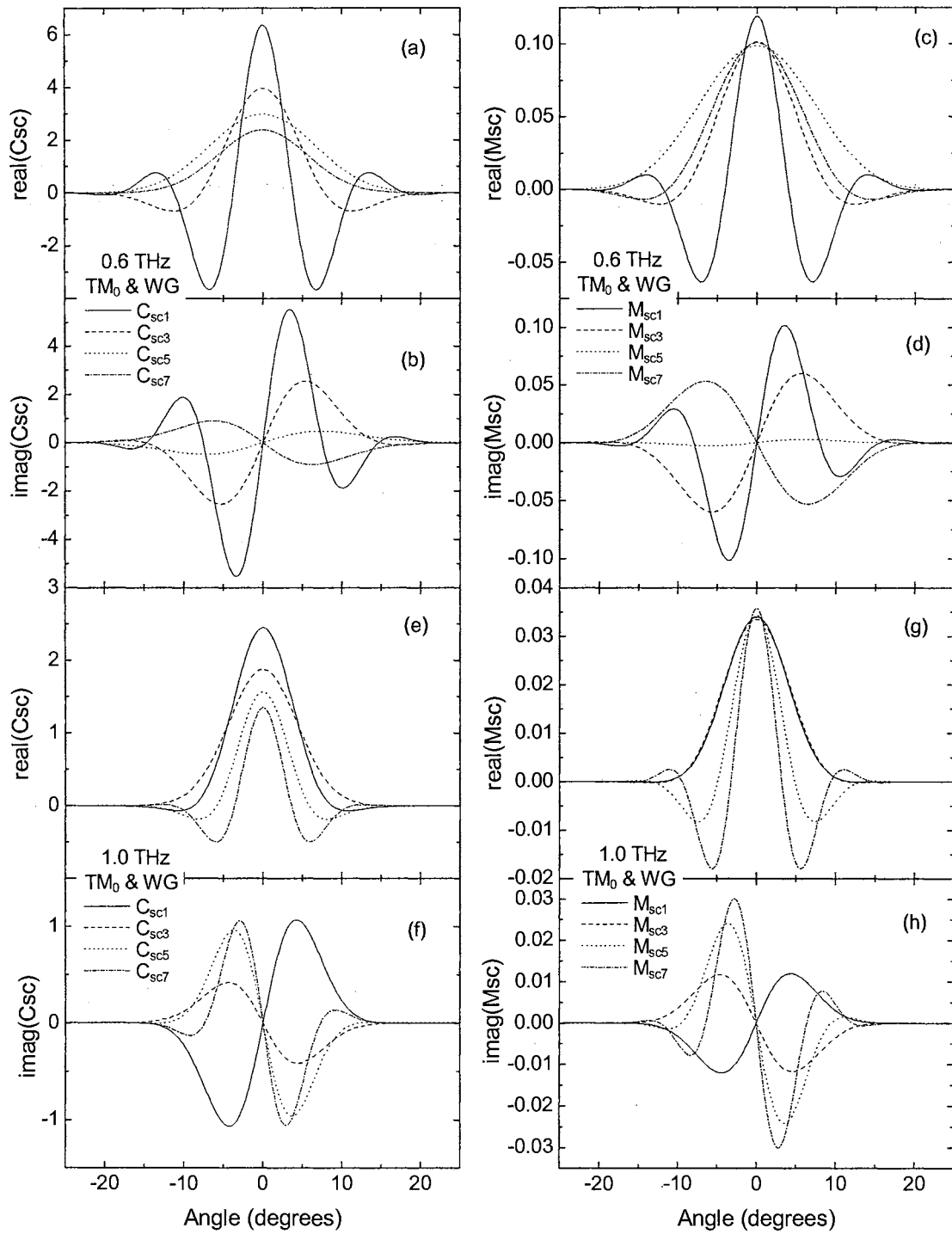


Fig. 6-4 Coupling coefficients for C_{sc} and M_{sc} for the slab TM_0 mode and WG_1 , WG_3 , WG_5 and WG_7 modes at 0.6 and 1.0 THz.

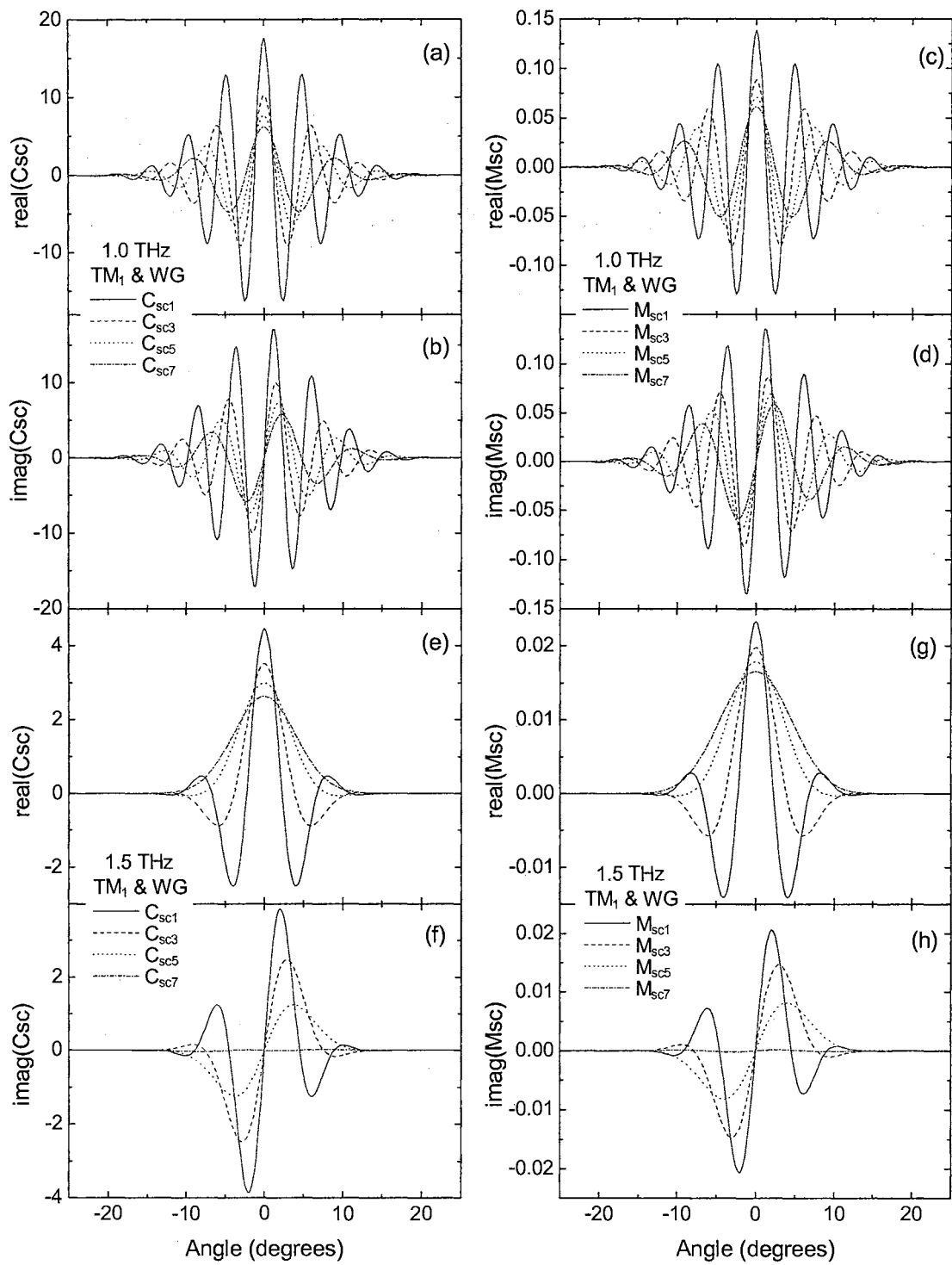


Fig. 6-5 Coupling coefficients for C_{sc} and M_{sc} for the slab TM_1 mode and WG_1 , WG_3 , WG_5 and WG_7 modes at 1.0 and 1.5 THz.

The oscillations in the coupling coefficients are related to the phase match condition between the specific slab mode and the WG mode (see Fig. 6-3). At 0.6 THz, WG₁ mode has the largest mismatch, while WG₅ has the closest phase velocity with TM₀ mode, therefore the coupling coefficients for WG₁ mode has the most oscillations, while those for the WG₅ mode do not show any oscillation feature (Figs. 6-4a,b,c,d). For TM₁ mode, the phase match condition is better satisfied at 1.5 THz, so the coupling coefficients show fewer oscillations (Figs. 6-5e,f,g,h) than those at 1.0 THz (Figs. 6-5a,b,c,d). The oscillations in the coupling coefficients are usually related with destructive interference, resulting in a small overall coupling result.

As mentioned in Appendix D, M_{sc} represents the projection of a WG mode to a slab mode, which is related to the overlap integral of the two modes. Since the slab and the cylinder are physically apart from each other, it is expected that this projection coefficient is far less than 1, which is true as shown in Figs. 6-4c,d,g,h, and Figs. 6-5c,d,g,h. In fact, in many early derivations of the coupled mode theory, M_{sc} was simply neglected [42, 46-48,51,52].

6.4 Coupling from Slab to Cylinder: Single Mode Coupling

As described earlier, the THz pulse propagates dominantly in the TM₀ mode in the slab waveguide. In the slab-cylinder contact area, this pulse couples into the cylinder as a

composition of the cylindrical WG modes. Though this coupling is simultaneously into several WG modes, for simplicity, we first analyze the coupling as a single mode case, i.e., we calculate the coupling from the dominant TM_0 mode into the individual WG mode separately. The coupling from the TM_2 mode is ignored in the calculation due to its large phase velocity discrepancies with the WG modes and therefore the small coupling.

The 4th order Runge-Kutta method [58] (see Appendix F) is used to numerically solve the coupled mode equations (5-12) and (5-15). In the calculation we set the initial modal amplitudes $a_{si}(\omega) = 1$ for the slab TM_0 mode, and $a_{mi}(\omega) = 0$ for the WG modes, where the subscript m is the WG mode index, and the subscript i indicates the initial value. We call this “slab excited” case as shown in Fig. 6-6a. Fig. 6-7 shows the absolute value of the modal amplitude evolution for the coupling from slab TM_0 mode to WG_1 , WG_3 , and WG_5 modes during the coupling process at 0.6 THz and 1.0 THz. Again to keep the figures simple and easy to read, results for the even WG modes are not included in the plots. It is clearly seen that most of the coupling occurs at the vicinity of the slab-cylinder contact point as the two fields have the greatest overlap in this region. For lower frequency, the coupling region is larger as the modal fields expand more in the cladding region and decay more slowly as the angle increases. The oscillations in the modal amplitude of WG mode correspond to the oscillations in the coupling coefficients (see Figs. 6-4e,f) owing to the phase mismatch between the two modes.

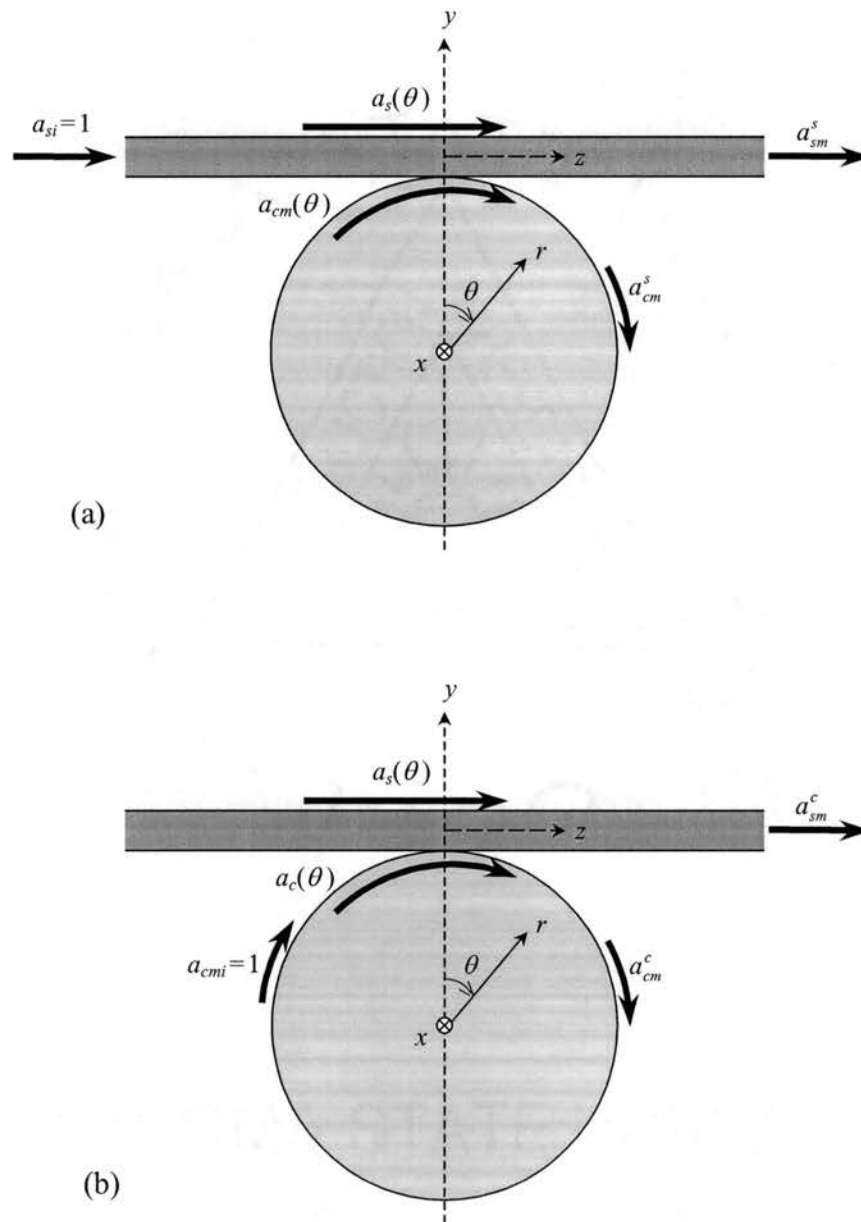


Fig. 6-6 Excitation and coupling diagram for the slab-cylinder coupling structure. (a) Slab excited case. (b) Cylinder excited case.

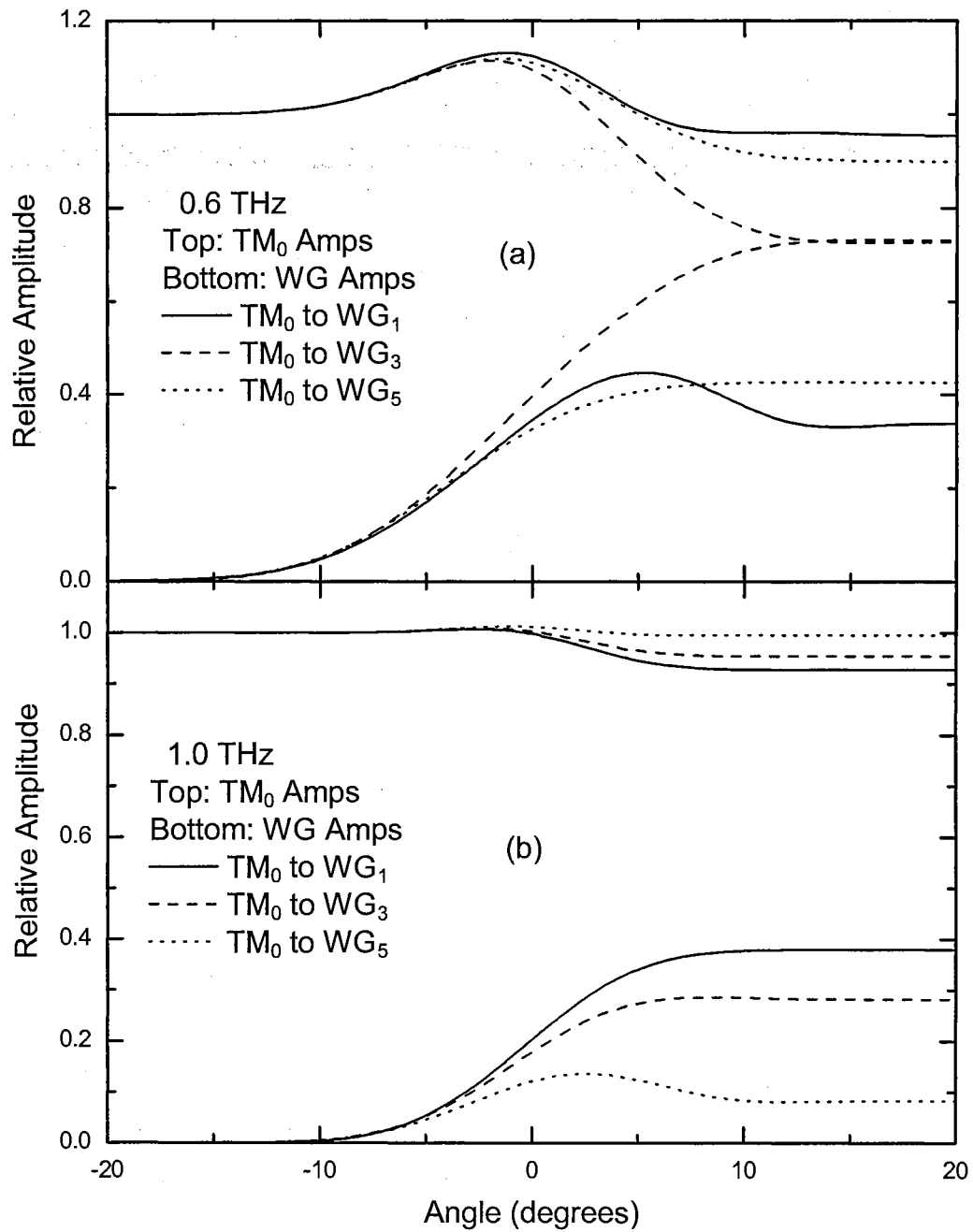


Fig. 6-7 Amplitude evolution of the coupling from TM_0 to WG_1 , WG_3 and WG_5 modes in the case of single mode coupling at (a) 0.6 THz and (b) 1.0 THz.

The above calculation is conducted over the frequency range from 0.3 THz–3.0 THz, and we obtain the complex frequency-dependent final coupled modal amplitudes $a_{sm}^s(\omega)$ and $a_{cm}^s(\omega)$, with their amplitude parts shown in Fig. 6-8 for the TM_0 mode and the WG_1 to WG_8 modes. Here the superscript s indicates “slab excited” case. As the index of the WG mode increases, the overall coupling spectrum profile goes to the lower frequency end, which is consistent with the phase matching result shown in Fig. 6-3. Below 0.4 THz, the coupling results show strange structures, which may be a result of the approximation (5-23) where we used an amplitude with θ -dependency to represent a modal amplitude with z -dependency. This is a good approximation at higher frequencies as the field is well confined inside the slab, and hence the coupling range is much smaller. At lower frequencies, as the evanescent portion of the field has more weight over the entire field pattern, this approximation tends to give larger error as the coupling range increase dramatically. Since the experimental spectra of the cavity pulses shown in Chapter III cover a frequency range above 0.4 THz, the overall calculation results will not be affected by the results at the lower frequency end.

In principle the power should be conserved during the coupling process. In the straight parallel waveguide coupling system, the total power evolution during the coupling process can be evaluated exactly and hence proved conserved [49]. However, in our system, an exact formulation of the power evolution is not readily available. We can calculate the total power after coupling as the summation of the square of the modal amplitudes, which should be equal to 1, the input power. Fig. 6-9 shows the total power after coupling for the single mode coupling from TM_0 to the first 8 WG modes. At above

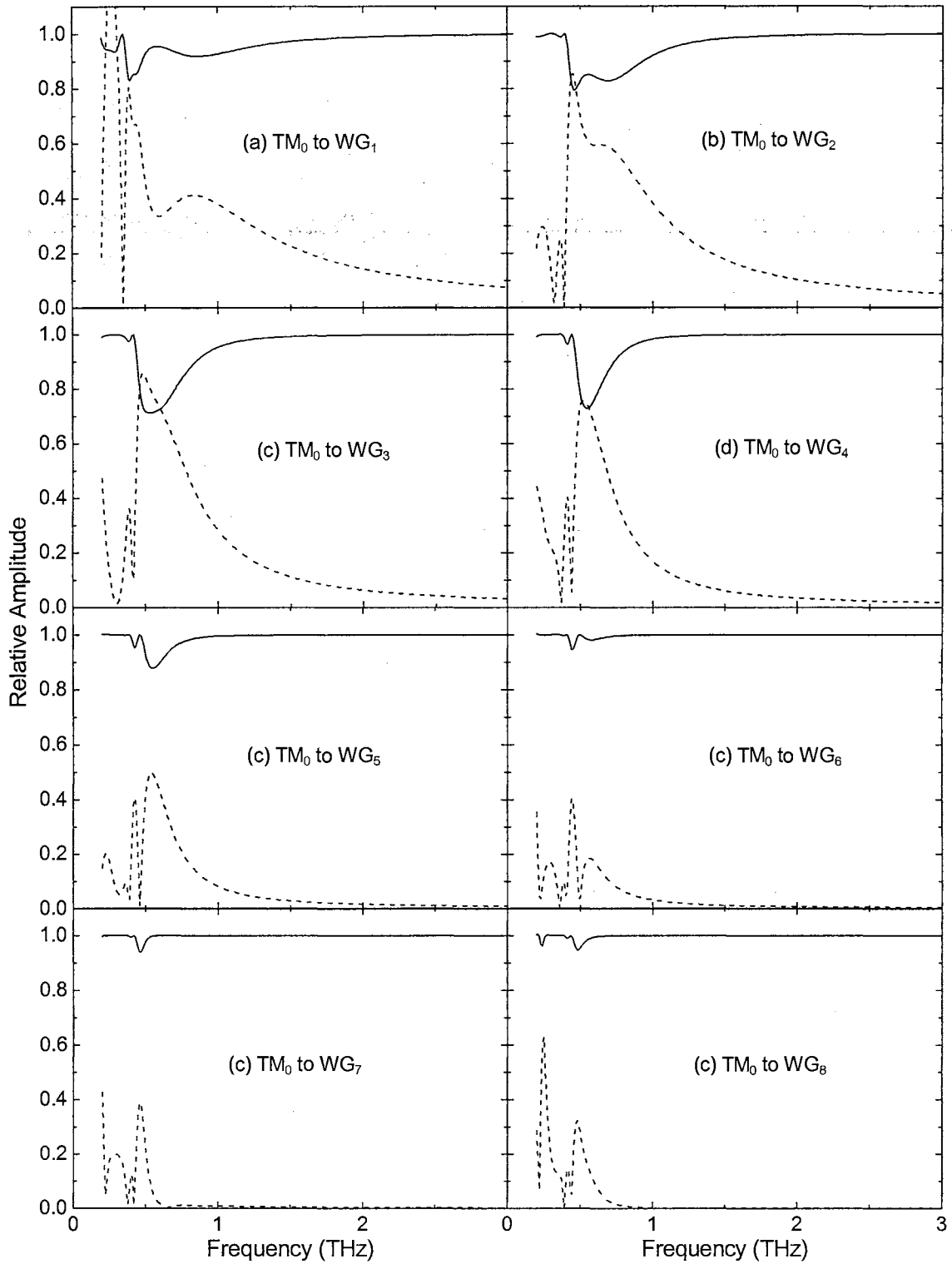


Fig. 6-8 Single mode coupling results for the coupling from TM_0 to first 8 WG modes. Solid: TM_0 amplitudes; Dashed: WG amplitudes.

0.6 THz, the calculated total power is within 5% of the power conservation level. However, at lower frequencies, the calculated total power is well off from the input power, which is 1, indicating a bad accuracy of the calculation at lower frequencies.

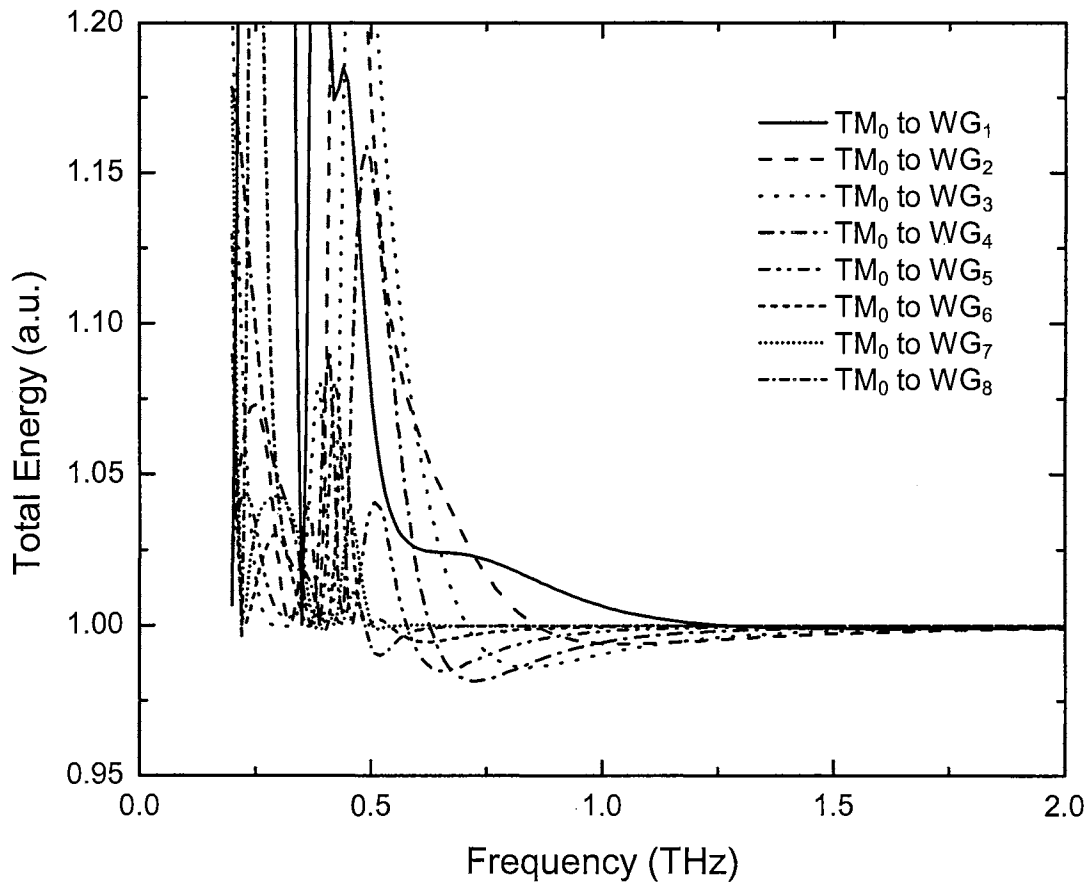


Fig. 6-9 Total power after coupling for the single mode coupling from TM_0 to the first 8 WG modes.

6.5 Coupling from Cylinder to Slab and the Effect of TM_1 Mode

The coupled WGM THz pulse will propagate around the cylinder continuously. When this pulse arrives at the slab-cylinder contact region, the coupling from the cylinder to the slab occurs. For simplicity, we first assume that only a single TM_0 mode is excited inside the slab by the WG modes. Again the 4th order Runge-Kutta method is used to solve the coupled mode equations (5-12) and (5-15). In the calculation we set the initial modal amplitudes $a_{sl}(\omega) = 0$ for the slab TM_0 mode, and $a_{mi}(\omega) = 1$ for the WG modes, as shown in Fig. 6-6b. We call this “cylinder excited” case. We obtain the complex final coupled modal amplitudes $a_{sm}^c(\omega)$ and $a_{cm}^c(\omega)$, and show their amplitude parts in Fig. 6-10 for the TM_0 mode and the first 8 WG modes, for the frequency range from 0.3 THz–3.0 THz. Here the superscript c indicates “cylinder excited” case. Again the overall coupling spectrum profile moves to the lower frequency end as the index of the WG mode increases.

In a similar way the total power after coupling is calculated for the coupling from individual WG modes into the slab TM_0 mode. The results are shown in Fig. 6-11. Again the calculation gives good power conservation at high frequencies, and the theory seems invalid at lower frequencies.

Although the TM_1 mode is not excited in the slab waveguide by the preceding metal plate guide, it is possible to be excited during the coupling between the slab and the cylinder. This coupling is neglected in the calculation of the coupling in the slab excited case in the

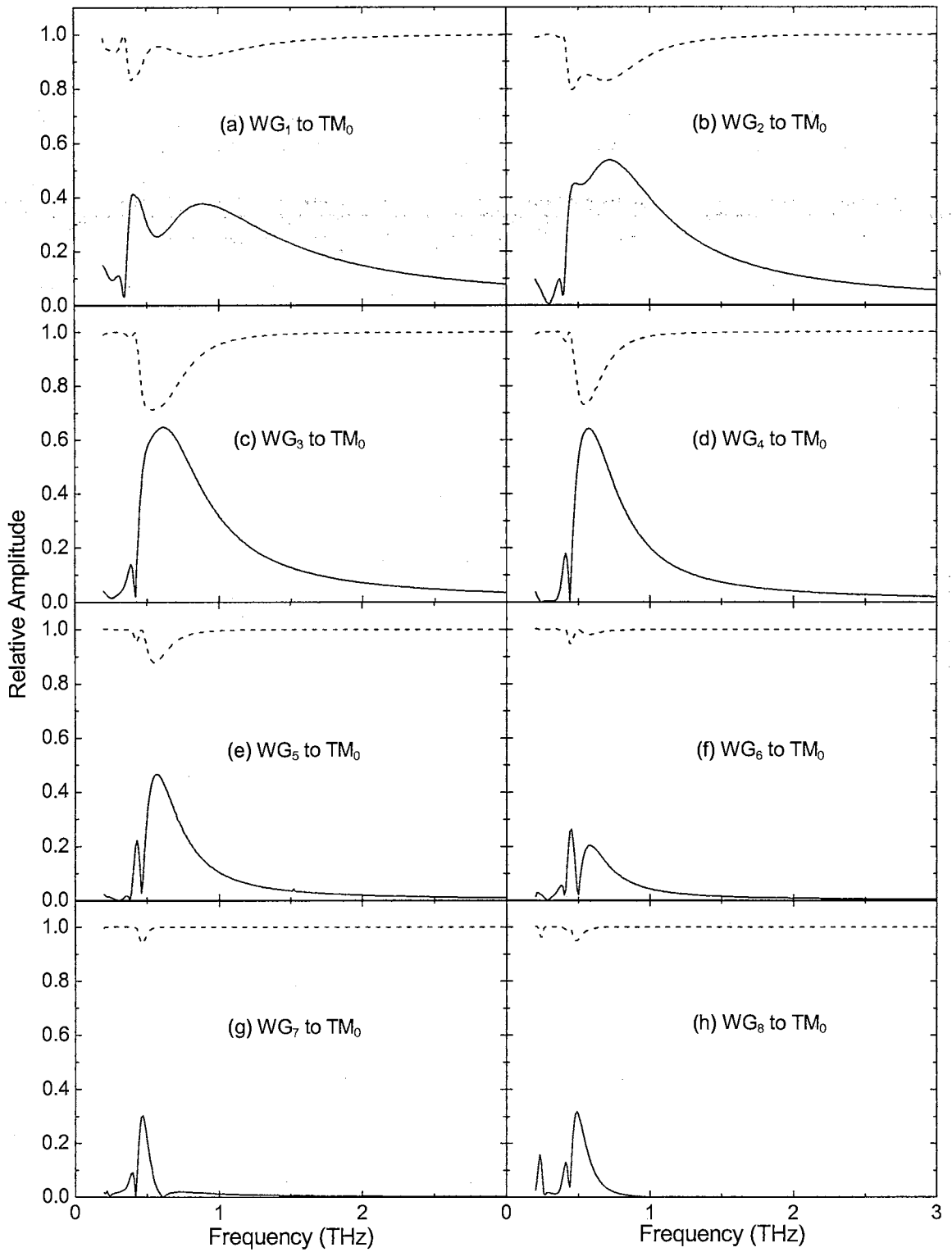


Fig. 6-10 Single mode coupling results for the coupling from first 8 WG modes to TM_0 mode. Solid: TM_0 amplitudes; Dashed: WG amplitudes.

previous section, since the TM_1 can only be excited by the WG modes and therefore this coupling is a second order effect. However, in the cylinder excited case, the TM_0 and TM_1 modes are excited simultaneously by the WG modes, if possible, and the coupling into the TM_1 mode may affect the coupling result into the TM_0 mode. Figs. 6-12 and 6-13 show the amplitude evolution and phase change of the modes during the coupling process when only TM_0 mode is considered, at 1.0 THz and 1.5 THz, respectively. For comparison, we plot in Figs. 6-14 and 6-15 the results when both TM_0 and TM_1 are considered for 1.0 THz and 1.5 THz, respectively. The phase change for the TM_1 mode

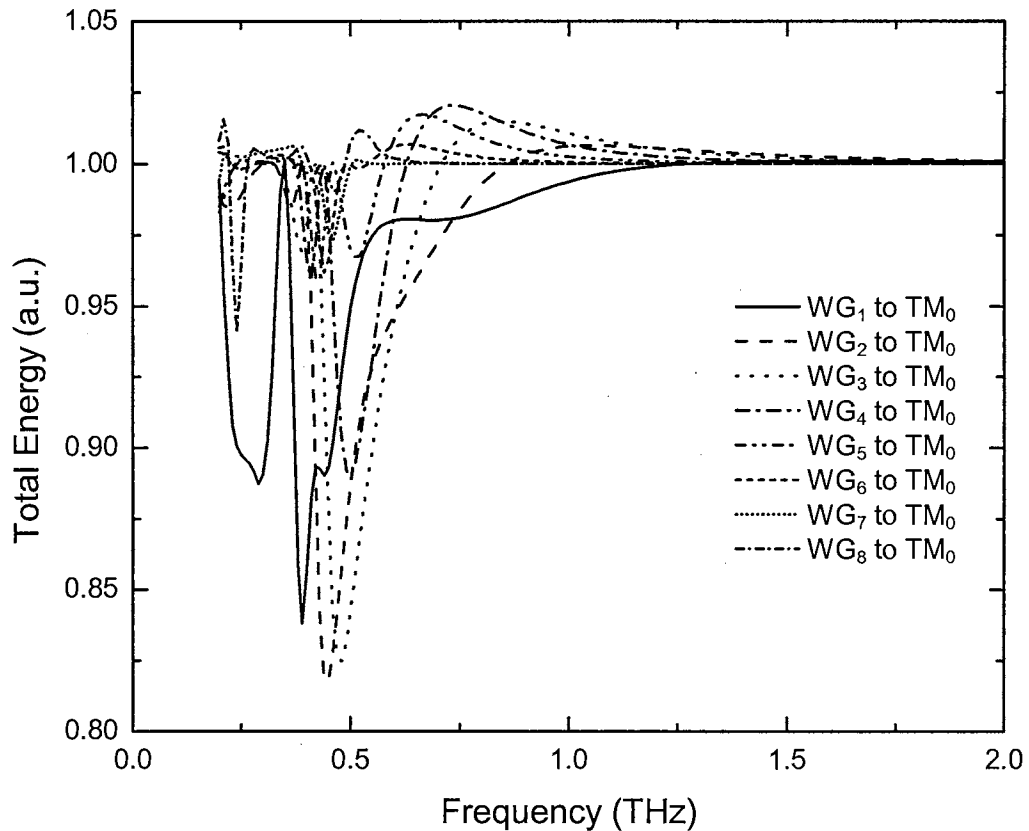


Fig. 6-11 Total power after coupling for the single mode coupling from WG modes to slab TM_0 mode.

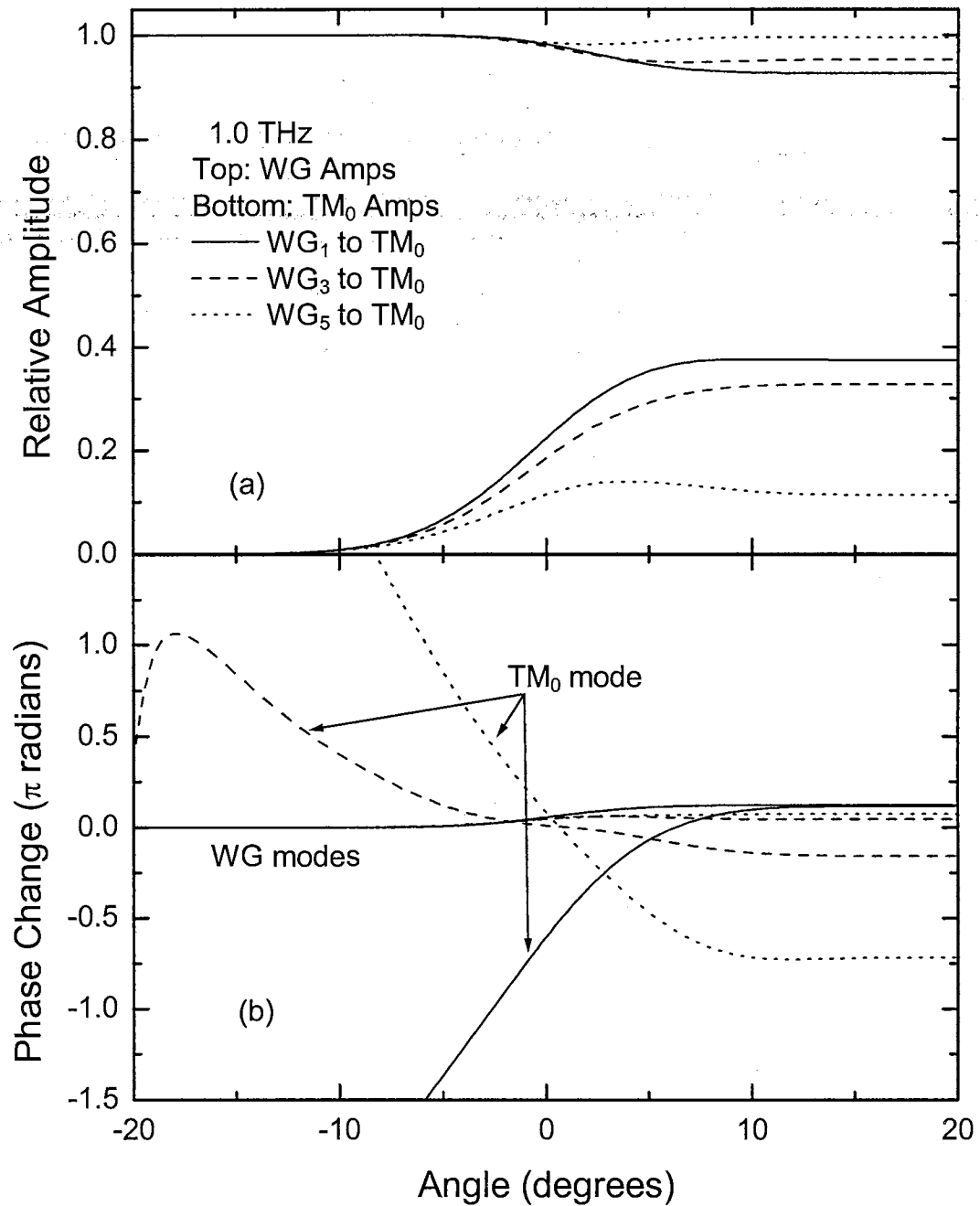


Fig. 6-12 (a) Amplitude and (b) phase change for coupling from WG modes to TM₀ mode at 1.0 THz. The phase changes for the TM₀ mode in (b) have been shifted by integer numbers of 2π so that they fall in the range from $-\pi$ to π at the end of the coupling.

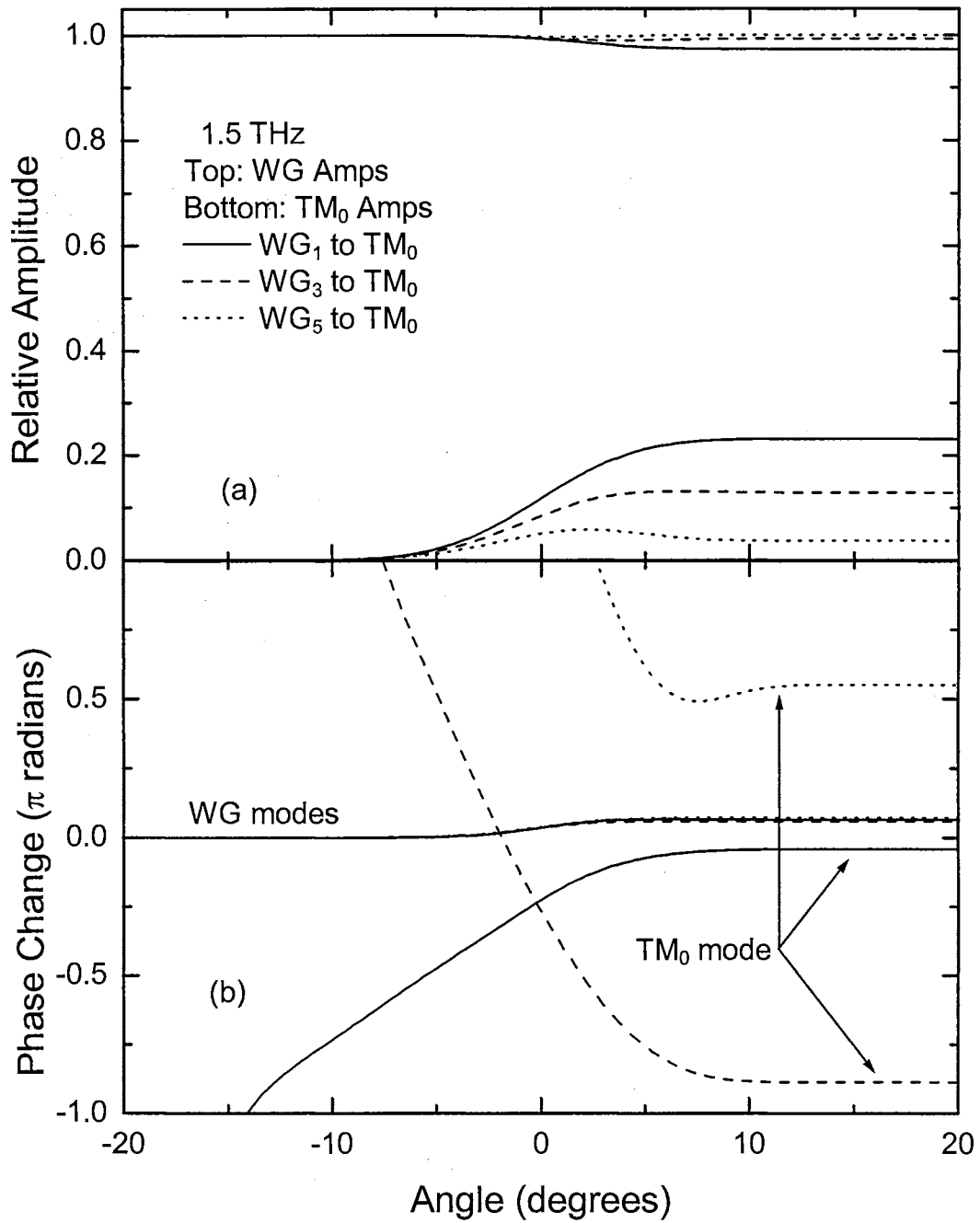


Fig. 6-13 (a) Amplitude and (b) phase change for coupling from WG modes to TM_0 mode at 1.5 THz. The phase changes for the TM_0 mode in (b) have been shifted by integer numbers of 2π so that they fall in the range from $-\pi$ to π at the end of the coupling.

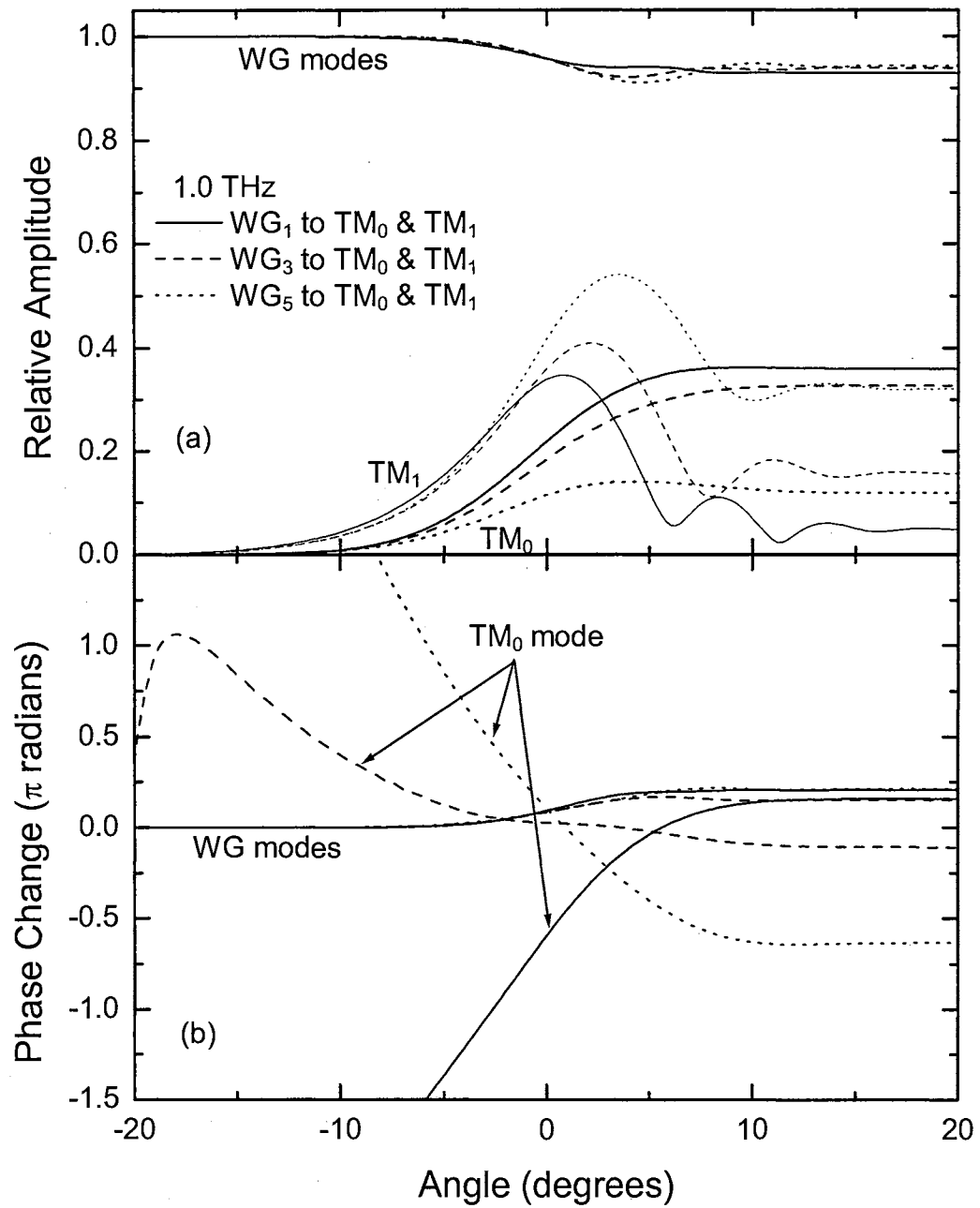


Fig. 6-14 (a) Amplitude and (b) phase change for coupling from WG modes to TM_0 and TM_1 modes at 1.0 THz. The phase changes for the TM_0 mode in (b) have been shifted by integer numbers of 2π so that they fall in the range from $-\pi$ to π at the end of the coupling. The phase change for the TM_1 mode is not plotted.

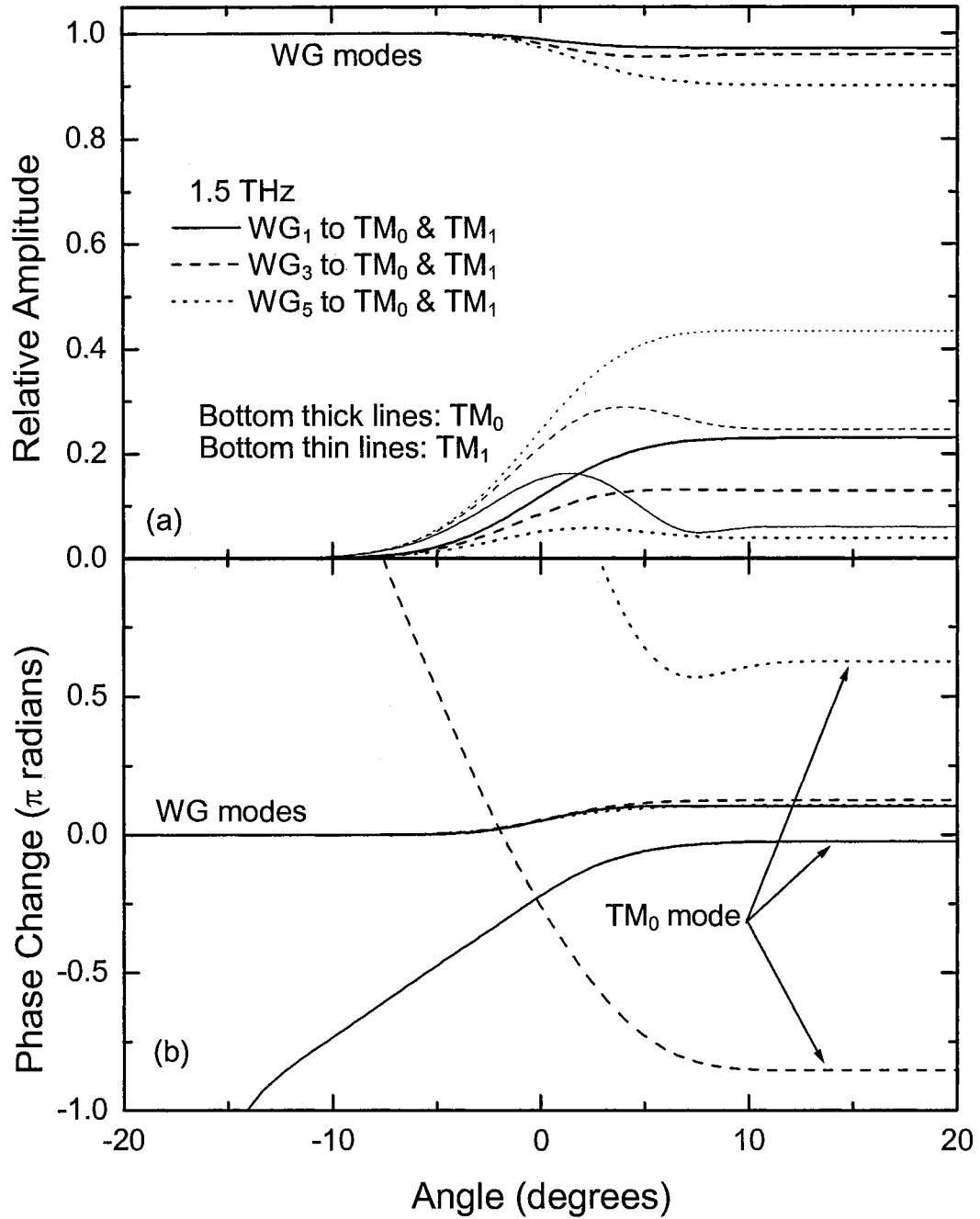


Fig. 6-15 (a) Amplitude and (b) phase change for coupling from WG modes to TM_0 and TM_1 modes at 1.5 THz. The phase changes for the TM_0 mode in (b) have been shifted by integer numbers of 2π so that they fall in the range from $-\pi$ to π at the end of the coupling. The phase change for the TM_1 mode is not plotted.

is not included in the figures. The calculation is achieved by using the coupled mode equations for multimode case (Eq. (5-26) with (5-28)). Though the coupling into the TM_1 mode is strong as shown in Figs. 6-14 and 6-15, neither the amplitude nor the phase has significant change for the TM_0 mode when compared with Figs. 6-12 and 6-13. The WG modes are not depleted much during the coupling process, so that the coupling from WG modes into the TM_0 and TM_1 modes can be viewed as separate couplings and no cross coupling occurs between the slab modes. This explains why the TM_1 mode does not affect the coupling of TM_0 mode. Thus, we can neglect the effect of TM_1 mode in the calculation of the coupling.

6.6 Transfer Functions for Cavity Pulses

Now that we have obtained the single mode coupling results for the coupling between the slab and cylinder, to get the overall coupling results, we need to combine the results for the coupling between the slab TM_0 mode and the individual WG modes.

Using the concept of a frequency-domain transfer function, the output pulses can be viewed as the transformation of the input pulse. If we assume that the complex frequency transfer function of the main transmitted pulse (transmitted pulse in Fig. 3-2 or 3-6) is $H_r(\omega)$, where ω is the angular frequency, then its complex spectrum can be expressed as

$$A_r(\omega) = H_r(\omega)I(\omega), \quad (6-3)$$

where $I(\omega)$ is the complex spectrum of the input pulse shown in Fig. 3-1. In a similar fashion the complex spectrum of the cavity pulses can be written as

$$A_j(\omega) = H_j(\omega)H_r(\omega)I(\omega) = H_j(\omega)A_r(\omega), \quad (6-4)$$

where for the first cavity pulse ($j=1$) the complex transfer function $H_1(\omega)$ is given explicitly by

$$H_1(\omega) = \sum_m a_{cm}^s(\omega)a_{sm}^c(\omega)\exp[i2\pi l_m(\omega)]. \quad (6-5)$$

The modal amplitudes have been calculated as mentioned earlier, the exponential factor on the right side of the above equation is the phase change for the individual WG mode after one round trip propagation around the cylinder, and the summation is over all the cylindrical WG modes. Similarly, for the second cavity pulse ($j=2$), the complex transfer function $H_2(\omega)$ can be expressed as

$$\begin{aligned} H_2(\omega) &= \sum_m a_{cm}^s(\omega)\exp[i2\pi l_m(\omega)]a_{cm}^c(\omega)\exp[i2\pi l_m(\omega)]a_{sm}^c(\omega) \\ &= \sum_m a_{cm}^s(\omega)a_{cm}^c(\omega)a_{sm}^c(\omega)\exp[i4\pi l_m(\omega)], \end{aligned} \quad (6-6)$$

where the exponential factor is the phase change for the individual WG mode after propagating two round trips around the cylinder.

It is worthy to point out that both the coupling structures A and B have the same transfer functions H_1 and H_2 , as they have the same coupling configuration in the open window area. However, the two structures have different H_r 's and consequently different $A_r(\omega)$ profiles as a result of their different sample structures.

In the mode analysis, we have assumed that, in the silicon-filled metal plate waveguide,

the THz pulse propagates in the single TEM mode. Though it is difficult to get a pure TEM mode propagation as mentioned in Chapter II, this assumption will not affect our numerical calculation of the cavity pulses, since the reference pulse is A_r , the main transmitted pulse of the reference scan, and the transfer function H_r cancels out and does not appear in the calculation for the cavity pulses.

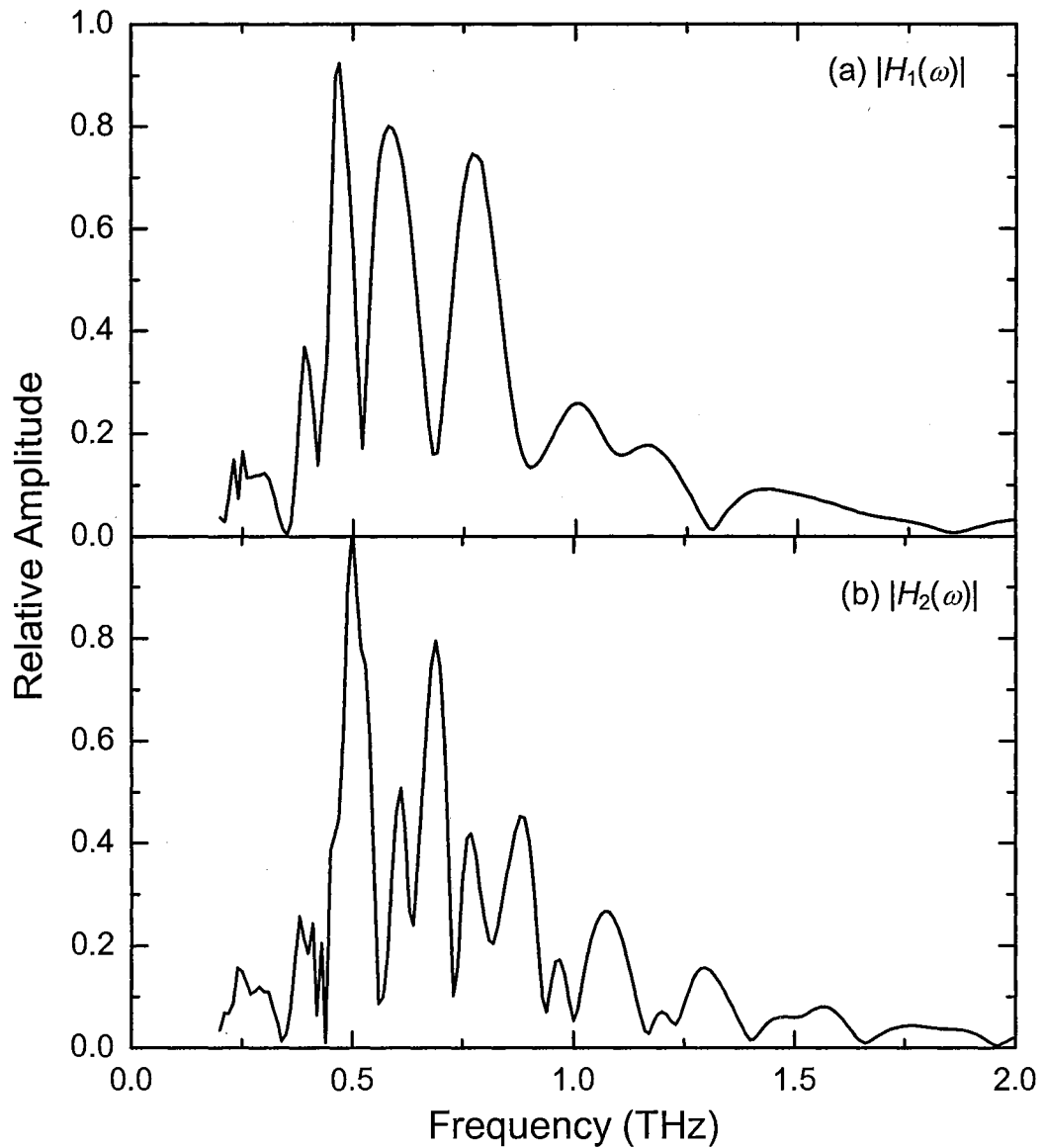


Fig. 6-16 Frequency transfer functions from single mode coupling for (a) the first and (b) the second cavity pulses.

The calculated amplitude transfer functions $|H_1(\omega)|$ and $|H_2(\omega)|$ are presented in Fig. 6-16. They are the combination of the coupling results for the first 8 WG modes and there are no floating parameters in the calculation. As expected, the transfer function for the second cavity pulse is more complicated than that for the first one, as the WGM THz pulse travels longer distance around the cylindrical cavity before coupled out as the second cavity pulse.

6.7 Multimode Coupling from Slab to Cylinder

In Section 6.4 we calculated the coupling from slab TM_0 mode to WG modes using single mode coupling, which assumes that the slab TM_0 mode is not depleted during the coupling and there is no “cross coupling” between the WG modes. Here cross coupling means that the interaction (coupling) of the TM_0 mode with one WG mode does not affect that with another, so the WG modes basically does not feel the existence of other WG modes. This assumption is a very good approximation when calculating the coupling from the cylinder to slab (cylinder excited), as any coupling from the WG-excited TM_0 mode back to another WG mode will be a second-order effect. But for the slab excited case, the power is simultaneously injected into all the WG modes and the single slab TM_0 is depleted, so it is appropriate to use the multimode coupling equations (5-26) with (5-27) to calculate this coupling.

As usual, we use the 4th order Runge-Kutta method to numerically solve Eq. (5-26). The initial values are set as $a_{si}(\omega) = 1$ for the TM_0 mode, and $a_{mi}(\omega) = 0$ for the WG modes. Fig. 6-17 shows the amplitude evolution during the coupling for the TM_0 mode and the WG modes when the first 8 WG modes are considered in the coupling. Fig. 6-17a is the

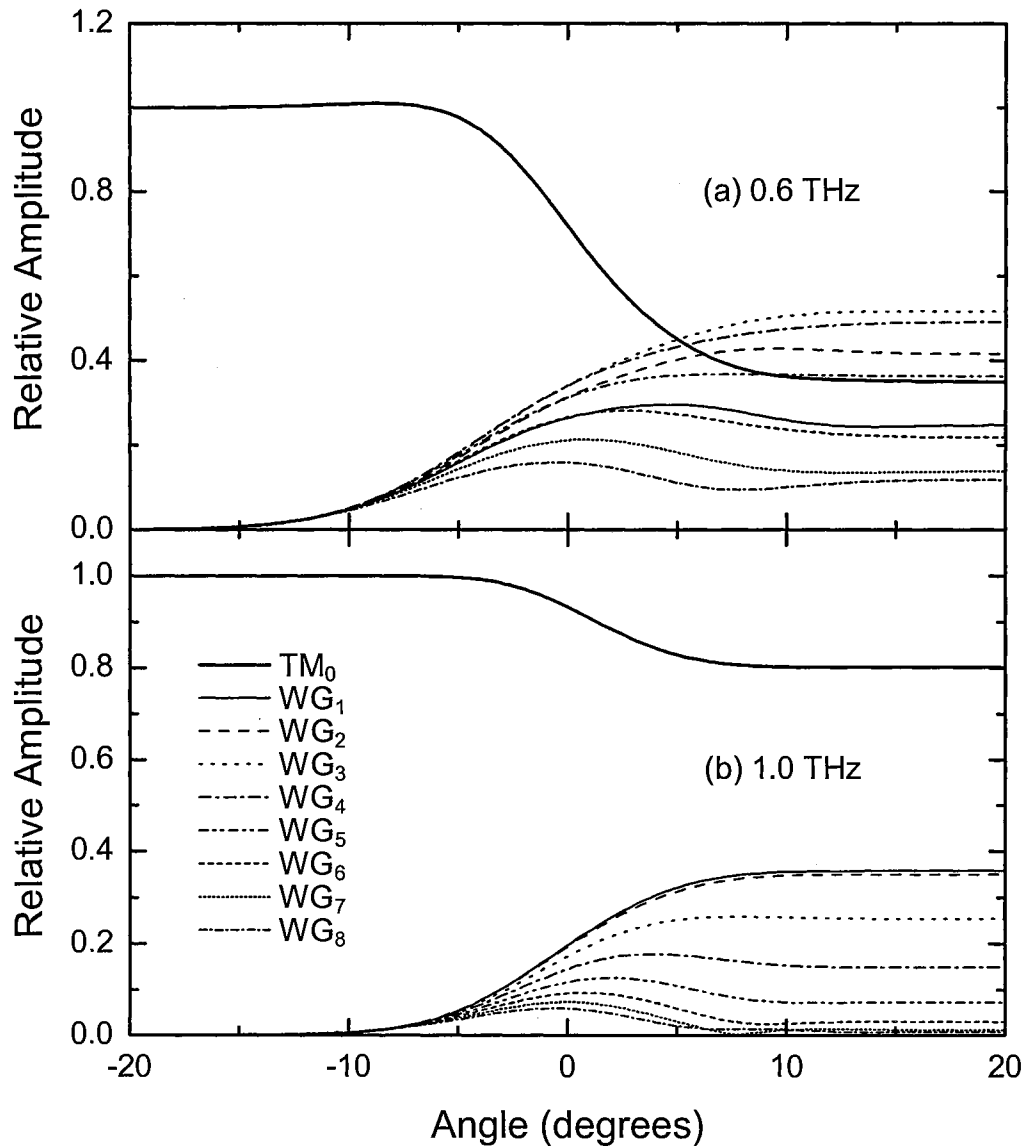


Fig. 6-17 Amplitude evolution of the coupling from TM_0 to WG_1 , WG_2 , ..., and WG_8 modes in the case of multimode coupling at (a) 0.6 THz and (b) 1.0 THz.

results for 0.6 THz and Fig. 6-17b is for 1.0 THz. Comparing Fig. 6-17 with the single mode coupling results shown in Fig. 6-7, we see that the depletion of TM_0 mode causes the decrease of the coupling into the WG modes, as we expected. This decrease effect is bigger at low frequency (0.6 THz) than at higher frequency (THz), since the coupling between the slab and the cylinder is weaker at higher frequency and therefore the depletion effect is weaker.

For the coupling from cylinder to slab, the WG modes couple into the slab TM_0 mode simultaneously. Though it is possible to use the multimode coupling equation to calculate the overall coupling results, since the cross coupling is a second order effect, we still use the single mode coupling results for this coupling. Based on these analyses, the transfer functions for the cavity pulses can still be expressed by Eqs. (6-5) and (6-6), but now $a_{cm}^s(\omega)$ is the final coupling results for the WG_m mode from the multimode calculation. The calculated amplitude transfer functions $|H_1(\omega)|$ and $|H_2(\omega)|$ are plotted in Fig. 6-18. Again they are the combination of the coupling results from the first 8 WG modes.

In addition, it is now possible to get the transfer function for the main transmitted pulse when the cylinder is brought in contact with the slab waveguide. In fact, the final coupled amplitude of the slab TM_0 mode, $a_s^s(\omega)$, is the transfer function for the main pulse. The amplitude part of $a_s^s(\omega)$ is plotted in Fig. 6-19a and its phase part is plotted in Fig. 6-19b.

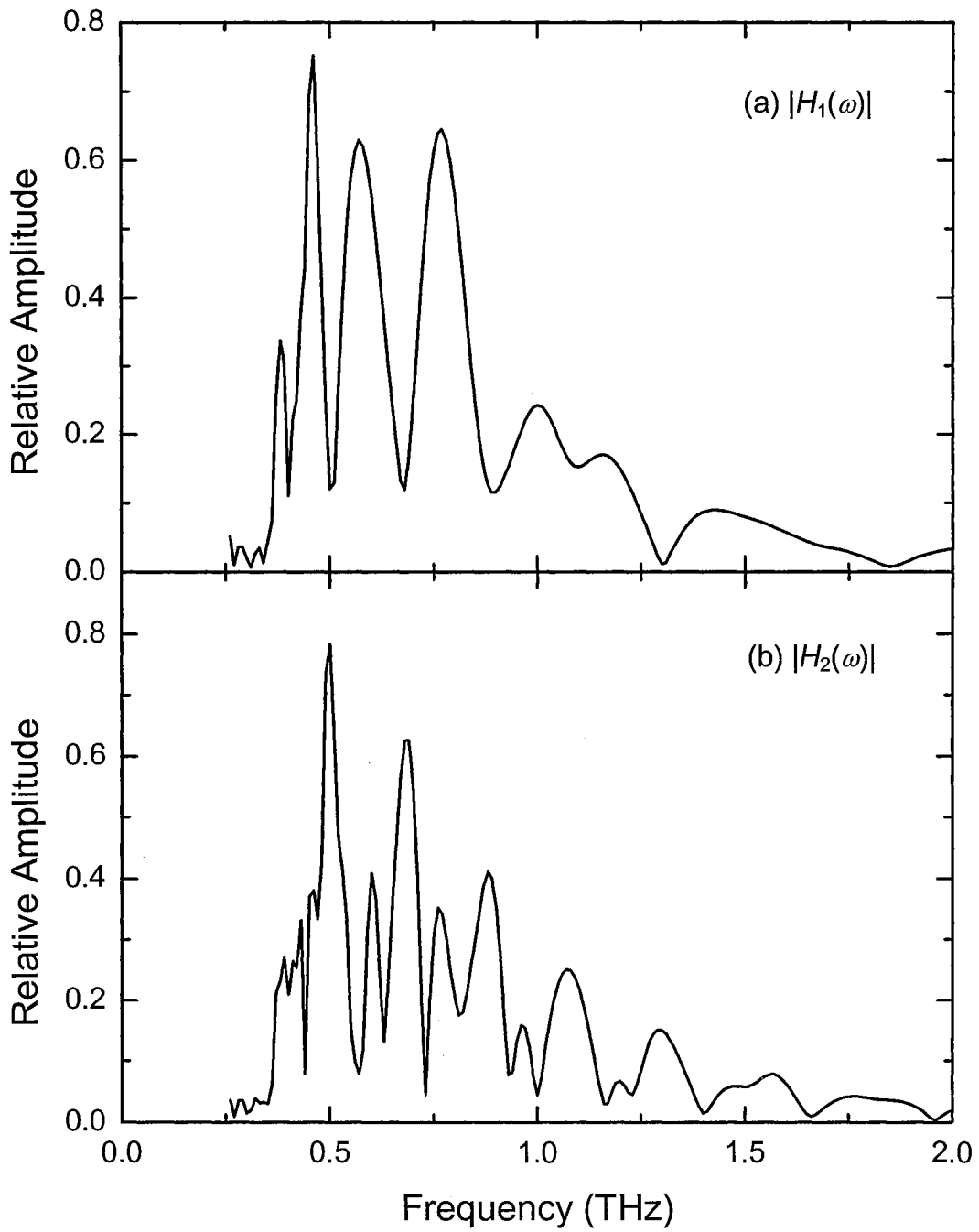


Fig. 6-18 Frequency transfer functions from multimode coupling for (a) the first and (b) the second cavity pulses.

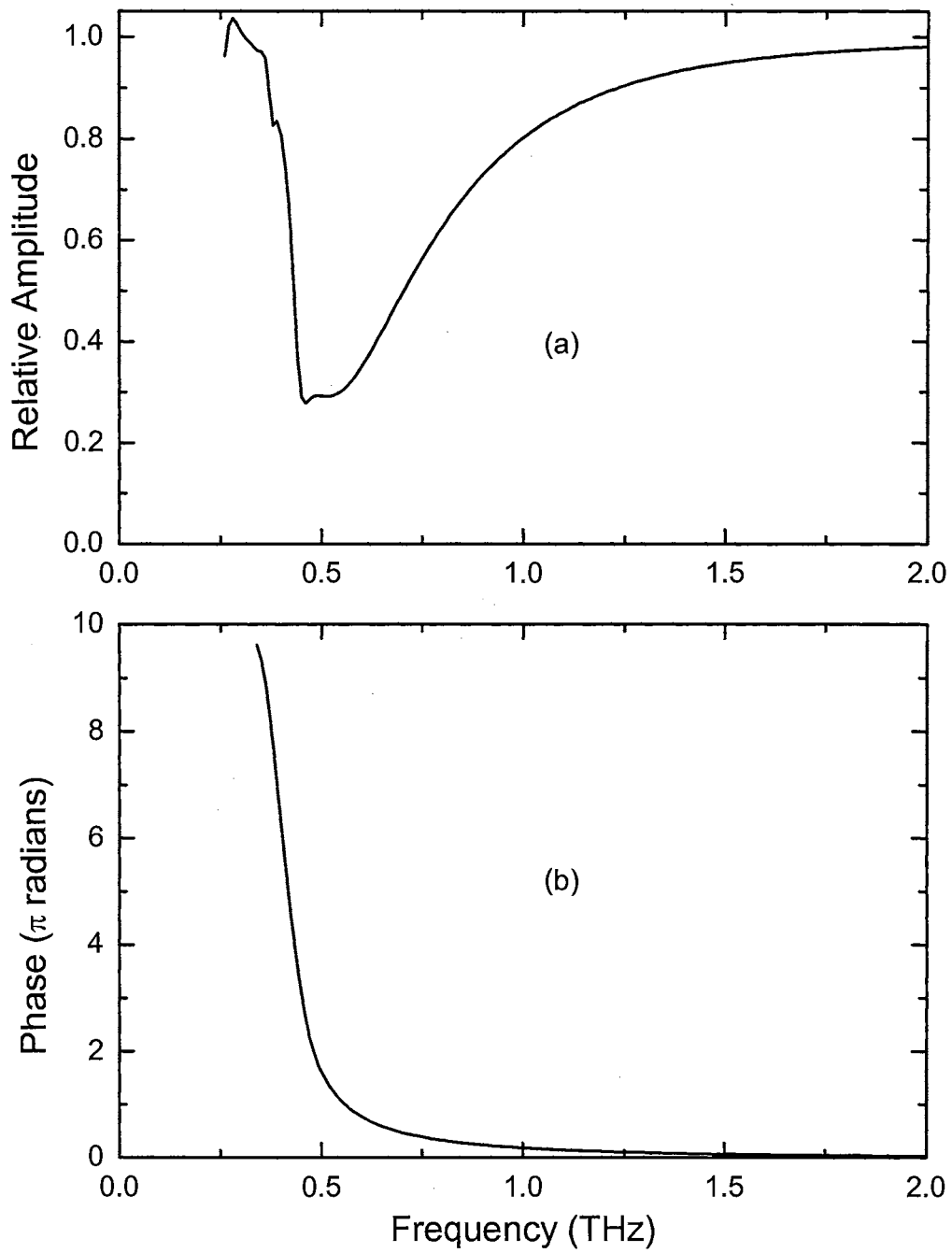


Fig. 6-19 Frequency transfer function for the main transmitted pulse when the cylinder is brought in contact with the slab waveguide. (a) Amplitude; (b) phase.

6.8 Comparison between Experiment and Theory

With the calculated complex frequency domain transfer functions for the cavity pulses, and the measured main transmitted pulse, we are able to calculate the cavity pulses in both the frequency and time domains. We use the multimode coupling results to continue the calculation. For structure A, we take the spectrum of the main transmitted pulse of the reference scan shown in Fig. 3-3c as $A_r(\omega)$, and multiply it with $|H_1(\omega)|$ and $|H_2(\omega)|$ shown in Fig. 6-18, then we get the calculated spectra of the first and the second cavity pulses, which are presented in Fig. 6-20 along with the experimental results. It is seen that theory gives reasonably good agreement with the experiment in the overall structure and magnitude. As expected, the theory gives better explanation to the spectral structure to the first cavity pulse than to the second one, due to the fact that the second cavity pulse propagates longer distance and therefore has more unpredictable feature.

Using the complex spectrum of main transmitted pulse of reference scan and the complex transfer functions $H_1(\omega)$ and $H_2(\omega)$, the pulses are also calculated in time domain and are shown in Fig. 6-21 along with the experiment. Again the theory explains the overall structure and the magnitude of both the cavity pulses.

In addition, the main transmitted pulse can also be predicted by theory when the cylinder is brought contact with the slab. The calculation results are shown in Fig. 6-22a for the spectrum and Fig. 6-22b for the time domain, along with the experimental results. The

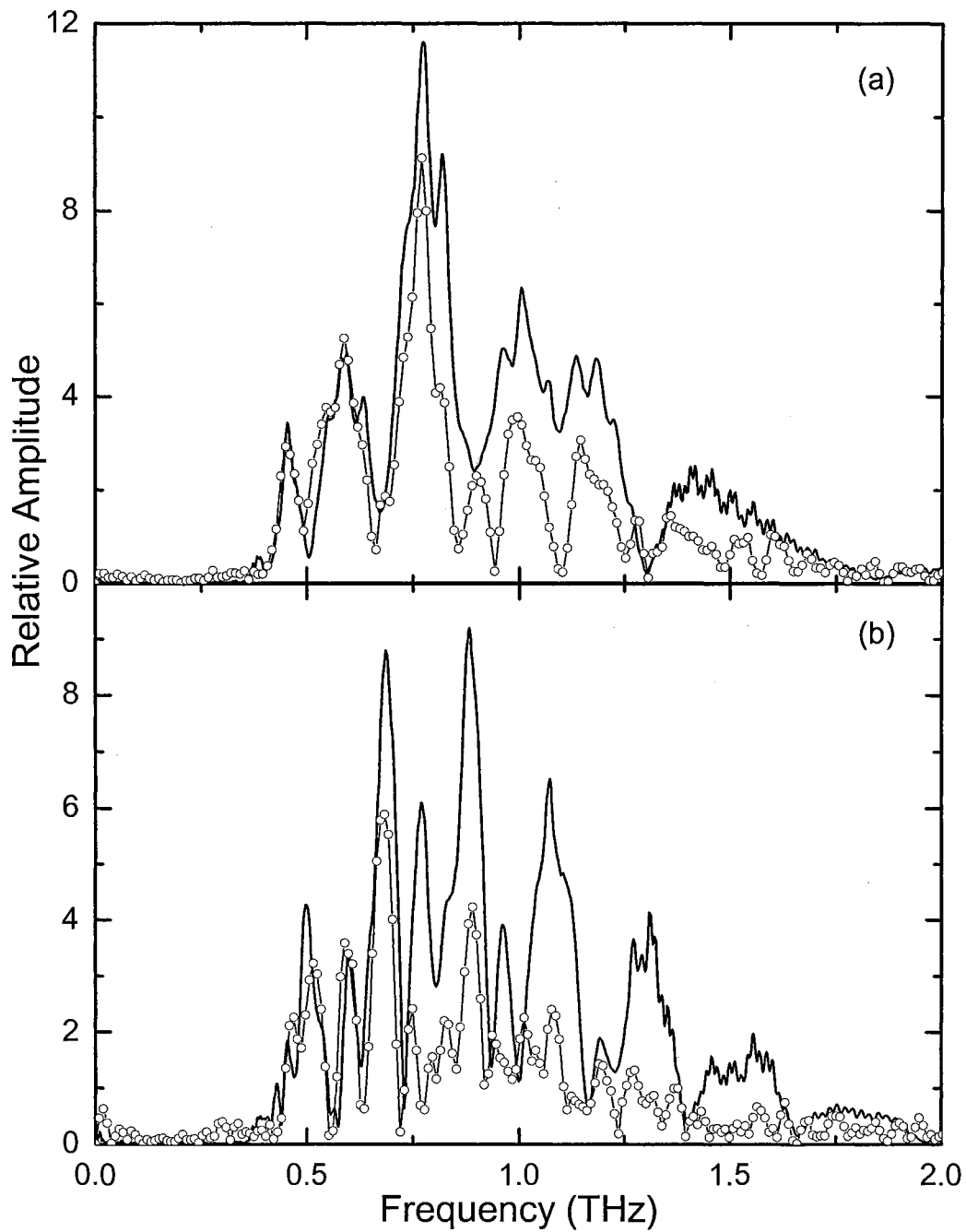


Fig. 6-20 Comparison of the spectra for (a) the first and (b) the second cavity pulses for structure A. The solid lines are the calculated results, and the lines with open circles represent the experimental results.

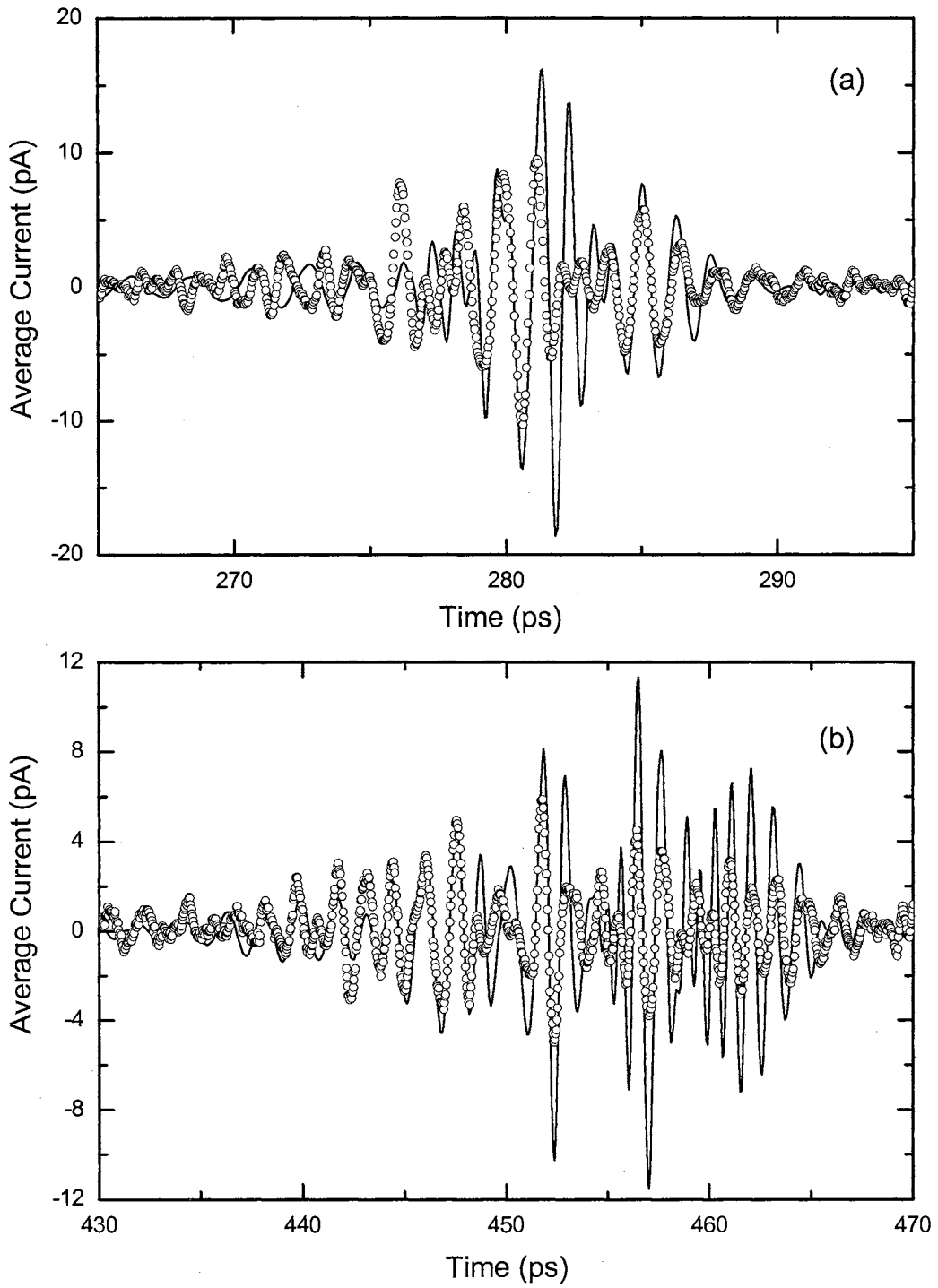


Fig. 6-21 Measured and the calculated results for (a) the first and (b) the second cavity pulses for structure A. The open circles represent the experiment and the solid lines are the calculation results.

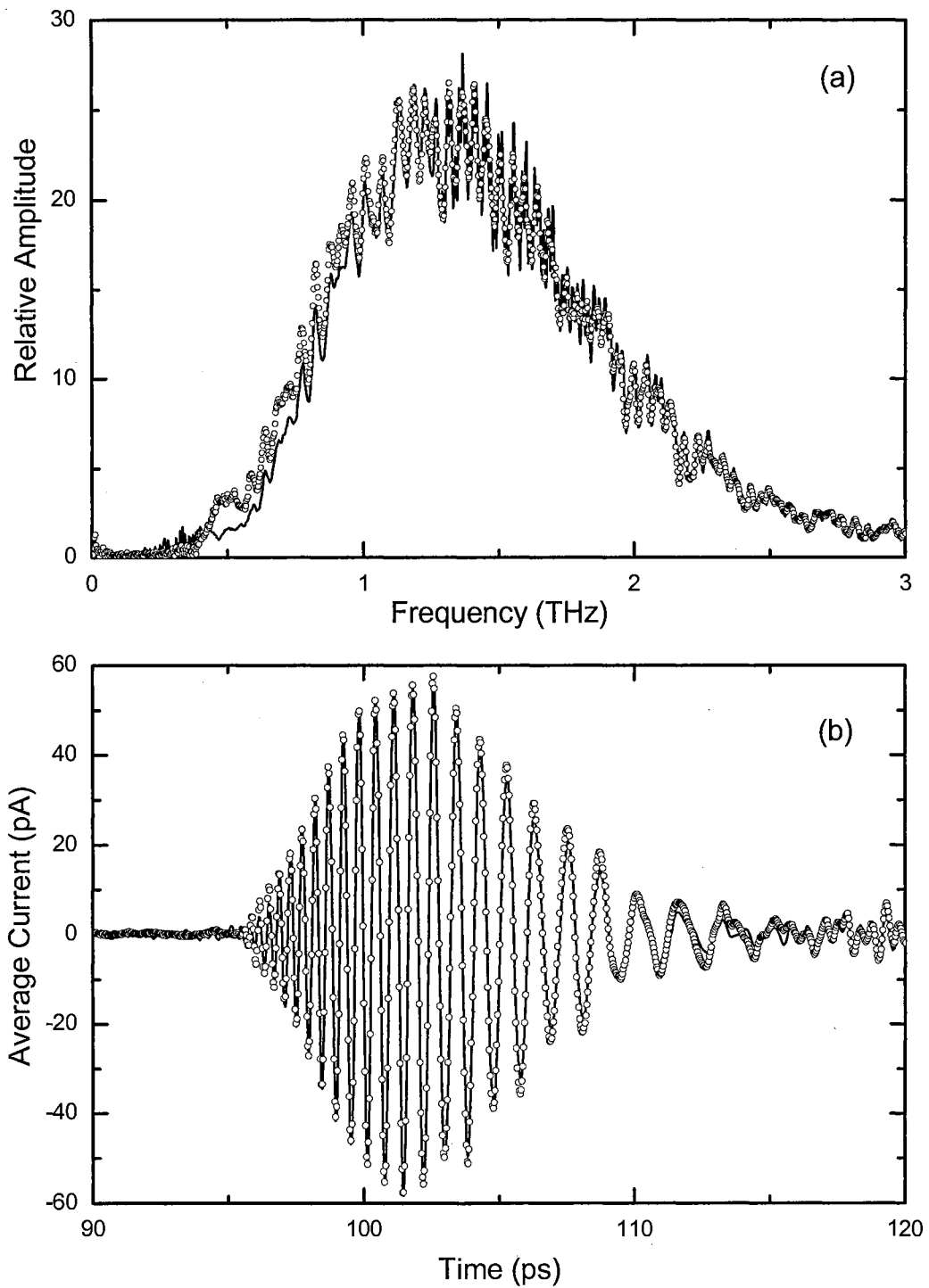


Fig. 6-22 Measured and the calculated results for the main transmitted pulse for structure A. (a) Spectrum. (b) Time domain output pulse. The open circles represent the experiment and the solid lines are the calculation results.

theory gives excellent prediction for this pulse in both the time domain and frequency domain. In the time domain, even the detailed structure is well explained by the theory.

With similar calculations we get the calculation results for structure B. The theoretical and the experimental results for the two cavity pulses are compared in Fig. 6-23 for the frequency domain and in Fig. 6-24 for the time domain. Compared with the results for the structure A, we see that the overall agreement between the theory and the experiment is better for the structure B. In the frequency domain, even though the experimental results show sharper and deeper interference minima than predicted by theory, the overall structure is in good agreement with theory. In the time domain, initially the theoretical oscillation is too slow for the first cavity pulse. However, at about 225 ps, synchronization is obtained and the complicated experimental structure is then in excellent agreement with theory. For the second cavity pulse, initially the theory is out of phase with the experimental oscillations. Starting at about 395 ps excellent agreement between the experimental and theoretical oscillations is obtained, although many experimental maxima are significantly larger than theory.

The calculation results for the main transmitted pulse are shown in Fig. 6-25 along with the experimental results and the reference pulse. Again the theory gives excellent explanation to the experiment. In time domain, the theory gives the replica of the detailed structure of the experiment, demonstrating the suitability of the coupled mode theory.

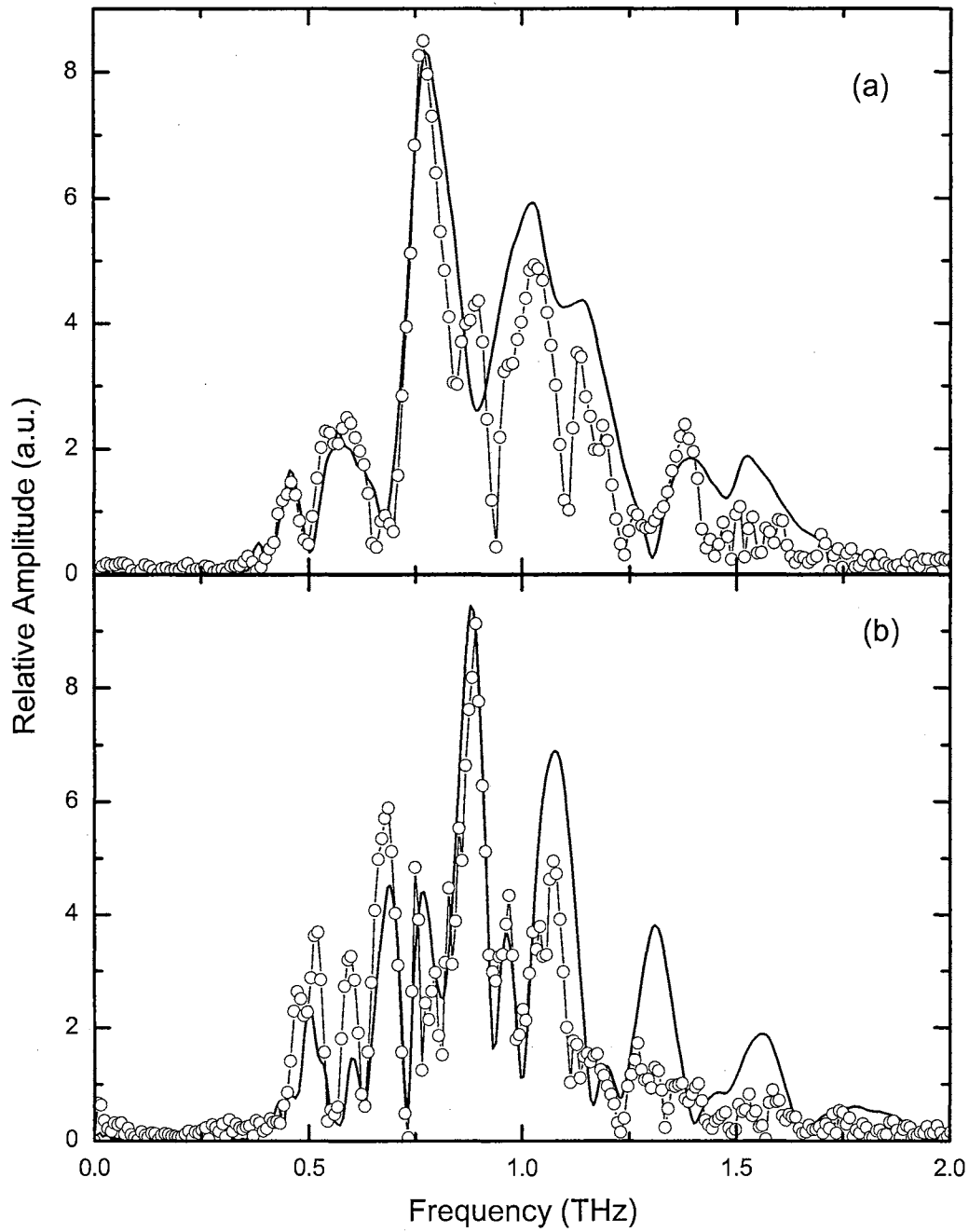


Fig. 6-23 Spectra of (a) the first and (b) the second cavity pulses for structure B. The thin lines with open circles are experiment and the thick solid lines represent the calculation results.

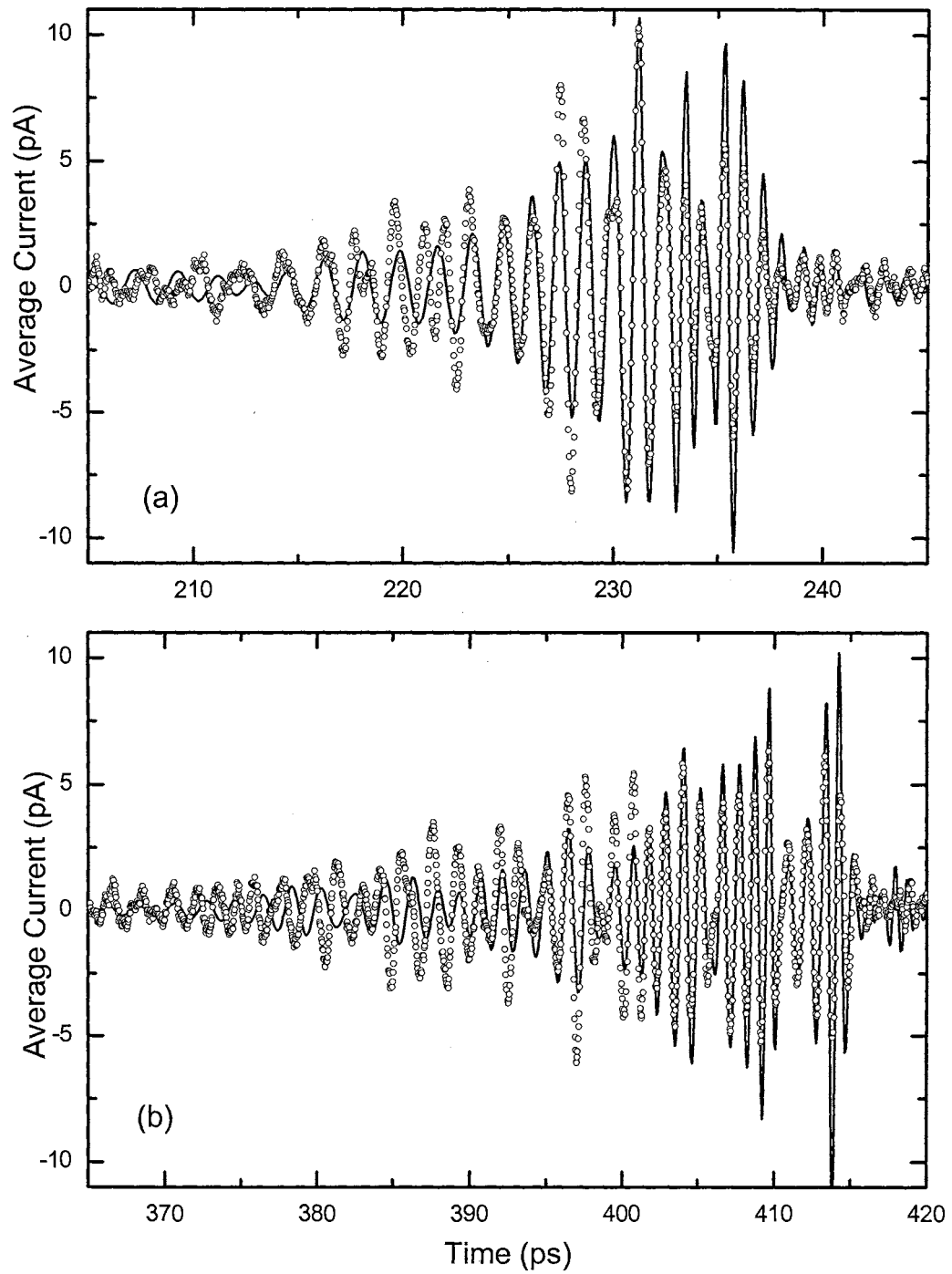


Fig. 6-24 Measured and calculated results of (a) the first and (b) the second cavity pulses for structure B. The open circles represent the experiment and the solid lines are calculation results.

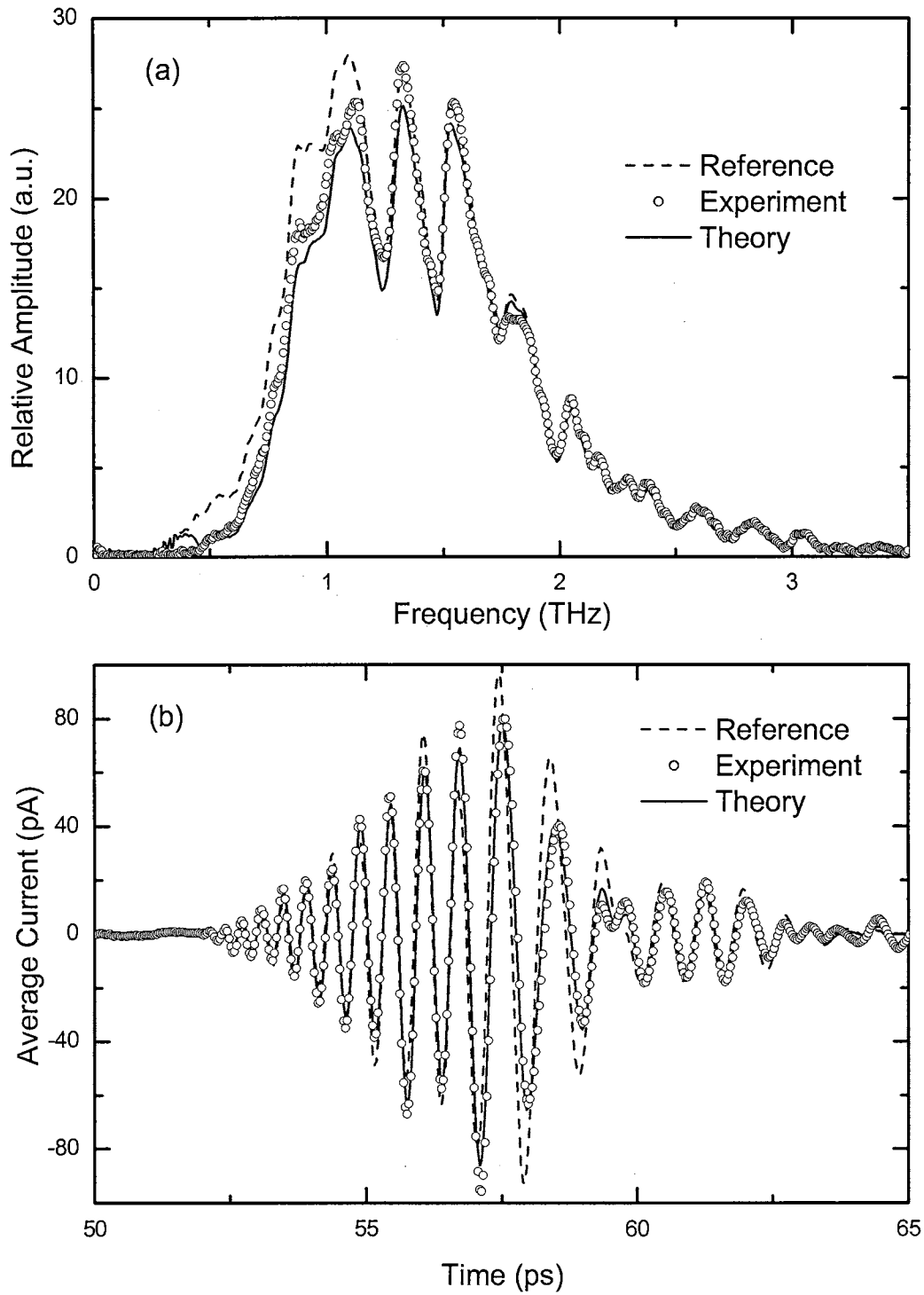


Fig. 6-25 Measured and calculated results for the main transmitted pulse for structure B, along with the reference pulse. (a) Spectra. (b) Time domain output pulses.

The discrepancies between theory and experiment are considered to be due to limitations in numerical calculations. The observed rapidly oscillating structures in both the time and frequency domains involve constructive and destructive interference among the first eight WG modes of the cylinder. This interference is determined by the complex product of coupling results $a_{cm}^s a_{sm}^c$ and the relative phase difference between the WG modes caused by propagation around the cylinder. For example, the relative phase difference at 1.0 THz due to propagating one time around the cylinder for the first two WG modes is $(7.78)(2\pi)$ radians, which is approximately 5% of their total phase angle for this propagation. This result shows the sensitivity of the system, in which a small error in the total calculated phase can lead to a large error in the predicted interference. Consequently, the numerical calculation for the WGM total phase angles must be performed to an accuracy of better than 0.1%.

Fig. 6-26 shows the comparison between the calculated and measured transfer functions for the main transmitted pulse for both structures A and B. For structure B, it is seen that the overall agreement between the theory and experiment is fairly good above 0.5 THz. Below 0.5 THz, the experimental results seem unpredictable by the theory, as expected. For structure A, the discrepancy between theory and experiment is larger, due to the alignment problem. At above 1.0 THz, there are oscillations in the experimental results for both structures. However, the cause of these oscillations is yet to be determined.

In calculating the transfer functions, there are no floating parameters. The thickness of the slab waveguides and the diameter of the cylinder were measured using a micrometer

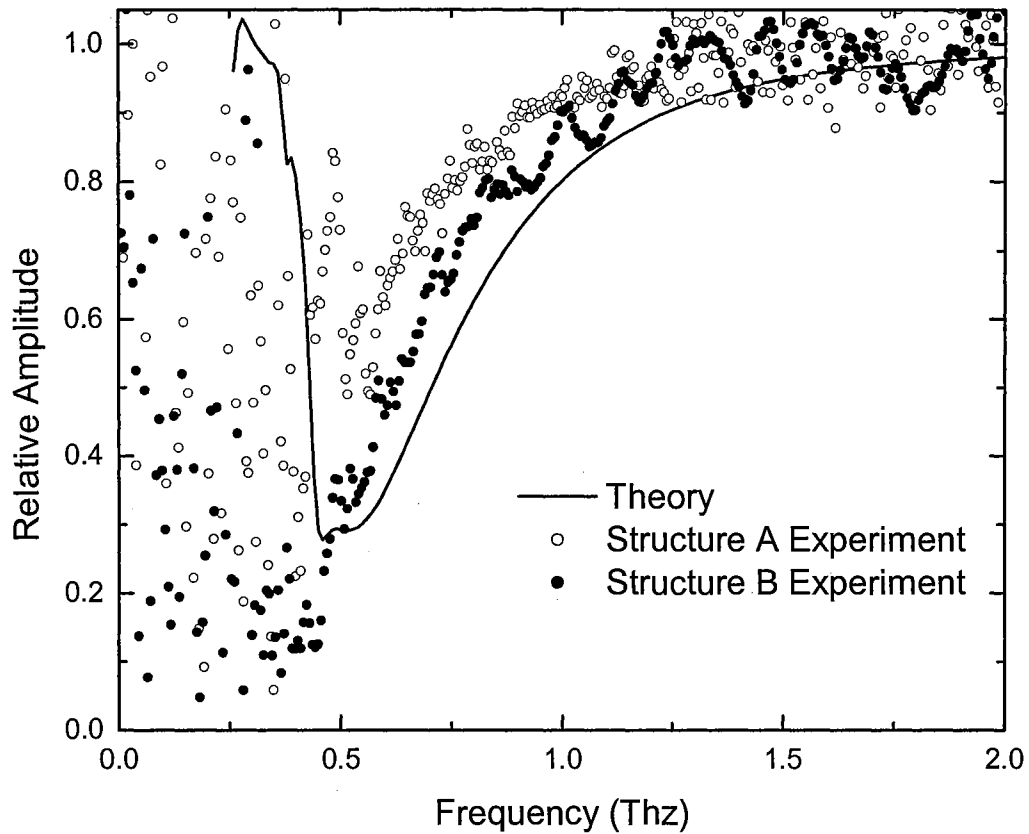


Fig. 6-26 Comparison of the transfer functions of the main transmitted pulse for structure B. Solid: calculation results; open circles: experiment.

with an accuracy of $10 \mu\text{m}$, and the refractive index of the silicon is from experimental measurement [23]. The calculated spectra and output pulses of the main transmitted pulses, and the calculated spectra of the cavity pulses are the exact calculation results. However, the calculated results for the time domain pulse for the cavity pulses have been shifted to get the maximal oscillation match to the experimental data. The time shifts for the cavity pulses are as follows:

Structure A:

First cavity pulse: shifted by 3.2 ps;

Second cavity pulse: shifted by 5.5 ps;

Structure B:

First cavity pulse: shifted by 2.6 ps;

Second cavity pulse: shifted by 5.1 ps.

The sources of this discrepancy are considered to be as follows: accuracy of the measurement of the diameter of the cylinder, accuracy of the phase term in the calculation of the modal amplitudes. Since the calculation of phase is more easily affected by any approximations, we believe that the latter is the main source of the discrepancy.

The calculation results for structure B give better explanation the experiment than that for structure A. As we have mentioned in Chapter II, due to the cylinder holder problem, it is very difficult to align the cylinder for structure A. We believe that in the experiment, the cylinder is not optimally aligned for structure A, so the experimental results is not satisfactory.

In general, the coupled mode theory gives good explanation to the experimental results for both the coupling structures. The overall structure and magnitude of the experimental results are predicted by the theory. With a shorter open window, structure B effectively reduces the broadening of the main transmitted pulse and hence the reflection ones, and the cavity pulses have a larger SNR over a longer time range. All these factors contribute to a better agreement between the theory and experiment for structure B.

CHAPTER VII

CONCLUSIONS AND PERSPECTIVES

We have successfully demonstrated a dielectric cylindrical WGM cavity for THz pulses. The THz pulses are coupled into and out of the cylindrical cavity via a dielectric slab waveguide. The coupled THz pulse inside the cavity is composed of several WGM modes. The continuous oscillation of the WGM-THz pulse inside the cylinder and the coupling between the slab waveguide and the cylinder generate a cavity pulse train with a constant period. The first two cavity pulses coupled out of the cylindrical cavity are observed, and thereby demonstrate the strong coupling between the slab waveguide and the cylinder.

Since our coupling source is subps THz pulses, the observed cavity pulses cover a continuous frequency range from 0.4 THz to 1.8 THz, instead of discrete frequency points as in the case of using a cw laser as the coupling source. Due to the multimode feature of the WGM-THz pulse, the cavity pulses show spectral oscillations. The group velocity dispersion of the WGM modes caused frequency chirp and pulse broadening of the cavity pulses; the second cavity pulse has more complicated patterns in both the frequency and time domains than the first cavity pulse.

The metal plates used in the coupling structures force the incoming THz pulse couple into single mode propagation of the low-loss, non-dispersive TEM mode of the metal plate waveguide, which effectively reduces the pulse broadening and frequency chirp of the main transmitted pulse. In the open window area, the THz pulse propagates as a combination of the dominant TM_0 mode and the minor TM_2 mode. Upon passing the second metal plate waveguide, the TM_2 mode is basically filtered out, so the THz receiver essentially detects a single TM_0 propagation in the slab waveguide.

A coupled mode theory in cylindrical coordinates has been developed to analyze this coupling structure. Through the single mode and multimode coupling calculation, we calculate the coupling between the single slab TM_0 mode and the individual WG mode, and then combine the results to get the overall coupling results. The theory gives reasonably good explanation to the experimental results in both the frequency and time domains. Since structure B has a shorter open window and thus a shorter transmitted pulse, the cavity pulses from this structure have a better SNR and are better explained by the theory.

This study demonstrates the feasibility of the slab-cylinder structure as an effective coupling scheme for the THz WGM cavity. Since the coupling source is a subps THz pulse instead of a cw wave, the coherence condition is not required for the coupled WGM modes; hence the cavity pulses cover a continuous frequency range, instead of the discrete frequency points. Since the WGM modes travel with different group and phase

velocities, the WGM pulse is broadened as it propagates; different cavity pulses carry different spectrum profiles due to the interference between the modes upon detection. Clearly, this structure is an excellent choice to study the propagation properties of single subps pulse of THz radiation propagating in the WGM modes of a cylinder.

As the recent progress in THz waveguide studies [34-38] has made possible the guided wave propagation and circuit interconnection of THz radiation, this structure may be a promising coupler and resonator for future THz integrated circuits.

To our knowledge, this is the first experimental demonstration of WGM cavity for THz radiation. As mentioned earlier, the unique feature of this study is the use of the subps THz pulse as the coupling source. This feature makes it possible to separate the cavity pulses in the time domain, which is essential in studying the propagation properties of WGM modes. However, the broad spectral band of the coupling source also makes it difficult to obtain a single mode coupling into the WGM cavity. As we have seen, multimode propagation of the WGM modes causes pulse broadening and frequency chirp, which is not desirable in communication-related circuits. A solution to the single mode coupling is to narrow the spectral range of the coupling source. If we look back at the dispersion relation shown in Fig. 6-3, it is possible that, by adjusting the dimensions of the slab waveguide and the cylindrical cavity, only a single WGM mode has a suitable phase match relation with the slab TM_0 mode within a certain frequency range. If the spectral range of the coupling source can be limited in this frequency range, then we shall get a fairly good single mode coupling into the WGM cavity. Recently, progress has

been made on the study of tunable THz sources, and widely tunable THz sources are available in the frequency range from 0.7 THz to 3.0 THz, with a narrow bandwidth of about 0.02—0.1 THz [56,57]. It will be of great importance and interest to realize a single mode coupling into the WGM cavity using these new THz sources. It is expected that the propagation properties of a single mode WGM pulse will differ from the multimode one, as the pulse broadening and frequency chirp problem will be solved.

It is also possible to modify the coupling structure in order to obtain a single mode coupling. Since single mode propagation of THz radiation has already been realized in ribbon and metal waveguides, a circular version of these waveguides could make good THz cavities. However, the excited modes inside this kind of cavities will no longer be WGM modes.

WGM resonators are widely used in millimeter wavelength circuits as frequency filters. In THz region, as long as the coupling source is a subps pulse, the cylindrical cavity cannot serve as a frequency filter, due to the fact that it can support continuous frequency range. However, a wide-band WGM resonator is also important in future THz circuits, as it can be used for power combiner or mixer for broadband THz signals.

Starting from the current work, there are still more that could be done in the future, which are of both theoretical and experimental interests. A change of the polarization of the input THz beam will result in the excitation of another set of WGM modes. The WGM modes of new polarization would have different coupling and propagation properties. As

mentioned earlier, the change in the dimensions of the both the slab waveguide and the cylindrical cavity would result in different coupling features. A combination of these changes (polarization and dimensions) may give us a frequency band selection and mode selection.

Another interesting problem is the directional coupler. Right now our input coupler and the output coupler is the same slab waveguide. It would be of great interest and important if we could use a second coupler as the output coupler. It would be possible to tune the output frequency band by adjusting the dimensions of the output coupler. This way we would have more options in selecting the frequency and mode of the coupled THz pulse, and thus more flexibility in the future use of this coupling structure.

The searching of new coupling structures for THz cavities is yet to continue in the future.

As this study has opened a new area of study in THz frequency region, we believe that THz technology will find more applications in the future in both scientific research and everyday life.

BIBLIOGRAPHY

1. H. M. Nussenzveig, *Diffraction Effects in Semiclassical Scattering* (Cambridge University Press, Cambridge, 1992).
2. X. H. Jiao, P. Guillon P, And J. Obregon, “Theoretical-analysis of the coupling between whispering-gallery dielectric resonator modes and transmission-lines”, *Electron. Lett.* **21**, 88-89 (1985).
3. L. Collot, V. Lefèvr-Seguin, M. Brune, J. M. Raimond, and S. Haroche, “Very high- Q whispering-gallery mode resonances observed in fused silica microspheres”, *Europhys. Lett.* **23**, 327-334 (1993).
4. C. Vedrenne and J. Arnaud, “Whispering-Gallery modes of dielectric resonators”, *IEE Proc. H* **129**, 183-187 (1982).
5. D. Crod and P. Guillon, “Whispering gallery dielectric resonator modes for W -band devices”, *IEEE Trans. Microwave Theory Tech.* **38**, 1667-1674 (1990).
6. V. Sandoghdar, F. Treussart, J. Hare, V. Lefèvr-Seguin, J.-M. Raimond, and S. Haroche, “Very low threshold whispering-gallery-mode microsphere laser”, *Phys. Rev. A* **54**, R1777-1780 (1996).
7. A. C. R. Pipino, J. W. Hudgens, and R. E. Huie, “Evanescent wave cavity ring-down spectroscopy with a total-internal reflection minicavity”, *Rev. Sci. Instrum.* **68**, 2978-2989 (1997).

8. M. Cai, O. Painter, and K. J. Vahala, "Observation of critical coupling in a fiber taper to a silica-microsphere whispering-gallery mode system", *Phys. Rev. Lett.* **85**, 74-77 (2000).
9. D. W. Vernooy, A. Furusawa, N. Ph. Georgiades, V. S. Ilchenko, and H. J. Kimble, "Cavity QED with high- Q whispering gallery modes", *Phys. Rev. A* **57**, R2293-R2296 (1998).
10. S. Schiller and R. L. Byer, "High-resolution spectroscopy of whispering gallery modes in large dielectrics", *Opt. Lett.*, **16**, 1138-1140 (1991).
11. A. L. Huston, J. D. Eversole, "Strain-sensitive elastic-scattering from cylinders", *Opt. Lett.* **18**, 1104-1106 (1993).
12. V. S. Ilchenko, P. S. Volikov, V. L. Velichansky, F. Treussart, V. Lefèvre-Seguin, J.-M. Raimond, and S. Haroche, "Strain-tunable high- Q optical microsphere resonator", *Opt. Comm.* **145**, 86-90 (1998).
13. D. C. Bownass, J. S. Barton, and J. D. C. Jones, "Detection of high humidity by optical fibre sensing at telecommunications wavelengths", *Opt. Comm.* **146**, 90-94 (1998).
14. Y. Tomabechi, J. Hwang, and K. Matsumura, "Resonance characteristics on a dielectric disk resonator coupled with a straight waveguide", *Radio Sci.* **31**, 1809-1814 (1996).
15. Jiangquan Zhang and D. Grischkowsky, "Whispering-gallery mode terahertz pulses", *Opt. Lett.* **27**, 661-663 (2002).
16. G. Annino, D. Bertolini, M. Cassettari, M. Fittipaldi, I. Longo, and M. Martinelli, "Dielectric properties of materials using whispering gallery dielectric resonators: Experiments and perspectives of ultra-wideband characterization", *J. Chem. Phys.* **112**, 2308-2314 (2000).

17. D. Braunstein, A. M. Khazanov, G. A. Koganov, and R. Shuker, "Lowering of threshold conditions for nonlinear effects in a microsphere", *Phys. Rev. A* **53**, 3565-3572 (1996).
18. A. T. Rosenberger, "Nonlinear optical effects in the whispering-gallery modes of microspheres", in *Operational Characteristics and Crystal Growth of Nonlinear Optical Materials*, R. B. Lal and D. O. Frazier, eds., Proc. SPIE **3793**, 179-186 (1999).
19. J. Krupka, K. Derzakowski, and A. Abramowicz, "Use of whispering-gallery modes for complex permittivity determinations of ultra-low-loss dielectric materials", *IEEE Trans. Microwave Theory Tech.* **47**, 752-759 (1999).
20. A. T. Rosenberger and J. P. Rezac, "Whispering-gallery-mode evanescent-wave microsensor for trace-gas detection", in *Biomedical Instrumentation Based on Micro- and Nanotechnology*, R. P. Mariella and D. V. Nicolau, eds., Proc. SPIE **4265**, 102-112 (2001).
21. D. H. Auston, K. P. Cheung, and P. R. Smith, "Picosecond photoconducting Hertzian dipoles", *Appl. Phys. Lett.* **45**, 284-286 (1984).
22. M. B. Ketchen, D. Grischkowsky, T. C. Chen, C-C. Chi, I. N. Duling, III, N. J. Halas, J-M. Halbout, J. A. Kash, and G. P. Li, "Generation of subpicosecond electrical pulses on coplanar transmission lines", *Appl. Phys. Lett.* **48**, 751-753 (1986).
23. D. Grischkowsky, S. Keiding, M. van Exter, and Ch. Fattinger, "Far-infrared time-domain spectroscopy with terahertz beams of dielectrics and semiconductors", *J. Opt. Soc. Am. B* **7**, 2006-2015 (1990).
24. B. B. Hu and M. C. Nuss, "Imaging with terahertz waves", *Opt. Lett.* **20**, 1716-1719 (1995).
25. J. O'Hara and D. Grischkowsky, "Quasi-optic terahertz imaging", *Opt. Lett.* **26**, 1918-1920 (2001).

26. R. A. Cheville, R. W. McGowan, and D. Grischkowsky, "Late-time target response measured with THz impulse ranging", *IEEE Trans. Antennas and Prop.* **45**, 1518-1524 (1997).
27. Tae-In Jeon and D. Grischkowsky, "Nature of conduction in doped silicon", *Phys. Rev. Lett.* **78**, 1106-1109 (1997).
28. G. Gallot, Jiangquan Zhang, Tae-In Jeon, and D. Grischkowsky, "Measurements of the THz absorption and dispersion of ZnTe and their relevance to the electro-optic detection of THz radiation", *Appl. Phys. Lett.* **74**, 3450-3452 (1999).
29. Ch. Fattinger and D. Grischkowsky, "Terahertz beams", *Appl. Phys. Lett.* **54**, 490-492 (1989).
30. M. van Exter and D. Grischkowsky, "Characterization of an optoelectronic terahertz beam system", *IEEE Trans. Microwave Theory Tech.* **38**, 1684-1691 (1990).
31. D. Grischkowsky, I. N. Duling, III, J. C. Chen, and C.-C. Chi, "Electromagnetic shock waves from transmission lines", *Phys. Rev. Lett.* **59**, 1663-1666 (1987).
32. H. Roskos, M. C. Nuss, K. W. Goossen, D. W. Kisker, A. E. White, K. T. Short, D. C. Jacobson, and J. M. Poate, "Propagation of picosecond electrical pulses on a silicon-based microstrip line with buried cobalt silicide ground plane", *Appl. Phys. Lett.* **58**, 2598-2600 (1991).
33. R. W. McGowan, G. Gallot, and D. Grischkowsky, "Propagation of ultrawideband short pulses of terahertz radiation through submillimeter-diameter circular waveguides", *Opt. Lett.* **24**, 1431-1433 (1999).
34. G. Gallot, S. P. Jamison, R. W. McGowan, and D. Grischkowsky, "THz waveguides", *J. Opt. Soc. Am. B* **17**, 852-863 (2000).
35. S. P. Jamison, R. W. McGowan, and D. Grischkowsky, "Single-mode waveguide propagation and reshaping of sub-ps terahertz pulses in sapphire fibers", *Appl. Phys. Lett.* **76**, 1987-1989 (2000).

36. R. Mendis and D. Grischkowsky, "Plastic ribbon THz waveguides", *J. Appl. Phys.* **88**, 4449-4451 (2000).
37. R. Mendis and D. Grischkowsky, "Undistorted guided wave propagation of sub-picosecond THz pulses", *Opt. Lett.* **26**, 846-848 (2001).
38. R. Mendis and D. Grischkowsky, "THz interconnect with low-loss and low-group velocity dispersion", *IEEE Microwave Wireless Component Lett.* **11**, 444-446 (2001).
39. V. B. Braginsky, M. L. Gorodetsky, and V. S. Ilchenko, "Quality factor and nonlinear properties of optical whispering-gallery modes", *Appl. Phys. Lett. A.* **137**, 393-397 (1989).
40. M. van Exter, Ch. Fattering, and D. Grischkowsky, "Terahertz time-domain spectroscopy of water vapor", *Opt. Lett.* **14**, 1128-1130 (1989).
41. N. Marcuvitz, *Waveguide Handbook* (Peter Peregrinus, London) (1993).
42. A. W. Snyder and J. D. Love, *Optical Waveguide Theory* (Chapman and Hall, New York) (1983).
43. X. H. Jiao, P. Guillon, and L. A. Bermudez, "Resonant frequencies of whispering-gallery dielectric resonator modes", *IEE Proc.-H* **134**, 497-501 (1987).
44. G. Annino, M. Cassettari, I. Longo, and M. Martinelli, "Whispering gallery modes in a dielectric resonator: characterization at millimeter wavelength", *IEEE Trans. Microwave Theory Tech.* **45**, 2025-2034 (1997).
45. J. D. Stratton, *Electromagnetic Theory* (McGraw-Hill, New York, N. Y.) (1941).
46. A. W. Snyder and D. J. Mitchell, "Leaky mode analysis of circular optical waveguides", *Opto-Electronics* **6**, 287-296 (1974).
47. H. F. Taylor and A. Yariv, "Guided wave optics", *Proc. IEEE* **62**, 1044-1060 (1974).

48. A. Hardy and W. Streifer, "Coupled mode theory of parallel waveguides", *J. Lightwave Technol.* **3**, 1135-146 (1985).
49. S.-L. Chuang, "A coupled mode formulation by reciprocity and a variational principle", *J. Lightwave Technol.* **5**, 5-15 (1987).
50. H. A. Haus, W. P. Huang, S. Kawakami, and N. A. Whitaker, "Coupled-mode theory of optical waveguides", *J. Lightwave Technol.* **5**, 16-23 (1987).
51. D. R. Rowland and J. D. Love, "Evanescent wave coupling of whispering gallery modes of a dielectric cylinder", *IEE Proc.-J* **140**, 177-188 (1993).
52. M. A. McHenry and D. C. Chang, "Coupled-Mode theory of two nonparallel dielectric waveguides", *IEEE Trans. Microwave Theory Tech.* **32**, 1469-1475 (1984).
53. Q. Han, Y. Kogami, Y. Tomabechi, and K. Matsumura, "Coupling characteristics of eccentric arranged dielectric disk and ring", *IEEE Trans. Microwave Theory Tech.* **MIT-44**, 2017-2024 (1996).
54. M. L. Gorodetsky and V. S. Ilchenko, "Optical microsphere resonators: optimal coupling to high- Q whispering-gallery modes", *J. Opt. Soc. B* **16**, 147-154 (1999).
55. V. S. Ilchenko, X. S. Yao, and L. Maleki, "Pigtailing the high- Q microsphere cavity: a simple fiber coupler for optical whispering-gallery modes", *Opt. Lett.* **24**, 723-725 (1999).
56. K. Kawase, J.-I. Shikata, and H. Ito, "Terahertz wave parametric source", *J. Phys. D: Appl. Phys.* **35**, R1-R14 (2002).
57. V. Ryzhii and I. Khmyrova, "Terahertz photomixing in quantum well structures using resonant excitation of plasma oscillations", *J. Appl. Phys.* **91**, 1875-1881 (2002).

58. M. L. Abell and J. P. Braselton, *Differential Equations with Mathematica* (Academic Press, Boston) (1993).
59. J. C. Slater, *Microwave Electronics* (D. Van Nostrand, New York) (1950).
60. C. A. Balanis, *Advanced Engineering Electromagnetics*, (John Wiley & Sons, New York) (1989).
61. R. E. Collin, *Field Theory of Guided Waves*, 2nd edition, (IEEE Press, New York) (1991).

APPENDIXES

Appendix A

Impedance, Orthogonality and Normalization of Guided Modes

We start from the source-free Maxwell's equations

$$\nabla \times \mathbf{E} = \left(\nabla' + \hat{z} \frac{\partial}{\partial z} \right) \times \mathbf{E} = -\mu_0 \frac{\partial \mathbf{H}}{\partial t}, \quad (\text{A-1})$$

$$\nabla \times \mathbf{H} = \left(\nabla' + \hat{z} \frac{\partial}{\partial z} \right) \times \mathbf{H} = \varepsilon_r \varepsilon_0 \frac{\partial \mathbf{E}}{\partial t}, \quad (\text{A-2})$$

where ε_0 and μ_0 are the free space permittivity and permeability, respectively, ε_r is the relative permittivity, the superscript t denotes the transverse component, and the caret $\hat{}$ indicates a unit vector. Here we have assumed that the relative permeability is 1. For TE or TM polarized guided modes, the characteristic impedance η is determined by [34,59]

$$\hat{z} \times \mathbf{E}' = \eta \mathbf{H}', \quad (\text{A-3})$$

Now we deduce the explicit expressions for η for both the TE and TM modes. For TE modes, $\mathbf{E} = \mathbf{E}^t$, so we obtain from (A-1)

$$\hat{z} \times \frac{\partial \mathbf{E}^t}{\partial z} = -\mu_0 \frac{\partial \mathbf{H}^t}{\partial t}. \quad (\text{A-4})$$

Replacing $\partial/\partial z$ by $i\beta$, and $\partial/\partial t$ by $-i\omega$, we obtain

$$\hat{z} \times \mathbf{E}^t = \frac{\omega \mu_0}{\beta} \mathbf{H}^t = \frac{k}{\beta} \sqrt{\frac{\mu_0}{\epsilon_0}} \mathbf{H}^t, \quad (\text{A-5})$$

where β is the propagation constant, ω is the angular frequency, and k is the free-space wavenumber. Comparing (A-5) and (A-3), we obtain for TE modes

$$\eta_{TE} = \frac{k}{\beta} \sqrt{\frac{\mu_0}{\epsilon_0}} = \frac{k}{\beta} \eta_0, \quad (\text{A-6})$$

where $\eta_0 = \sqrt{\frac{\mu_0}{\epsilon_0}}$ is the intrinsic impedance of free-space [60].

For TM modes, $\mathbf{H} = \mathbf{H}^t$, so we obtain from (A-2)

$$\hat{z} \times \frac{\partial \mathbf{H}^t}{\partial z} = \epsilon_r \epsilon_0 \frac{\partial \mathbf{E}^t}{\partial t}. \quad (\text{A-7})$$

Replacing $\partial/\partial z$ by $i\beta$, and $\partial/\partial t$ by $-i\omega$, we obtain

$$\mathbf{E}^t = -\frac{\beta}{k \epsilon_r} \sqrt{\frac{\mu_0}{\epsilon_0}} \hat{z} \times \mathbf{H}^t. \quad (\text{A-8})$$

This leads to

$$\begin{aligned} \hat{z} \times \mathbf{E}^t &= -\frac{\beta}{k \epsilon_r} \sqrt{\frac{\mu_0}{\epsilon_0}} \hat{z} \times (\hat{z} \times \mathbf{H}^t) \\ &= -\frac{\beta}{k \epsilon_r} \sqrt{\frac{\mu_0}{\epsilon_0}} [(\hat{z} \cdot \mathbf{H}^t) \hat{z} - \hat{z} \cdot \hat{z} \mathbf{H}^t] \end{aligned}$$

$$= \frac{\beta}{k\varepsilon_r} \sqrt{\frac{\mu_0}{\varepsilon_0}} \mathbf{H}^t, \quad (\text{A-9})$$

where the vector equality $\mathbf{c} \times (\mathbf{a} \times \mathbf{b}) = (\mathbf{c} \cdot \mathbf{b})\mathbf{a} - (\mathbf{c} \cdot \mathbf{a})\mathbf{b}$ has been used. Comparing (A-9) and (A-3), we obtain for TM modes

$$\eta_{TM} = \frac{\beta}{k\varepsilon_r} \sqrt{\frac{\mu_0}{\varepsilon_0}} = \frac{\beta}{k\varepsilon_r} \eta_0. \quad (\text{A-10})$$

Notice that ε_r is a space-dependent variable, indicating that for TM modes, η is also space-dependent. However, for TE modes, all the parameters in Eq. (A-6) are constants for a specific mode, so η is also a constant for this mode.

The general orthogonality relation for guided modes can be written as [42,61]

$$\iint_S \mathbf{E}_n \times \mathbf{H}_m \cdot \hat{\mathbf{z}} dS = 0, \text{ when } n \neq m, \quad (\text{A-11})$$

where n and m are mode indexes. When there is no loss present, it can be shown that [61]

$$\iint_S \mathbf{E}_n \times \mathbf{H}_m^* \cdot \hat{\mathbf{z}} dS = \iint_S \mathbf{E}_n^* \times \mathbf{H}_m \cdot \hat{\mathbf{z}} dS = 0, \text{ when } n \neq m, \quad (\text{A-12})$$

where the asterisk * denotes complex conjugate. With (A-3) we have

$$\begin{aligned} \mathbf{E}_n \times \mathbf{H}_m \cdot \hat{\mathbf{z}} &= (\mathbf{E}_n^t + \hat{\mathbf{z}}E_n^z) \times (\mathbf{H}_m^t + \hat{\mathbf{z}}H_m^z) \cdot \hat{\mathbf{z}} \\ &= \mathbf{E}_n^t \times \mathbf{H}_m^t \cdot \hat{\mathbf{z}} \\ &= \frac{1}{\eta_m} [\mathbf{E}_n^t \times (\hat{\mathbf{z}} \times \mathbf{E}_m^t)] \cdot \hat{\mathbf{z}} \\ &= \frac{1}{\eta_m} [(\mathbf{E}_n^t \cdot \mathbf{E}_m^t) \hat{\mathbf{z}} - (\mathbf{E}_n^t \cdot \hat{\mathbf{z}}) \mathbf{E}_m^t] \cdot \hat{\mathbf{z}} \end{aligned}$$

$$= \frac{1}{\eta_m} \mathbf{E}_n^t \cdot \mathbf{E}_m^t, \quad (\text{A-13})$$

Substituting (A-13) into (A-11) we get

$$\iint_S \frac{1}{\eta_m} \mathbf{E}_n^t \cdot \mathbf{E}_m^t dS = 0, \text{ when } n \neq m. \quad (\text{A-14})$$

Up to now we have not made any assumptions or approximations, so (A-14) and (A-11) are equivalent for TE and/or TM modes. Note that η_m is space-dependent for TM modes of dielectric waveguide. For TE modes (with the assumption that the relative permeability is 1) or waveguides with perfectly conducting walls, η_m is a constant for a specific mode. This leads to the well-known orthogonality relation for *TE modes of dielectric waveguides* or *TE and TM modes of waveguides with perfectly conducting walls* [34,61]

$$\iint_S \mathbf{E}_n^t \cdot \mathbf{E}_m^t dS = 0, \text{ when } n \neq m. \quad (\text{A-15})$$

If there is no loss present, a similar procedure leads to

$$\iint_S \frac{1}{\eta_m} \mathbf{E}_n^t \cdot (\mathbf{E}_m^t)^* dS = \iint_S \frac{1}{\eta_n} \mathbf{E}_n^t \cdot (\mathbf{E}_m^t)^* dS = 0, \text{ when } n \neq m. \quad (\text{A-16})$$

for the general case, and

$$\iint_S \mathbf{E}_n^t \cdot (\mathbf{E}_m^t)^* dS = 0, \text{ when } n \neq m. \quad (\text{A-17})$$

for *TE modes of dielectric waveguides* or *TE and TM modes of waveguides with perfectly conducting walls*. It is further deduced from (A-14) that, in general, for *TM modes of dielectric waveguides*

$$\iint_S \mathbf{E}_n^t \cdot \mathbf{E}_m^t dS \neq 0, \quad \iint_S \mathbf{H}_n^t \cdot \mathbf{H}_m^t dS \neq 0; \quad (\text{A-18})$$

and from (A-16) for the lossless case

$$\iint_S \mathbf{E}_n^t \cdot (\mathbf{E}_m^t)^* dS \neq 0, \quad \iint_S \mathbf{H}_n^t \cdot (\mathbf{H}_m^t)^* dS \neq 0. \quad (\text{A-19})$$

If the modes are normalized by the power propagating along z direction, such that [42]

$$\frac{1}{2} \iint_S \mathbf{e}_m \times \mathbf{h}_m^* \cdot \hat{z} dS = \frac{1}{2} \iint_S \mathbf{e}_m^* \times \mathbf{h}_m \cdot \hat{z} dS = 1, \quad (\text{A-20})$$

then the orthogonality and normalization relations can be combined as [42]

$$\frac{1}{2} \iint_S \mathbf{e}_n \times \mathbf{h}_m^* \cdot \hat{z} dS = \frac{1}{2} \iint_S \mathbf{e}_m^* \times \mathbf{h}_n \cdot \hat{z} dS = \delta_{mn}, \quad (\text{A-21})$$

or equivalently

$$\frac{1}{2} \iint_S \frac{1}{\eta_m} \mathbf{e}_n^t \cdot (\mathbf{e}_m^t)^* dS = \frac{1}{2} \iint_S \frac{1}{\eta_n} \mathbf{e}_n^t \cdot (\mathbf{e}_m^t)^* dS = \delta_{mn}. \quad (\text{A-22})$$

In Eqs. (A-20) to (A-22), the lower case \mathbf{e} and \mathbf{h} represent normalized fields, and the factor 1/2 is from time averaging [42].

It should be noted that, all the equations with impedance are only valid for *TE* or *TM* modes. For hybrid modes as in the dielectric rod, the general forms of (A-11), (A-12), and (A-21) should be used for orthogonality and normalization.

Appendix B

Derivation of Reciprocity Relation (5-4)

For a vector in cylindrical coordinates $\mathbf{A} = \hat{r}A^r + \hat{\theta}A^\theta + \hat{x}A^x$, where the superscripts r , θ , and x indicate the corresponding components, we have

$$\nabla \cdot \mathbf{A} = \frac{1}{r} \frac{\partial(rA^r)}{\partial r} + \frac{\partial A^x}{\partial x} + \frac{1}{r} \frac{\partial \mathbf{A}}{\partial \theta} \cdot \hat{\theta}. \quad (\text{B-1})$$

Multiplying both sides with r and integrate along r direction, and assuming that the system is uniform along x direction so $\partial/\partial x = 0$, we have

$$\begin{aligned} \int_0^\infty r \nabla \cdot \mathbf{A} dr &= \int_0^\infty \frac{\partial(rA^r)}{\partial r} dr + \int_0^\infty \frac{\partial \mathbf{A}}{\partial \theta} \cdot \hat{\theta} dr \\ &= (rA^r) \Big|_{r=0}^{r=\infty} + \int_0^\infty \frac{\partial \mathbf{A}}{\partial \theta} \cdot \hat{\theta} dr \\ &= \frac{\partial}{\partial \theta} \int_0^\infty \mathbf{A} \cdot \hat{\theta} dr, \end{aligned} \quad (\text{B-2})$$

where we have assumed that for guided modes the field quantities are zero at $r = \infty$.

Applying this relation to the vector $(\mathbf{E}_1 \times \mathbf{H}_2^* + \mathbf{E}_2^* \times \mathbf{H}_1)$, and with Eq. (5-3), we get (5-4).

A similar approach leads to the unconjugated form (5-5). In Ref. 53, from (B-1) the

authors derived

$$\int_0^\infty \nabla \cdot \mathbf{A} dr = \int_0^\infty \frac{1}{r} \frac{\partial(rA')}{\partial r} dr + \int_0^\infty \frac{1}{r} \frac{\partial \mathbf{A}}{\partial \theta} \cdot \hat{\theta} dr. \quad (\text{B-3})$$

Then the first integral of (B-3) on the right-hand is set to zero (the justification they gave was weak), and the reciprocity relation was

$$\frac{\partial}{\partial \theta} \int_0^\infty \frac{1}{r} (\mathbf{E}_1 \times \mathbf{H}_2 - \mathbf{E}_2 \times \mathbf{H}_1) \cdot \hat{\theta} dr = ik \sqrt{\frac{\epsilon_0}{\mu_0}} \int_0^\infty (\epsilon_2 - \epsilon_1) \mathbf{E}_1 \cdot \mathbf{E}_2 dr. \quad (\text{B-4})$$

For comparison, the reciprocity relation we derived, i.e. Eq. (5-5), is also written here (with $\mathbf{J}_1 = \mathbf{J}_2 = 0$)

$$\frac{\partial}{\partial \theta} \int_0^\infty (\mathbf{E}_1 \times \mathbf{H}_2 - \mathbf{E}_2 \times \mathbf{H}_1) \cdot \hat{\theta} dr = ik \sqrt{\frac{\epsilon_0}{\mu_0}} \int_0^\infty (\epsilon_2 - \epsilon_1) r \mathbf{E}_1 \cdot \mathbf{E}_2 dr. \quad (\text{B-5})$$

Appendix C

Derivation of Longitudinal Components (5-9a) and (5-9b)

We start from the vector equality in cylindrical coordinates

$$\nabla \times \mathbf{A} = \left(\nabla^t + \frac{1}{r} \hat{\theta} \frac{\partial}{\partial \theta} \right) \times \mathbf{A}, \quad (\text{C-1})$$

where the superscript t denotes the transverse component. From Eqs. (5-2a) and (5-2b), the source-free Maxwell's equations for the total fields can then be written in the cylindrical coordinates as

$$\nabla^t \times \mathbf{E}_T + \frac{1}{r} \hat{\theta} \times \frac{\partial}{\partial \theta} \mathbf{E}_T = ik \sqrt{\frac{\mu_0}{\epsilon_0}} \mathbf{H}_T, \quad (\text{C-2a})$$

$$\nabla^t \times \mathbf{H}_T + \frac{1}{r} \hat{\theta} \times \frac{\partial}{\partial \theta} \mathbf{H}_T = -ik \epsilon_T \sqrt{\frac{\epsilon_0}{\mu_0}} \mathbf{E}_T. \quad (\text{C-2b})$$

For θ component of (C-2b), we have

$$\nabla^t \times \mathbf{H}_T^t = -ik \epsilon_T \sqrt{\frac{\epsilon_0}{\mu_0}} \mathbf{E}_T^\theta. \quad (\text{C-3})$$

With the help of (5-8b) we have for the θ component of the total electrical field

$$\begin{aligned}
\hat{\theta}E_T^\theta &= -\frac{1}{ik\varepsilon_T} \sqrt{\frac{\mu_0}{\varepsilon_0}} \nabla' \times \mathbf{H}_T^\theta \\
&= -\frac{1}{ik\varepsilon_T} \sqrt{\frac{\mu_0}{\varepsilon_0}} [a(\theta) \nabla' \times \mathbf{H}_a' + b(\theta) \nabla' \times \mathbf{H}_b'] \\
&= -\frac{1}{ik\varepsilon_T} \sqrt{\frac{\mu_0}{\varepsilon_0}} \left[a(\theta) \left(-ik\varepsilon_a \sqrt{\frac{\varepsilon_0}{\mu_0}} \hat{\theta}E_a^\theta \right) + b(\theta) \left(-ik\varepsilon_b \sqrt{\frac{\varepsilon_0}{\mu_0}} \hat{\theta}E_b^\theta \right) \right] \\
&= a(\theta) \frac{\varepsilon_a}{\varepsilon_T} \hat{\theta}E_a^\theta + b(\theta) \frac{\varepsilon_b}{\varepsilon_T} \hat{\theta}E_b^\theta. \tag{C-4}
\end{aligned}$$

A similar procedure can be applied to get the θ component of the total magnetic field.

Appendix D

Physical Explanation of Coupled Mode Equations

D.1 Mode Excitation by Current Sources [42]

Suppose we now have a ring waveguide with a complete set of modes, we determine the amplitudes of the modes excited by a prescribed distribution of currents \mathbf{J} , as shown in Fig. D-1. The total fields everywhere in the ring are expressed as the modal expansion of the complete set of the ring modes

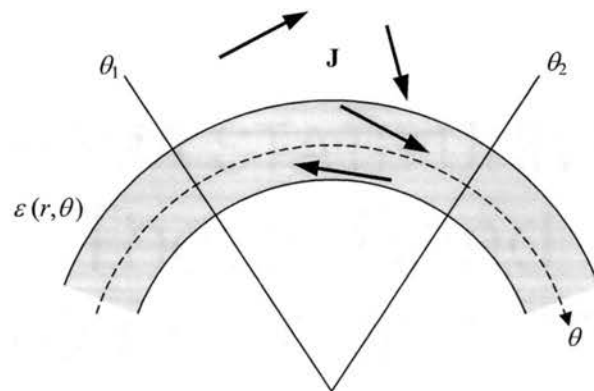


Fig. D-1 A prescribed distribution of currents with density \mathbf{J} occupies the volume between the transverse planes $\theta = \theta_1$ and $\theta = \theta_2$.

$$\mathbf{E} = \sum_j a_j(\theta) \mathbf{e}_j \exp(i\beta_j \theta),$$

$$\mathbf{H} = \sum_j a_j(\theta) \mathbf{h}_j \exp(i\beta_j \theta), \quad (\text{D-1})$$

where β_j is the angular propagation constant for the j th mode, and the modal amplitudes depends on θ only. For the first set of solutions, we use $\mathbf{E}_1 = \mathbf{E}$, $\mathbf{H}_1 = \mathbf{H}$, $\mathbf{J}_1 = \mathbf{J}$, and for the second set, we use the j th modal field on the source-free waveguide, i.e. $\mathbf{J}_2 = 0$, $n_2 = n_1 = n$, and

$$\mathbf{E}_2 = \mathbf{e}_j \exp(i\beta_j \theta); \quad \mathbf{H}_2 = \mathbf{h}_j \exp(i\beta_j \theta). \quad (\text{D-2})$$

Substituting into Eq. (5-4) and assume all the modes satisfy the orthogonal and normalization relation, we get

$$\frac{da_j(\theta)}{d\theta} = -\frac{1}{4} \int_0^\infty \mathbf{e}_j^* \cdot \mathbf{J} \exp(-i\beta_j \theta) r dr. \quad (\text{D-3})$$

D.2 Physical Derivation of Coupled Mode Equations

As shown in Fig. D-2a, we consider a waveguide with relative permittivity profile $\bar{\epsilon}(r, x)$ which is invariant in θ , and current density distribution $\mathbf{J}(r, \theta, x)$. From (5-2b) the Maxwell's equation is

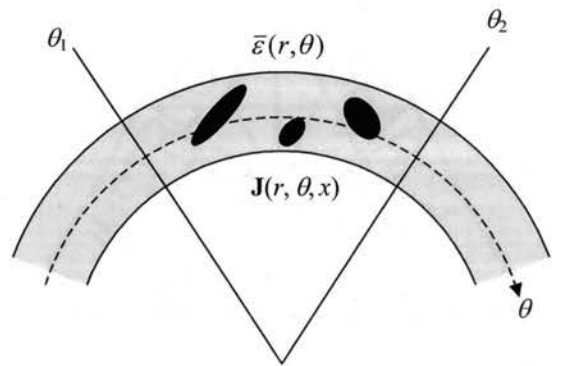
$$\nabla \times \mathbf{H} = \mathbf{J} - ik\bar{\epsilon} \sqrt{\frac{\epsilon_0}{\mu_0}} \mathbf{E}. \quad (\text{D-4})$$

On the other hand, for the waveguide shown in Fig. D-2b, where the current density is

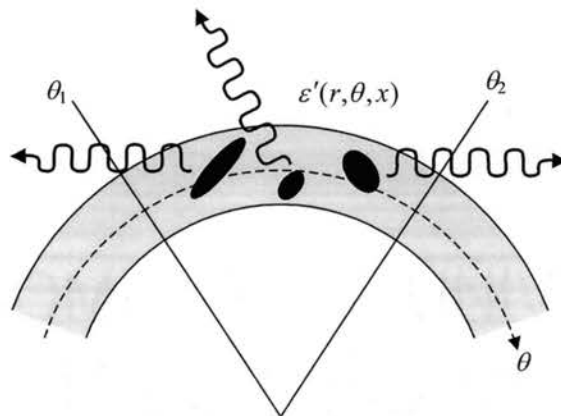
zero but the relative permittivity profile $\varepsilon'(r, \theta, x)$ is slightly changed from $\bar{\varepsilon}(r, x)$, the Maxwell's equation is

$$\nabla \times \mathbf{H} = -ik\varepsilon' \sqrt{\frac{\varepsilon_0}{\mu_0}} \mathbf{E} = -ik(\varepsilon' - \bar{\varepsilon}) \sqrt{\frac{\varepsilon_0}{\mu_0}} \mathbf{E} - ik\bar{\varepsilon} \sqrt{\frac{\varepsilon_0}{\mu_0}} \mathbf{E}. \quad (\text{D-5})$$

If we compare Eqs. (D-4) and (D-5), the first term on the right side of (D-5) can be identified by a fictitious induced current given by [42]



(a)



(b)

Fig. D-2 (a) Unperturbed waveguide with current density distribution $\mathbf{J}(r, \theta, x)$ denoted by darkly shaded regions. (b) Perturbed waveguide. Darkly shaded regions denote the nonuniformities.

$$\mathbf{J} = -ik(\varepsilon' - \bar{\varepsilon})\sqrt{\frac{\varepsilon_0}{\mu_0}}\mathbf{E}. \quad (\text{D-6})$$

The quantity $(\varepsilon' - \bar{\varepsilon})$ represents the perturbation to the original medium $\bar{\varepsilon}(r, x)$. This can represent scattering centers in a fiber, or in our case, one ring to another. For our system with two rings, the fictitious current to ring a induced by ring b can be written as

$$\mathbf{J} = -ik(\varepsilon_T - \varepsilon_a)\sqrt{\frac{\varepsilon_0}{\mu_0}}\mathbf{E}_T, \quad (\text{D-7})$$

where \mathbf{E}_T , ε_T and ε_a are the total electric field and the relative permittivities defined in section 5.3.

On the other hand, mode can be excited by current distribution as shown in Eq. (D-3).

For ring a , this excitation can be written as

$$\begin{aligned} \frac{da'(\theta)}{d\theta} &= -\frac{1}{4} \int_0^\infty (\mathbf{e}_a^t + \hat{\theta}e_a^\theta)^* \cdot \mathbf{J} \exp(-il\theta) r dr \\ &= i \frac{k}{4} \sqrt{\frac{\varepsilon_0}{\mu_0}} \int_0^\infty (\varepsilon_T - \varepsilon_a) (\mathbf{e}_a^t + \hat{\theta}e_a^\theta)^* \cdot (\mathbf{E}_T^t + \hat{\theta}E_T^\theta) \exp(-i\beta_a\theta) r dr. \end{aligned} \quad (\text{D-8})$$

Substituting Eqs. (5-8a) and (5-9a) into the right side, we get the right side of Eq. (5-12).

On the left side of (D-8), $a'(\theta)$ refers to the total amplitude of mode of ring a , which can be expressed as the ‘‘projection’’ of the total field into the normalized modal field of ring a [42]

$$a'(\theta) = \frac{1}{4} \int_0^\infty \exp(-i\beta_a\theta) (\mathbf{e}_a^* \times \mathbf{H}_T + \mathbf{E}_T \times \mathbf{h}_a^*) \cdot \hat{\theta} dr, \quad (\text{D-9})$$

which is exactly the term in the brackets on the left side of Eq. (5-12). For this reason M_{pq} in Eqs. (5-12) and (5-15) may be more precisely called mode-mapping coefficients.

Appendix E

Quasioptic Coupling

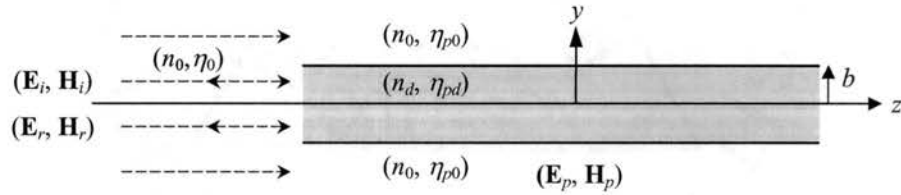


Fig. E-1 Coupling from free-space to dielectric waveguide.

With the knowledge of orthogonality as shown in Appendix A, we derive the coupling coefficient for the coupling from free-space to a dielectric waveguide, as shown in Fig. E-1. We assume that the system is uniform in x direction so $\partial/\partial x = 0$. At the interface of the input side, the boundary conditions lead to

$$\mathbf{E}_i^t + \mathbf{E}_r^t = \sum_p a_p \mathbf{E}_p^t, \quad (\text{E-1})$$

$$\mathbf{H}_i^t - \mathbf{H}_r^t = \sum_p a_p \mathbf{H}_p^t. \quad (\text{E-2})$$

From Eq. (A-3), (E-2) becomes

$$\frac{1}{\eta_0} \hat{z} \times (\mathbf{E}_i^t - \mathbf{E}_r^t) = \hat{z} \times \sum_p a_p \frac{1}{\eta_p} \mathbf{E}_p^t. \quad (\text{E-3})$$

It can be shown from (E-3) that

$$\mathbf{E}_i^t - \mathbf{E}_r^t = \sum_p a_p \frac{\eta_0}{\eta_p} \mathbf{E}_p^t. \quad (\text{E-4})$$

Applying the orthogonality relation (A-16) to (E-1) and (E-4), we obtain

$$\int_{-\infty}^{\infty} (\mathbf{E}_i^t + \mathbf{E}_r^t) \cdot \frac{1}{\eta_p} (\mathbf{E}_p^t)^* dy = a_p \int_{-\infty}^{\infty} \frac{1}{\eta_p} \mathbf{E}_p^t \cdot (\mathbf{E}_p^t)^* dy, \quad (\text{E-5})$$

$$\int_{-\infty}^{\infty} (\mathbf{E}_i^t - \mathbf{E}_r^t) \cdot (\mathbf{E}_p^t)^* dy = a_p \eta_0 \int_{-\infty}^{\infty} \frac{1}{\eta_p} \mathbf{E}_p^t \cdot (\mathbf{E}_p^t)^* dy, \quad (\text{E-6})$$

where η_p is space-dependent

$$\eta_p = \begin{cases} \eta_{pd}, & \text{inside dielectric, } |y| < b; \\ \eta_{p0}, & \text{outside dielectric, } |y| > b. \end{cases} \quad (\text{E-7})$$

Assuming $\mathbf{E}_r = 0$ (no reflection) outside dielectric ($|y| > b$), (E-5) and (E-6) become

$$\eta_{pd} \int_{-\infty}^{\infty} \mathbf{E}_i^t \cdot \frac{1}{\eta_p} (\mathbf{E}_p^t)^* dy + \int_{-b}^b \mathbf{E}_r^t \cdot (\mathbf{E}_p^t)^* dy = a_p \eta_{pd} \int_{-\infty}^{\infty} \frac{1}{\eta_p} \mathbf{E}_p^t \cdot (\mathbf{E}_p^t)^* dy, \quad (\text{E-8})$$

$$\int_{-\infty}^{\infty} \mathbf{E}_i^t \cdot (\mathbf{E}_p^t)^* dy - \int_{-b}^b \mathbf{E}_r^t \cdot (\mathbf{E}_p^t)^* dy = a_p \eta_0 \int_{-\infty}^{\infty} \frac{1}{\eta_p} \mathbf{E}_p^t \cdot (\mathbf{E}_p^t)^* dy. \quad (\text{E-9})$$

Adding both sides of (E-8) and (E-9), and solving for a_p , we get

$$a_p = \frac{\eta_{pd} \int_{-\infty}^{\infty} \mathbf{E}_i^t \cdot \frac{1}{\eta_p} (\mathbf{E}_p^t)^* dy + \int_{-\infty}^{\infty} \mathbf{E}_i^t \cdot (\mathbf{E}_p^t)^* dy}{(\eta_{pd} + \eta_0) \int_{-\infty}^{\infty} \frac{1}{\eta_p} \mathbf{E}_p^t \cdot (\mathbf{E}_p^t)^* dy}. \quad (\text{E-10})$$

Applying the similar procedure to the output interface, we get at the output, the coupling from p th guided mode into the same mode as the incident mode

$$a'_p = \frac{\eta_{pd} \int_{-\infty}^{\infty} \frac{1}{\eta_p} \mathbf{E}_p^t \cdot (\mathbf{E}_i^t)^* dy + \int_{-\infty}^{\infty} \mathbf{E}_p^t \cdot (\mathbf{E}_i^t)^* dy}{(\eta_{pd} + \eta_0) \int_{-\infty}^{\infty} \frac{1}{\eta_0} \mathbf{E}_i^t \cdot (\mathbf{E}_i^t)^* dy}. \quad (\text{E-11})$$

If the modes are normalized by (A-20), then

$$a_p = (a'_p)^* = \frac{\eta_{pd} \int_{-\infty}^{\infty} \mathbf{e}_i^t \cdot \frac{1}{\eta_p} (\mathbf{e}_p^t)^* dy + \int_{-\infty}^{\infty} \mathbf{e}_i^t \cdot (\mathbf{e}_p^t)^* dy}{2(\eta_{pd} + \eta_0)}. \quad (\text{E-12})$$

Other types of coupling can be calculated following the similar procedure. The couplings in our structures include: (a) coupling between free-space and a parallel metal plate waveguide with plate separation $2b$; (b) coupling between the silicon-filled metal plate waveguide and the dielectric silicon slab waveguide of thickness $2b$. For case (a), the coupling coefficient is calculated as

$$a_p = (a'_p)^* = \frac{\int_{-b}^b \mathbf{e}_i^t \cdot (\mathbf{e}_p^t)^* dy}{\eta_p + \eta_0}. \quad (\text{E-13})$$

For case (b), the coupling coefficient for the coupling between TM_p mode of the metal plate and the TM_q mode of the slab is given as

$$a_{pq} = (a'_{pq})^* = \frac{\int_{-b}^b \mathbf{e}_{gp}^t \cdot (\mathbf{e}_{sq}^t)^* dy}{\eta_{sqd} + \eta_{gp}}, \quad (\text{E-14})$$

where the subscripts gp denote the TM_p mode of the metal guide, sq denote the TM_q mode of the slab mode, and d means inside the dielectric. In the derivations we have assumed that the reflection mode has the same impedance with the incident mode, and the modal fields in (E-13) and (E-14) have been normalized by (A-20).

Appendix F

Fourth Order Runge-Kutta Method

For an initial value problem with single variable

$$\begin{cases} \frac{dy}{dx} = f(x, y), \\ y(x_0) = y_0, \end{cases} \quad (\text{F-1})$$

the 4th order Runge-Kutta method can be used to numerically solve it. In this case, the recursive formula at each step is [58]

$$y_{n+1} = y_n + \frac{h}{6}(k_1 + 2k_2 + 2k_3 + k_4), \quad (\text{F-2})$$

where

$$\begin{aligned} k_1 &= f(x_n, y_n), \\ k_2 &= f\left(x_n + \frac{h}{2}, y_n + \frac{hk_1}{2}\right), \\ k_3 &= f\left(x_n + \frac{h}{2}, y_n + \frac{hk_2}{2}\right), \\ k_4 &= f(x_n + h, y_n + hk_3), \end{aligned} \quad (\text{F-3})$$

and h is the step size for x in the numerical calculation.

Now we expand this method to a system with multiple variables. Consider the following initial value problem with N variables

$$\begin{cases} \frac{dY}{dx} = F(x, Y), \\ Y(x_0) = Y_0, \end{cases} \quad (\text{F-4})$$

$$\text{where } Y = \begin{pmatrix} y_1 \\ y_2 \\ \vdots \\ y_N \end{pmatrix}, Y_0 = \begin{pmatrix} y_{10} \\ y_{20} \\ \vdots \\ y_{N0} \end{pmatrix}, \text{ and } F(x, Y) = \begin{pmatrix} f_1(x, y_1, y_2, \dots, y_N) \\ f_2(x, y_1, y_2, \dots, y_N) \\ \vdots \\ f_N(x, y_1, y_2, \dots, y_N) \end{pmatrix}.$$

In a similar fashion, the recursive formula is written as

$$Y_{n+1} = Y_n + \frac{h}{6}(K_1 + 2K_2 + 2K_3 + K_4), \quad (\text{F-5})$$

where

$$\begin{aligned} K_1 &= F(x_n, Y_n), \\ K_2 &= F\left(x_n + \frac{h}{2}, Y_n + \frac{hK_1}{2}\right), \\ K_3 &= F\left(x_n + \frac{h}{2}, Y_n + \frac{hK_2}{2}\right), \\ K_4 &= F(x_n + h, Y_n + hK_3). \end{aligned} \quad (\text{F-6})$$

For our coupled mode equations, the problem is of the form of

$$\begin{cases} \frac{d}{dx}[M(x)Y(x)] = F(x, Y), \\ Y(x_0) = Y_0, \end{cases} \quad (\text{F-7})$$

where $M(x)$ is a known $N \times N$ matrix. To solve this problem, let $Z(x) = M(x)Y(x)$, then we get

$$Y(x) = M^{-1}(x)Z(x), \quad (\text{F-8})$$

where $M^{-1}(x)$ is the inverse matrix of $M(x)$. Substitute these relations into (F-7), we get

$$\begin{cases} \frac{dZ}{dx} = F(x, M^{-1}Z) = G(x, Z), \\ Z(x_0) = Z_0 = M(x_0)Y(x_0), \end{cases} \quad (\text{F-9})$$

which is of the same form as (F-4). After solving this problem for $Z(x)$, solutions of $Y(x)$ can be obtained by (F-8).

Another way of solving the problem is to expand the differentiation in (F-7). Noticing that

$$\frac{d}{dx}[MY] = M \frac{dY}{dx} + \frac{dM}{dx}Y, \quad (\text{F-10})$$

we can write Eq. (F-7) as

$$\frac{dY}{dx} = M^{-1} \left(F(x, Y) - \frac{dM}{dx}Y \right) = G'(x, Y), \quad (\text{F-11})$$

which is of the solvable form of (F-4).

VITA 2

JIANGQUAN ZHANG

Candidate for the Degree of

Doctor of Philosophy

Thesis: A CYLINDRICAL DIELECTRIC WHISPERING-GALLERY MODE
TERAHERTZ CAVITY COUPLED WITH A DIELECTRIC SLAB
WAVEGUIDE

Major Field: Electrical Engineering

Biographical:

Personal Data: Born in Xiaxian, Shanxi, P. R. China, on May 11, 1970, the son of Mr. Baocun Zhang and Mrs. Taotao Zhu.

Education: Graduated from Kangjie High School, Yuncheng, Shanxi, China, in July 1987; received Bachelor of Science degree in Physics from University of Science and Technology of China, Hefei, Anhui, China, in July 1992; received Master of Science degree in Semiconductor Physics from Institute of Semiconductors, Chinese Academy of Sciences, Beijing, China, in July 1995; completed requirements for Doctor of Philosophy degree at Oklahoma State University in August 2002.

Professional Experience: Graduate Research Assistant, School of Electrical and Computer Engineering, Oklahoma State University, January 1998 to present; Graduate Research Assistant, Department of Physics, Oklahoma State University, May 1997 to December 1997; Teaching Assistant, Department of Physics, Oklahoma State University, August 1996 to May 1997; Software Engineer, Legend Group Co., Beijing, China, August 1995 to June 1996; Graduate Research Assistant, Institute of Semiconductors, Chinese Academy of Sciences, Beijing, China, August 1993 to July 1995.